Tailoring the Optoelectronic Properties of Carbon Nanotubes - A Comparative Study of Covalent and Non-Covalent Functionalization Approaches

Dissertation

zur Erlangung des Grades eines Doktors der Naturwissenschaften
am Fachbereich Physik der Freien Universität Berlin

eingereicht von
Mareen Gläske

Berlin, im August 2018

1. Reviewer Prof. Dr. Stephanie Reich
Fachbereich Physik
Freie Universität Berlin

2. Reviewer Prof. Dr. Rainer Haag
Fachbereich Chemie
Freie Universität Berlin

Tag der Einreichung: 14.08.2018
Tag der Disputation: 16.11.2018

Hofstadter's Law:
It always takes longer than you expect,
even when you take into account Hofstadter's Law.
-Douglas Hofstadter, Gödel, Escher, Bach: An Eternal Golden Braid.

Abstract

The functionalization of carbon nanotubes (CNTs) is an ongoing and actively researched topic in the scientific community. The modification of tubes through functionalities leads to new physical properties of the tubes and opens the way to real nanotechnological applications. Functionalization methods can be classified into three different classes - endohedral, covalent, and non-covalent approaches. All three methods come with specific advantages and challenges, as I will discuss in the introductory chapters of this thesis.

In the first part of this thesis, I will introduce a new covalent functionalization routine that we have developed. It is based on a nitrine based [2+1] cycloaddition reaction and for the very first time in literature, it maintains the extended π-network and preserves the outstanding optoelectronic properties of carbon nanotubes, even at an high degree of functionalization. This new method we developed offers a robust way to attach functional moieties on the tubes and creates a new toolbox for advanced tailoring of the nanotubes properties.

In the second part of this work I will describe how non-covalent functionalization methods can be used to attach moieties on the CNTs sidewalls and I will compare their outcome with the results from our new established [2+1] cycloaddition. I will discuss in detail the influence of three different type of functional moieties immobilized to the tubes' sidewalls: The dipole switch **spiropyran**, the molecular dye **perylene**, and **gold nanoparticles**.

The comparative study between covalent and non-covalent functionalization methods shows that functional moieties can be used to strongly influence the optical property of tubes. The study furthermore shows that the tubes' physical properties are also highly sensitive towards the attachment routine used for immobilization of the functional group. The same moiety yield different effects depending upon how it has been attached onto the tubes.

Contents

1 Introduction

Since their discovery in 1991 carbon nanotubes (CNTs) have been subject of intensive investigation, revealing their outstanding properties and promising to enable sophisticated technologies. Their outstanding thermal, electrical, mechanical, and optical properties make CNTs promising candidates for a wide variety of applications (see Chapter 2). CNTs have been incorporated into metal matrices to improve the thermal diffusivity, realizing new materials for heat sink applications [1]. Their low weight and high mechanical robustness promoted the idea of a space elevator composed of CNTs [2]. Although this project revealed itself to be rather unrealistic, CNTs have been successfully integrated into materials used in the automotive and airplane industry, reinforcing their strength and at the same time lowering their weight [3]. Their high electron mobility leads to excellent transport properties. Recently, CNTs have been implemented to build high performance transistor around 40 nm [4], paving the way to potentially replace silicon-based devices. Shulaker *et al.* introduced the first computer built entirely using CNT-based transistors, introducing them as the next generation of highly energy-efficient electronic systems [5]. CNTs have been successfully used for bioapplications: They can be used for protein and virus detection. The hollow tubes can be filled with drugs, realizing targeted medicine release [6]. At the same time, they can be used for in vivo cell imaging due to their infrared emission in the second transparency window of tissue [7]. Most of these applications are based on a) isolating the CNTs, b) overcoming the hydrophobic nature of CNTs to incorporate them into matrices, and/or c) immobilization of additional functional moieties. Different functionalization strategies have been developed to elude those obstacles and realizing sophisticated applications.

The functionalization methods can be classified into three different classes - endohedral, covalent, and non-covalent approaches. All three methods come with specific advantages and challenges, as I will discuss in Chapter 3. In particular, the covalent functionalization benefits of a much firmer attachment than the endohedral and non-covalent approaches. However, the strong immobilization comes at the cost of the integrity of the sp^2 network of the tubes: The strong chemical modification of tubes disrupts the π-network of the CNTs and leads to suppression of their optoelectronical properties. In Chapter 4, a new covalent functionalization routine will be introduced, the nitrene based [2+1] cycloaddition. Those findings are a milestone in the SWNT community: For the first time we could disprove the dogmatic assumption that covalent functionalization always disrupts the optical properties of SWNTs. The functionalization is remarkable as it preserves the π-conjugated system of the SWNTs after the covalent treatment [8].

In the second part of the thesis, I will focus on two aspects of the functionalization process: How the chemical modification and the functional moiety alters the properties of the tubes. I will demonstrate how the different functionalization schemes can be used to anchor three different functional moieties on the sidewall of the SWNTs, namely **spiropyran** - a molecular dipole switch, the dye **perylene**, and **plasmonic nanoparticles**. Different functionalization approaches will be pursued and the influence on the optical properties will be discussed.

Spiropyran - In Chapter 5, I will discuss the interaction of carbon nanotubes with the molecular dipole switch spiropyran, which has been showed to affect the optical response of the tubes. I will present our results on spiropyran-carbon nanotube complexes obtained by the non-covalent micelle swelling approach [9]. This method does not require any anchor nor sophisticated chemistry to warrant close tube-switch proximity. For the first time, we could experimentally validate the theoretical predictions, observing the predicted shifts and their effect on the tubes' excitation and emission energies. Much stronger effects can be observed onto the dipole switch if directly electronically integrated within the nanotubes conjugated network. The new nitrine based [2+1] cycloaddition routine yields hybrid nanotubes that show light-triggered reversible changes of the Fermi energy position and quenching of the tubes' emission [8].

Perylene - In Chapter 6, I will discuss how alkylated polymers conjugated with charged sulfated dendronized perylene bisimides were prepared to wrap around the CNTs scaffolds [10]. The polymer backbone solubilizes the CNTs and decorates them with fluorescent perylene. Photophysical measurements and biological in vitro studies showed superior optical properties, cellular uptake, and intracellular staining. A toxicity assay confirms the highly improved cytocompatibility of the polymer-wrapped CNTs toward surfactant-solubilized CNTs. In microscopy studies, the complexes allow for the direct imaging of the CNTs' cellular uptake via the perylene and CNT emission using the 1st and 2nd optical window for bioimaging. These findings render the polymer-CNT complexes with nanometer size, dual fluorescence, and high cytocompatibility as valuable systems for a broad range of fluorescence bioimaging studies. I will then introduce covalently anchored perylene on the CNTs and compare their features with the polymer-based complexes. The perylene-CNTs compounds prepared by covalent functionalization revealed Förster energy transfer between the perylene donor and the acceptor given by the (6,5) tubes species. The efficiency of the observed perylene-mediated emission matches with the theoretical expectations for the given samples structure.

Gold Nanoparticles - In Chapter 7, I will discuss how, aiming to enhance the luminescence yield of carbon nanotubes, we introduced a new class of hybrid nanoplasmonic colloidal systems (π-hybrids) [11]. To this aim, we dispersed nanotubes in colloidal suspensions of gold nanorods. The yielded hybrid structures exhibited enhanced luminescence. The overall enhancement of the luminescence of the hybrids has been analysed with the aim to improve the synthetic protocol, with particular attention to the dependence of the enhanced photoluminescence yield of our hybrids versus the emission yield over time [12]. Additionally, a plasmonic resonance study reveals that plasmon resonances overlapping with the excitation energy of the tubes

exhibit an enhanced luminescence, whereas a spectral overlap with the emission leads to strong quenching. Furthermore, we explored the mechanism behind the enhancement by monitoring the de-excitation dynamics of the π-hybrids through two-colour pump-probe time-resolved spectroscopy [13]. By evaluating the de-excitation times, the balance between near-field pumping and the faster metal-induced de-excitation contributions is estimated, proving the enhanced pumping to be the leading mechanism. At the end of the chapter, I will show how to adapt the covalent approach to include thiol groups anchored to the triazine. Thiols are known to strongly bind to gold surfaces. This approach yields assembling of the gold nanoparticles on the CNTs sidewall. The hybrids exhibit enhanced optical properties and much stronger stability towards environmental changes than the non-covalent ones.

The comparative study between covalent and non-covalent functionalization methods shows that functional moieties can be used to strongly influence the optical property of tubes. The study furthermore shows that the tubes' physical properties are also highly sensitive towards the attachment routine used for immobilization of the functional group. The same moiety yield different effects depending upon how it has been attached onto the tubes.

2 Structural, Electronical, Optical and Chemical Properties of CNTs

In 1991 Ijima reported on the synthesis of helical microtubules of graphitic carbon. With the use of arc discharge evaporation, he produced a new promising material - multi walled carbon nanotubes (MWNTs) [14]. Two years later he discovered single walled carbon nanotubes (SWNTs), an even more promising material [15]. In the following years nanotubes have been subject of intensive investigation, revealing their outstanding thermal, mechanical, and optical properties. Carbon nanotubes (CNTs) are materials consisting of carbon in its sp^2 form and can be pictured as rolled up sheets of graphene forming a tubular structure. Their diameters are in the range of a few nm and their lengths can reach up to several μm, making them quasi one - dimensional systems.
In this chapter I will give a short introduction into the main physical properties of SWNTs, focusing on their electronic, optical, and chemical characteristics.

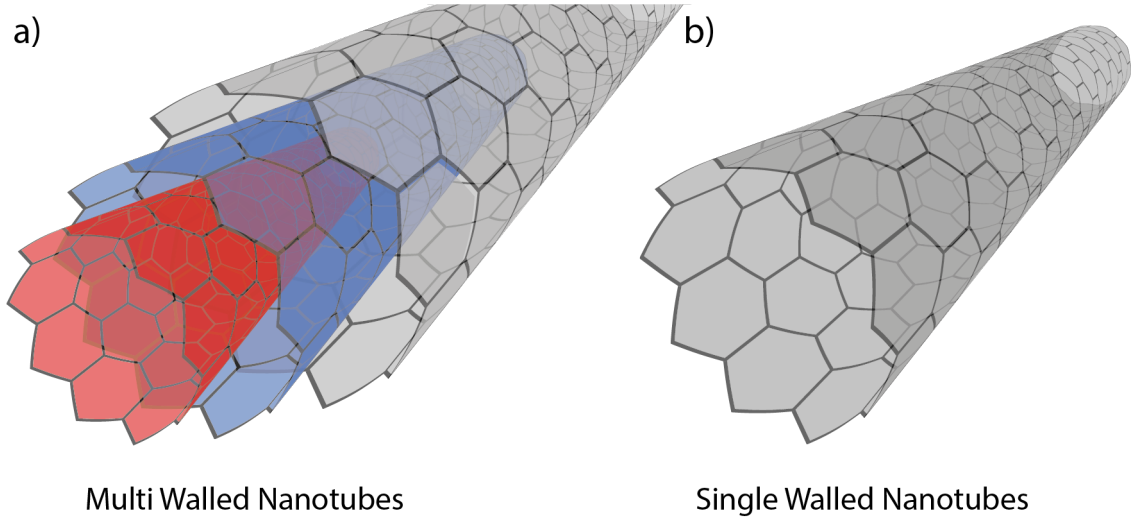

Fig. 2.1: Sketch of a a) multi walled and b) single walled carbon nanotube.

2.1 Hybridization of Carbon

Carbon can form different allotropes beyond SWNTs: Fullerenes, graphene, carbon fibres, diamond, and many other materials made of pure carbon. The origin of so many stable structures lies in the different molecular binding behaviour of carbon. Carbon is an ele-

ment with six electrons occupying different orbitals. Two electrons fill the 1s orbital in the core and the other four electrons are valence electrons in the $2s^2$ $2p^2$ configuration. The electrons can occupy the 2s, $2p_x$, $2p_y$, and $2p_z$ orbitals. The small energy difference between the 2s and 2p states leads to mixing of the orbitals and their occupation, causing different hybridization states. An electron in the 2s shell can mix with $n = 1, 2, 3$ 2p electrons resulting in an sp^n hybridized state. In the case of carbon, all three hybridization states are possible (sp, sp^2, and sp^3), giving rise to the different carbon structures. The **sp hybridization** is a linear combination of 2s and 2p. Two carbon atoms in their sp-hybridization state will establish a strong covalent σ-bond, separated by 180°, and two π-bonds between the remaining 2p electrons. The **sp^2 hybridization** occurs between the 2s and two 2p orbitals, revealing a trigonal structure with a separation of 120° to the neighbouring carbon atom, with in-plane strong σ-bonds and weak π-bonds in the vertical direction. The third hybridization state, the **sp^3 configuration**, has a tetragonal (109.5°) geometry with only σ-bonds between the neighbouring atoms. sp hybridized carbon can be found in one dimensional carbon system such as carbenes. In 2D planar carbon structures such as graphene or graphite an sp^2 configuration is present. Fullerenes and SWNTs are not 2D materials but they exhibit local planar structures also showing sp^2 hybridization, with a small degree of sp^3 hybridization due to curvature, for more details please refer to Section 2.5.1. The sp^3 configuration is the typical tetrahedral structure found in diamond. Figure 2.2 depicts the three hybridization states of carbon and associated allotropes. The different hybridization states give rise to different intrinsic physical properties of the resulting materials. The equal huge bonding strength in all directions in the sp^3 form makes diamond one of the strongest materials to be found in nature. The π-orbitals in the sp^2 structure give rise to weak inter-layer van der Waals (vdW) forces, which makes graphite a soft material easy to exfoliate. The hybridization state not only influences the mechanical properties of the material; it also strongly rules the optoelectronic characteristics of the resulting carbon allotrope. For a full description please refer to Ref. [16]. Within this thesis I will concentrate on SWNTs, an sp^2 hybridized carbon allotrope, focusing on their optoelectronic properties. I will investigate in detail the influence of different functionalization routines and moieties on their optical properties.

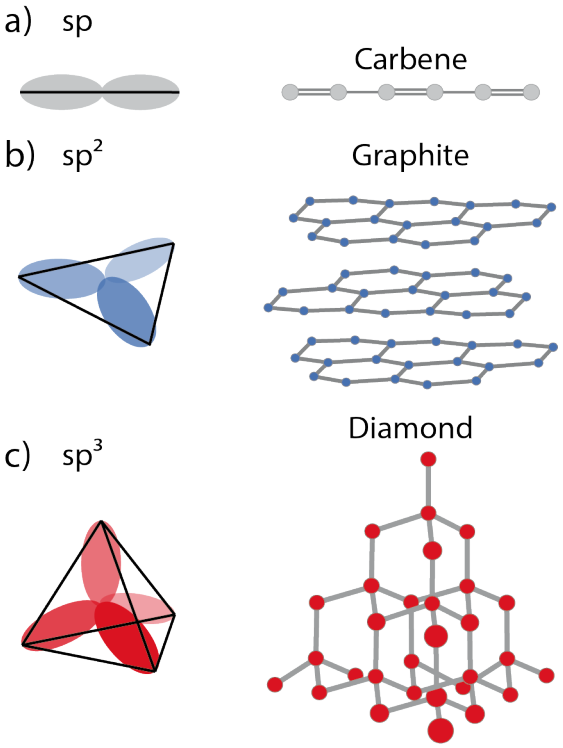

Fig. 2.2: Hybridization state of carbon and the corresponding allotropes. a) sp carbon and the allotrope carbene, b) sp^2 and the corresponding allotrope graphite, and c) sp^3 hybridized carbon and the associated diamond allotrope.

2.2 Structural Properties

SWNTs belong to the sp^2 hybridized carbon allotropes, consisting of carbon atoms arranged in a honeycomb structure. They can be pictured as a rolled-up sheet of graphene. According to the orientation and the length of the graphene sheet, different tube species are possible.

2.2.1 Real Space

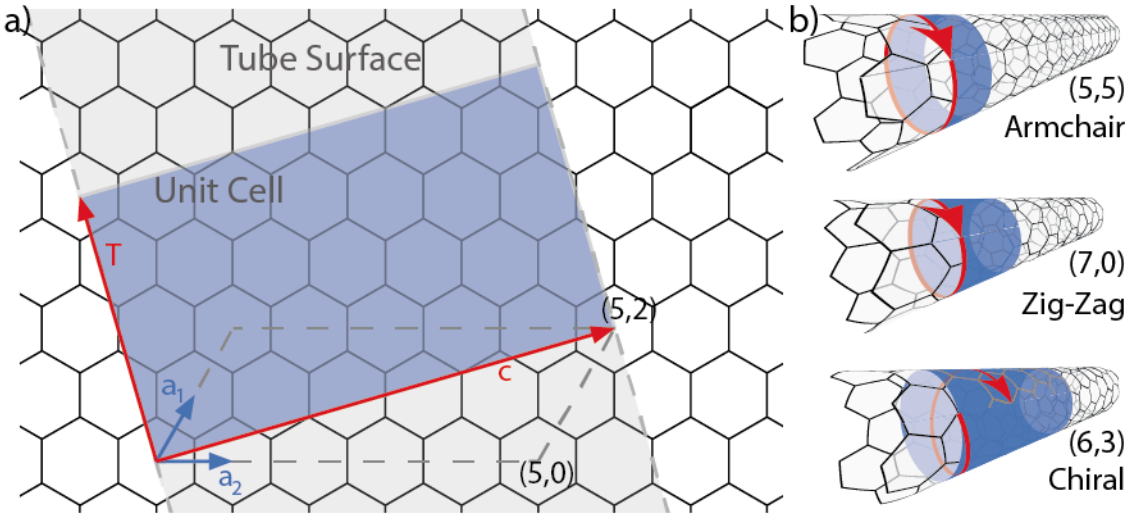

Fig. 2.3: a) Sketch of a graphene sheet: The blue arrows indicate the graphene unit vectors $\mathbf{a}_1$ and $\mathbf{a}_2$. The red vectors **T** and **c** outline the unit cell of a (5,2) SWNT. The light blue area depicts the graphene excerpt used to form the SWNT. b) Different SWNT types armchair, zig-zag and chiral. Adapted from [17].

Given the lattice vectors $\mathbf{a}_1$ and $\mathbf{a}_2$ of a graphene sheet, the circumferential vector, also called chiral vector **c**, can be defined as:

$$\mathbf{c} = n\mathbf{a}_1 + m\mathbf{a}_2, \tag{2.1}$$

where the integers n and m define the chirality (n, m) of the tubes. Figure 2.3 a) for example depicts the (5,2) vector extending two times along $\mathbf{a}_1$ and five times along $\mathbf{a}_2$, when rolling up it creates the tube with a (5,2) chirality. The combinations of n and m describes an infinite number of tubes. Given a certain chirality, the diameter d and the chiral angle θ of the tubes can be calculated. The diameter is obtained from:

$$d = \frac{|\mathbf{c}|}{\pi} = \frac{a_0\sqrt{m^2 + n^2 + nm}}{\pi}, \tag{2.2}$$

where a_0 is the length of the graphene lattice vector of 2.46 Å.
The chiral angle is defined by:

$$\cos\theta = \frac{\mathbf{a}_1 \cdot \mathbf{c}}{|\mathbf{a}_1| \cdot |\mathbf{c}|} = \frac{n + m/2}{\sqrt{m^2 + n^2 + nm}}. \tag{2.3}$$

The vector perpendicular to **c** is the translational vector **T** which is defined as:

$$\mathbf{T} = \frac{2m+n}{nR}\mathbf{a}_1 - \frac{2n+m}{nR}\mathbf{a}_2 \tag{2.4}$$

and with length

$$T = |\mathbf{T}| = \frac{\sqrt{3n^2+nm+m^2}}{NR}a_0, \tag{2.5}$$

where N is the greatest common divisor of n and m and R is defined as:

$$R = \begin{cases} 3 & \text{if } (n-m) \text{ is an integer} \\ 1 & \text{otherwise} \end{cases} \tag{2.6}$$

The different tubes can be grouped into three structural types: Armchair, zig-zag, and chiral tubes. The armchair and zig-zag tubes are achiral tubes with high symmetry. Armchair tubes have equal integers ($n = m$) and a chiral angle of 30° (*e.g.* the (5,5) tube in Fig. 2.3 (upper tube), whereas zig-zag tubes have a chiral angle of 0° resulting from one integer being equal to zero $(n, 0)$ (Fig. 2.3 (middle tube). Arbitrary values for (n, m) with $m < n$ lead to chiral tubes with an angle between 0° and 30°, as seen in Fig. 2.3 (bottom tube).

2.2.2 Reciprocal Space

The reciprocal lattice vector of graphene is obtained through the relation $a_i \cdot k_j = 2\pi\delta_{ij}$:

$$\mathbf{k}_1 = \left(\frac{1}{\sqrt{3}}, 1\right) \cdot \frac{2\pi}{a_0},\ \mathbf{k}_2 = \left(\frac{1}{\sqrt{3}}, -1\right) \cdot \frac{2\pi}{a_0}. \tag{2.7}$$

In the Brillouin zone of a graphene sheet **k** can take any value. For SWNTs, periodic boundary conditions apply along the circumference for $\mathbf{k}_\perp$:

$$\mathbf{k}_{\perp,l} = \frac{2\pi}{\lambda} = \frac{2\pi}{|\mathbf{c}|} = \frac{2}{d}l, \tag{2.8}$$

l is an integer between $-\frac{q}{2}+1, ...0, 1, ...\frac{q}{2}$ and λ is the wavelength. The tube axis can be considered continuous in the interval of $[-\pi/|\mathbf{T}|, \pi/|\mathbf{T}|]$, since $L \gg \lambda$. Now the reciprocal lattice vectors of the tube can be derived :

$$\begin{array}{cc} \mathbf{k}_\perp \cdot \mathbf{c} = 2\pi & \mathbf{k}_\perp \cdot \mathbf{T} = 0 \\ \mathbf{k}_z \cdot \mathbf{c} = 0 & \mathbf{k}_z \cdot \mathbf{T} = 2\pi \end{array} \tag{2.9}$$

yielding:

$$\mathbf{k}_\perp = \frac{2n+m}{qgR}\mathbf{k}_1 + \frac{2m+n}{qgR}\mathbf{k}_2, \tag{2.10}$$

$$\mathbf{k}_z = \frac{m}{q}\mathbf{k}_1 + \frac{n}{q}\mathbf{k}_2. \tag{2.11}$$

A general nanotube wave vector **k**, thus, can be written as:

$$\mathbf{k} = k_{\parallel} \cdot \frac{\mathbf{k}_z}{|\mathbf{k}_z|} + l \cdot \mathbf{k}_{\perp}. \tag{2.12}$$

Figure 2.4 depicts the resulting Brillouin zones. The dashed lines represent the allowed **k** vectors along the tubes axis. For a full derivation of the structural properties of SWNTs please refer to Ref. [18].

2.3 Electronic Properties

In the previous section the relation between SWNTs and graphene was exploited to describe the structural properties of SWNTs. A similar strategy will be applied to derive the electronic properties of the tubes. One primitive graphene unit cell contains of two carbon atoms, each of them having four electrons in its outer shell. The sp^2 orbitals created by the electrons are symmetric with respect to the planar graphene sheet and mix with neighbouring equivalent orbitals, creating three bonding σ and three antibonding σ^* bands. Only the σ-bonds are occupied by electrons while the σ^* are unoccupied. The bonding bands are located below the Fermi energy (E_F) making their contribution to the electronic properties negligible. Two of the eight electrons occupy the p_z orbital. Adjacent p_z orbitals interact with each other, forming delocalised π/π^*-bands above and below the graphene sheets, which is at the origin of its extended conjugated network. The E_F (set at 0 eV) is located within those bands (see Figure 2.4).
The electronic properties close to the Fermi energy of graphene, thus, can be derived by only considering the bands originating from the p_z orbitals. Using them as the basis for the tight binding calculation which yields the following eigenvalues:

$$E^{\pm}(\mathbf{k}) = \frac{\epsilon_{2p} \pm \gamma_0 \sqrt{f_{12}(k_1, k_2)}}{1 \pm s_0 \sqrt{f_{12}(k_1, k_2)}}, \tag{2.13}$$

where k_1 and k_2 are the components of the wave vectors and ϵ_{2p}, γ_0 and s_0 empirical parameters. The function f_{12} is a cosine dependent on k_1, k_2 which disappears at the K point for ($k_1 = \frac{1}{3}$) and ($k_2 = -\frac{1}{3}$). For a full derivation please refer to Ref. [18].
The dispersion relation of graphene depicted in Figure 2.4a) and b) shows the main characteristics of the band structure: The π and π^*-band cross at the K points with a linear behaviour around the Fermi level (E_F) and the smallest σ-σ^* band distance at the Γ-point, making graphene a semimetal. The linear behaviour at the K points give rise to a conical structure - the Dirac cones, giving the electrons in graphene a peculiar character that is not shared by standard metals. The linear parts mainly govern the optical and electronical properties of graphene. Graphene shows remarkable transport properties with a Fermi velocity of 10^6 ms^{-1} [19]. It absorbs a considerable amount of incident white light for a single layer with a constant absorption of 2.3% [20].

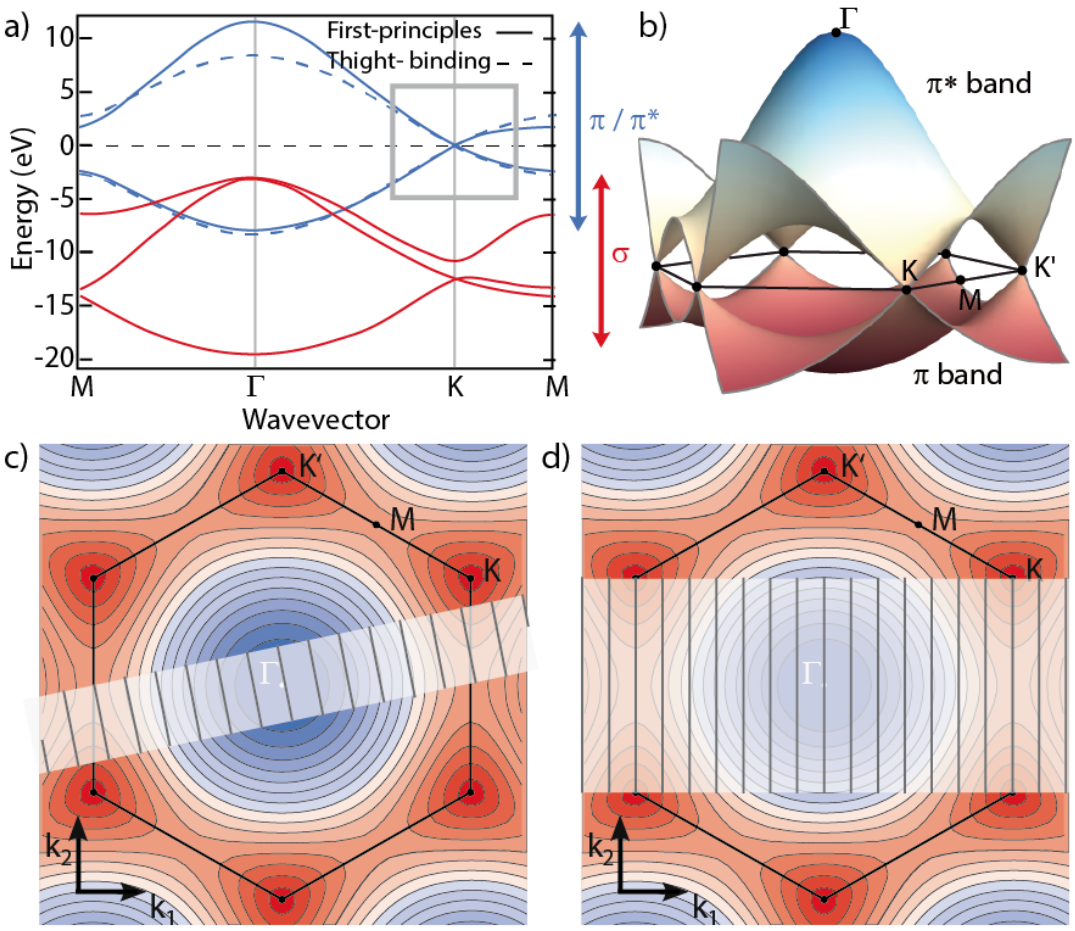

Fig. 2.4: a) Bandstructure of SWNTs. b) Energy dispersion relation of graphene: The conduction and valence band touch at six discrete points - the K points. Contour plot of the electronic structure of graphene with overlayed nanotube Brillouin zones (dashed lines). The band structure in c) belongs to a semiconducting nanotube (8,4) and none of the K points is an allowed state. d) Depicts the band structure of a metallic nanotube (7,7); note how the vector crosses the K points. Adapted from [17]

In order to link the band structure of graphene to the band structure of SWNTs the periodic boundary conditions need to be considered, following the so called zone folding method. The method is based on the assumption that rolling up of the graphene sheet into a tubular structure does not alter its dispersion relation. The nanotube dispersion relation, under this assumption, can be obtained by selecting the states compatible with the periodic boundary conditions dictated by the chiral vector **c**. The symmetry of the SWNTs gives rise to two distinct sets of tubes: Metallic or semiconducting. If the allowed **k** vectors do not pass through the K point, the tubes are semiconducting as depicted in Figure 2.4d). If the allowed **k** vectors include the K point, the tube is metallic. The so-called zone folding approximation results in the following correlation: If $mod_3(n-m) = 0$ the tubes are metallic and if $mod_3(n-m) = 1, 2$ the tubes are semiconducting.

One refers to big and small band gap semiconducting nanotubes to differentiate between the semiconducting tubes. The differences arise from the trigonal warping effect, which causes an asymmetry in the graphene dispersion relation around the K point. As it can be seen in the grey highlighted box in Fig. 2.4a), the energetic separation between the π-π^*-bands on the left of the K point is higher than the energy separation on the right. This makes the transition energies of the tubes on the left bigger than expected in a purely symmetric case and the ones on the right smaller. Kataura systematically highlighted this dependence by creating the plot bearing his name [22]. In a purely symmetric case, one would expect the transition energies of the tubes to scale inverse with the diameter (1/d). The trigonal warpping effect is responsible for deviations from this trend generating the different branches in the Kataura plot. The nanotubes belonging to each of these branches belong to the same so called *laola* family sharing the same family index $q = 2n + m$. Fig 2.5 depicts an example of a Kataura plot.

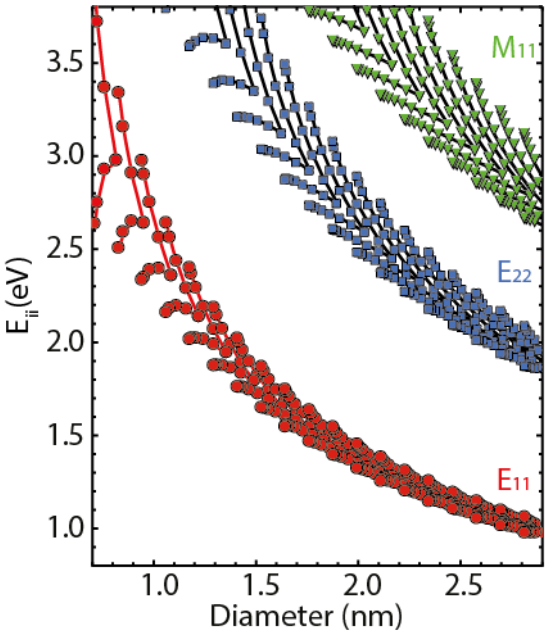

Fig. 2.5: Kataura plot depicting the diameter dependence on the semiconducting ($E_{11}$and E_{22}) and metallic M_{11} transition energies. Adapted from Ref. [21].

2.4 Optical Properties

The photoluminescence (PL) of SWNTs was first observed by O'Connell *et al.* and since then PL spectroscopy became a powerful tool to analyse SWNTs [23]. The crucial point in such analysis is to debundle and isolate individual tubes. In bundles inter-tube interactions occur, an excitation created in a semiconducting tube can cross into a neighbouring metallic tube, suppressing the luminescence due to fast non-radiative recombination channels. O'Connell *et al.* could individualize and stabilize SWNTs by applying horn sonication combined with the aid of surfactants.

2.4.1 Optical Transition

To describe the optical properties of SWNTs one needs to analyse their density of states (DOS). As an one dimensional materials, their DOS are described by a sequence of van Hove singularities (vHs). The full derivation of the DOS for SWNTs can be found in Ref. [24].

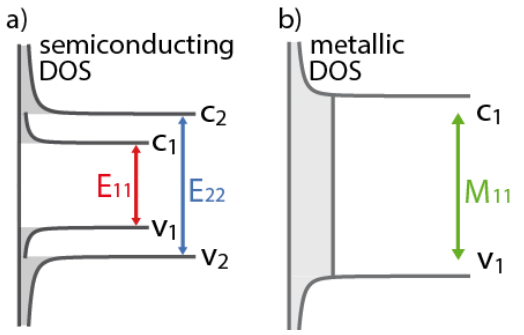

Fig. 2.6: DOS for a) a semiconducting and b) a metallic nanotubes. Adapted from Ref. [21].

Optical transition will take place between the sub-bands described by the vHs (see Fig. 2.6) and are dictated by the selection rules: Photons polarized parallel to the tube axis induce transitions between the valence (v_i) and conduction band (c_i) of the same index, given by the energy E_{ii}. Perpendicularly polarized light with respect to the tube axis will activate transition between sub-bands of v_{i+1} and c_i, given by the Energy $E_{i+1,i}$. Those transitions are suppressed in SWNTs due to depolarization, the so called antenna effect. Optical properties of SWNTs are thus limited to the transition between complementary vHs on opposite sides of their Fermi level (see for example Fig. 2.8).

2.4.2 Photoluminescence

For many years the optical processes in SWNTs were ascribed to single-particle band-to-band transitions. In the single-particle picture, the process is explained by the excitation of an electron from the conduction band into the valence band (E_{22} transition in Fig. 2.8a) of the vHs, followed by non-radiative relaxation into the lower sub-bands. Finally they radiatively recombine into the valence band (E_{11} in Fig. 2.8a) with the emission of a photon. The single particle picture helped assigning chiralities according to their transition energies. However, experiments revealed a discrepancy with the theoretically predicted values for the transition energies. The single particle picture predicts a ratio of 2 for the E_{11} and E_{22}, whereas the experimental results showed a ratio of 1.8.
In 2005, two photon experiments revealed the excitonic nature of optical processes in SWNTs pointing towards many body effects in the optical processes of SWNTs [25].

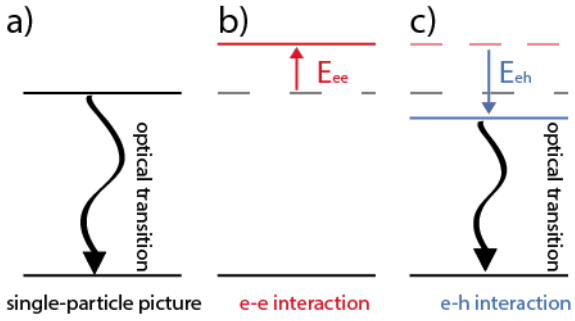

Fig. 2.7: Energy diagram of a) the bandgap for the single particle picture, b) the increase of the energy due to the electron electron interaction, and c) for the excitonic picture. Adapted from Ref. [26].

In the excitonic picture, the electron is excited from the valence into conduction band leaving a hole in the valence band. The positively acting hole and the electron are bound together via Coulombic interaction, forming an exciton. The excited electron senses a repulsive force from the remaining electrons in the valence band. Consequently, additional interactions must be considered in the many body picture: The single particle bandgap $E_{g,ii}$ is renormalized by the repulsive e-e interaction and increases the

energy of the excited states E_{ii}^{e-e}. The binding energy of the exciton on the other hand decreases the energy due to attractive Coulomb interaction between the electron and the hole $E_{ii}^{e-h}(< 0)$. The excitonic bandgap is redshifted compared to the single particle picture (see Fig. 2.7) and hence explains the ratio problem [27], [28]. The optical transition energy E_{ii} between the i-th valence and the i-th conduction band is given by:

$$E_{ii} = E_{iigr} + E_{iiee} + E_{iieh}. \tag{2.14}$$

In the many particle picture, the fundamental photoluminescence process remains the same: excitation, relaxation, recombination. However, the additional interactions lead to a redshift in the transition energies with respect to the single-particle picture. The transitions denoted as E_{22} and E_{11} will not refer any longer to inter band transition but rather indicate excitonic transitions.

2.4.3 Photoluminescence Excitation Spectroscopy

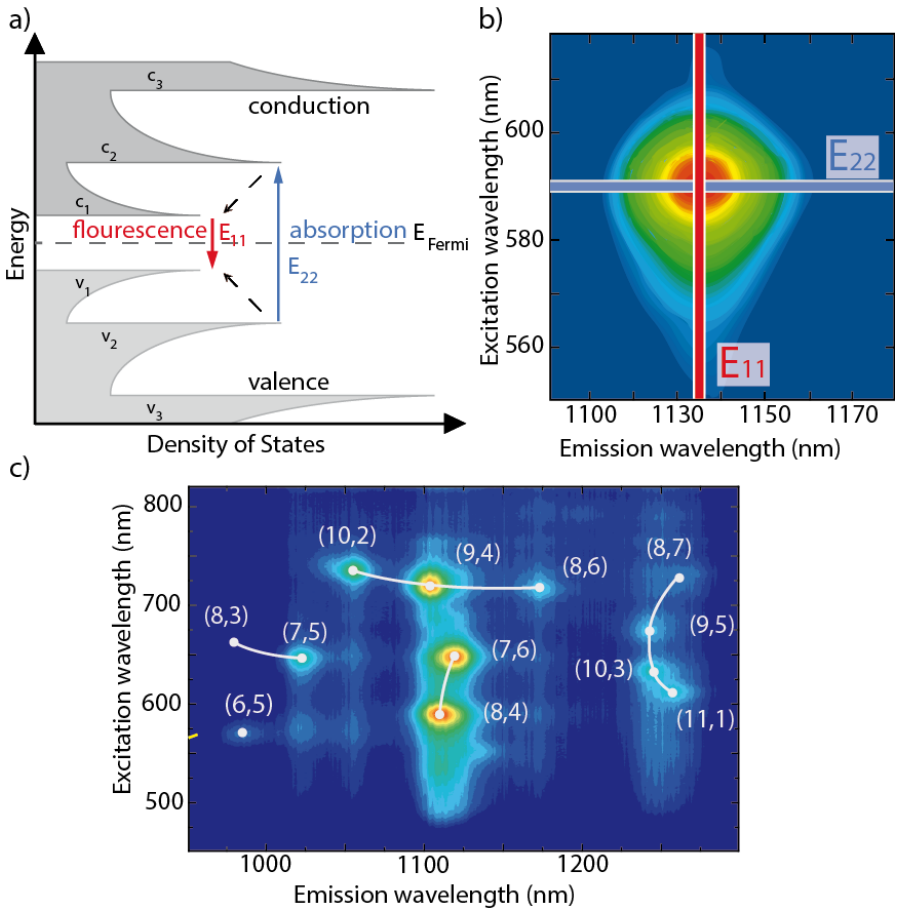

Fig. 2.8: a) Schematic PL process: Absorption of a photon with energy E_{22} creates an electron hole pair in the second valence and conduction band, followed by internal relaxation into the ground state and subsequently radiative recombination. b) Excerpt of a PLE map indicating the excitation and emission energy of the (7,6) SWNT. c) PLE map of a nanotube solution. Adapted from [17].

Each chirality has a distinctive set of excitation and emission transition energies which identifies univocally a specific nanotube. Figure 2.8 depicts the intrinsic transition wavelength for the (7,6) tube. The tube is excited at a wavelength of 590 nm which then shows an emission at 1130 nm. This set of excitations (E_{22}) and emission (E_{11}) values is unique for the (7,6) tube. Knowing those two numbers, one can identify the actual chirality composition of a nanotube sample. In order to experimentally analyse a certain nanotube sample, one gradually increases the energy of the photons tuning through a certain excitation range (visible region). Simultaneously the emission energy (infrared region) is detected. This method, called photoluminescence excitation (PLE), results in a photoluminescence excitation map depicted in Figure 2.8c). Each individual spot represents a specific set of excitation and emission energy, corresponding to one special chirality. The tubes connected by continuous lines belong to the same *laola* branch of the Kataura plot.

2.4.4 Environmental Effects on the Optical Properties

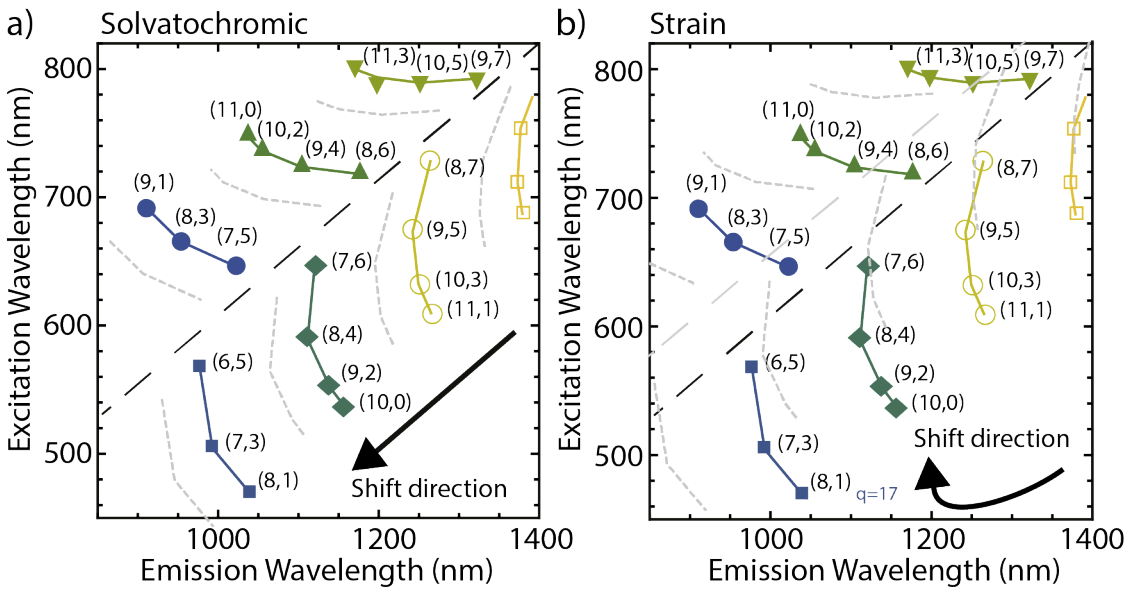

Fig. 2.9: a) Solvatochromic shifts of the SWNTs induced by environmental changes and b) shifts caused by strain.

The optical transition energies of SWNTs are extremely sensitive to changes in the environments. Changing the dielectric environment by attaching molecules, wrapping SWNTs with polymers, or encapsulation by micelles induces shifts in the transition energy. The influence of the medium on the energy of electronic states are called solvatochromic shifts. They describe the impact of a different medium on the SWNTs or a molecule in general. Choi *et al.* introduced a model to relate the spectral shifts resulting from the differences in exciton polarizability for various media [29]. The model shows linear relation between the solvatochromic shift and the tube diameter to the power of -4, indicating the magnitude of the interaction between the SWNTs and their surrounding. Please note, that the application of external forces such as strain can also lead to changes in the optical properties but with opposite sign of the shift between

$\Delta E_{11}$and ΔE_{22} [30]. The effects are sketched in Fig. 2.9. Other effects, in particular the effect of dipoles placed in the proximity of the tubes will be described in Chapter 5.

2.5 Chemical Properties

The fundamental properties of the SWNTs were obtained in the so-called zone-folding approximation. In this picture, the SWNTs is depicted as rolled up sheets of graphene, forming a one-dimensional tube. The electronic wavefunctions of the SWNTs are then obtained from the continuum of the graphene states by selecting the ones obeying the periodic boundary conditions. This approximation assumes that the induced curvature of the carbon network due to the rolling up process does not alter the hybridization nature of the carbon atoms themselves. The curvature though influences the reactivity of the SWNTs.

2.5.1 Curvature and Reactivity

In an ideal situation graphene is a planar, defect free honeycomb structure of sp^2-hybridized carbon atoms. Such aromatic macromolecules are chemically inert. SWNTs, however, are curved structures. While this does not significantly influence their optical response (at least for the diameter ranges of the standard commercially available tubes used in optical experiments), it does induce strain into their skeletal network. This influences the reactivity of the tubes: The strain induced by the curvature of the tubes induces a partial rehybridization of the sp^2 towards sp^3 state. The higher the strain, the closer they get to the sp^3 state and the stronger they aim for relaxation through chemical reactions. Thus, the stronger the curvature of the carbon allotropes, the higher is their affinity towards chemical reaction.

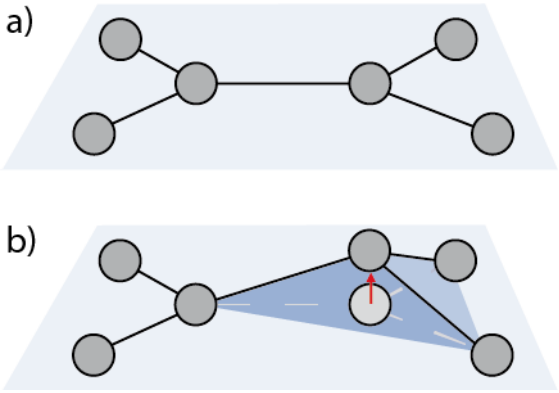

Fig. 2.10: a) Sketch of the unstrained carbon network in SWNTs. b) Strain induced in the skeletal carbon network.

To understand the origin of the reactivity of SWNTs two quantities need to be introduced: The pyramidalization angle, which is closely connected to the curvature and diameter of a certain tube, and the misalignment between the π-orbitals. The pyramidalization angle θ_p is defined as the angle between the π-orbital and the σ-bond minus 90°. According to the hybridization state and the curvature of the carbon allotrope, different values for θ_p are possible. In a pure planar sp^2 hybridization state $\theta_p = 0°$, whereas for carbon in the pure sp^3 state $\theta_p = 19{,}5°$. For curved sp^2 systems, such as fullerene and carbon nanotubes, different angles are observed. Both systems possess curved carbon structures but they mainly differ in dimensionality [31]. In fullerenes the curvature occurs in two dimensions, whereas for SWNTs the curvature is only

present along their circumference. Thus, the degree of distortion in fullerenes is higher, yielding higher reactivity than for the tubes. The (10,10) SWNT, with a radius of 1.3 nm, e.g. displays a pyramidalization angle of $\theta_p = 3.0°$ whereas the C_{240} fullerene, with the same diameter, shows a higher pyramidalization angle of 9.7°. The higher the convexity of the surface, the higher the strain, resulting in higher affinity towards addition reactions [32].
The second mechanism affecting the reactivity of the tubes is the misalignment of the π-orbitals. Even though fullerenes are highly strained objects, their π-orbitals remain perfectly aligned. The distortions necessary for closure of the fullerene structure involves carbon atom pyramidalization rather than a twisting around the carbon-carbon π-bond, thus no additional strain is introduced [33]. In SWNTs, two different types of bonds can be found. For example the (5,5) zig-zag tube shows a bond running perpendicular to the tubes' axis and the other with a specific angle to the circumference. For the orbitals perpendicular to the axis, no misalignment occurs, yielding a misalignment angle φ of 0°. In the second case, the π-orbitals show a misalignment with an angle of 21.3° as seen in Fig. 2.11d). For Fulleroids it has been shown that the reactivity could be mainly connected to the misalignment of the π-bonds, which is applicable for SWNTs as well [32]. Calculations and experiments further demonstrated the change in reactivity when increasing the strain in certain regions by bending the SWNTs [34]. The reactivity of carbon allotropes is strongly related to strain induced by the curvature of the structure. In fullerenes, the reactivity mainly originates from strain due to the pyramidalization angle whereas the strain in SWNTs mainly originates from the twisted double bonds. The misalignment of the π-orbitals determines the reactivity of the SWNTs. Both mechanism scale with the diameter, resulting in diameter dependent reactivity.

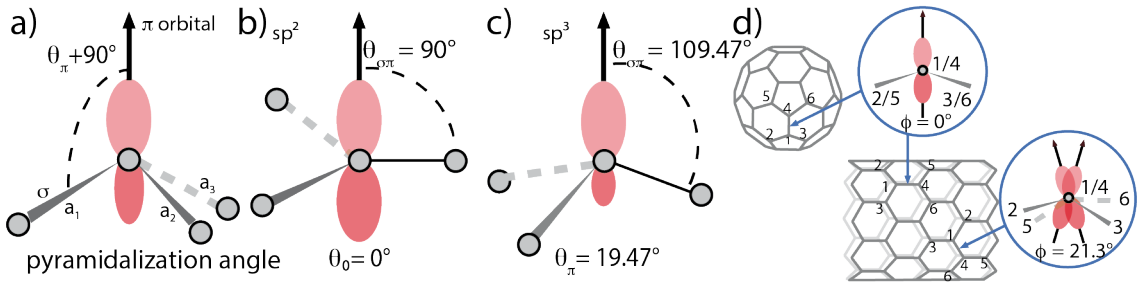

Fig. 2.11: a) Schematic illustration of the pyramidalization angle. Orbital configuration for a b) sp^2 and c) sp^3 configuration and the corresponding pyramidalization angle θ_p. d) The π-orbital misalignment angles along the C_1-C_4 bond in a (5,5)-SWNT and C_{60}. Figure adapted from Ref. [35] and [31].

2.5.2 Stacking and Insolubility

Most SWNT applications call for individualized nanotubes and stable tube dispersions. Due to their structural characteristics SWNTs tend to agglomerate and form bundles, resulting in low dispersibility. The typical honeycomb structures of SWNTs originates from the sp^2 hybridization of the carbon atoms. In the xy-plane the electrons are separated by 120° and in the z-axis the electron is delocalized in a p_z orbital, giving rise to van der Waals forces. The

delocalized π-electrons further promote the adsorption of other aromatic moieties through π-π-stacking, including other SWNTs. This interaction is intensified through the high SWNTs aspect ratio. The increased surface area amplifies the attractive forces. The high flexibility of SWNTs enables strong entanglement and dense packing of the tubes. A typical bundle may contain 100-500 SWNTs that are tightly bound by vdW attraction energy of 500 eV/μm per tube-tube contact [36], [37]. As highlighted in Section 2.4.2 bundling is detrimental for the optical response of the tubes. Figure 2.12 depicts SEM and TEM pictures of SWNTs bundles. The strong bundling affinity makes the isolation, dispersion and homogeneous functionalization of SWNTs quite difficult. Strong external forces need to be applied in order to debundle the tubes. In the next chapter different functionalization processes will be introduced, solving this issue.

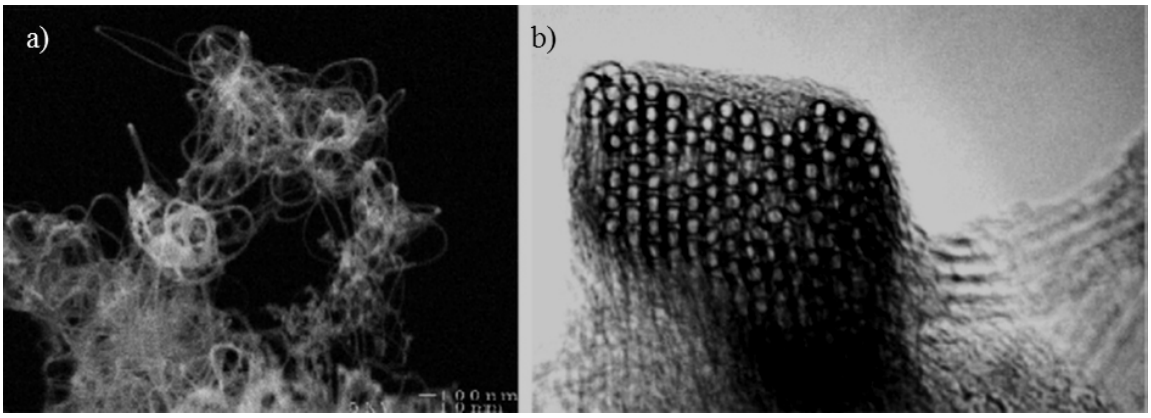

Fig. 2.12: a) SEM picture of stacked and agglomerated SWNTs. b) TEM image of a SWNT bundle. Taken from [38].

3 Functionalization Routines

In the previous chapter, I provided a general theoretical introduction on SWNTs. The basic physical properties were explained, focusing on the intrinsic optical characteristic of SWNTs. In the last part, I highlighted the main drawback of SWNTs: The affinity to form bundles and their insolubility in most solvents makes it challenging to tailor their surface and properties. In this chapter, I will focus on the functionalization of SWNTs. The aim is to tailor the optical properties of SWNTs in a controlled way, realizing SWNT hybrids with new outstanding properties, empowering new kinds of applications. The major task is to find a way to immobilize the functional moiety onto the surface of SWNTs without compromising the conjugation of the sp^2 network and the optical properties of the tubes. Utilization of SWNTs requires customizing the raw SWNTs to overcome the bundling and unwetting behaviour and anchor functional components on the SWNTs sidewall. Here I want to give a further inside into the three main functionalization approaches: The endohedral, exohedral covalent, and exohedral non-covalent functionalization.

3.1 Endohedral Functionalization

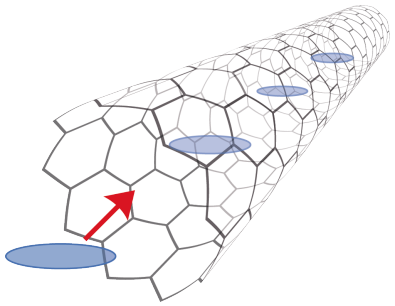

Fig. 3.1: Endohedral filling of a carbon nanotube.

During the endohedral functionalization process, the molecule is inserted in the nanotubes inner core as seen in Fig. 3.1. To fill the nanotube three different mechanism may be applied: Sublimation, immersion, and transport. If the material can be vaporized, it will be heated up to the sublimation point. The molecule will adsorb onto the sidewall and will migrate towards the side ends of the tubes. If the molecule overcomes an activation barrier, it ends up encapsulated inside the tubes. The optimum setup can be found if the difference between the inner tube diameter and the size of the molecule are in the range of the van der Waales gap of 0.3 nm. If this criterium is not met, the molecule will not enter the tube. Note that the molecule needs to have a diameter smaller than the tube. However, if the tube diameter is too big, the vdW interaction decreases, leading to inferior interplay.

The other possible mechanism is the immersion of SWNTs in a liquid. If the surface tension is below 0.2 N/m, the tubes will be spontaneously filled. This effect is connected to capillary effects. It must be pointed out that for most nanotubes (below 8 nm in diameter) the classical approximation is not valid anymore and the liquids experience an anomalous behaviour. This capillary filling also counts for ionic compounds, here the SWNTs are immersed in molten salts or eutectic mixtures. The last class is the insertion of substances which neither sublime nor melt. Those components need to be transported into the nanotube with the help of solvents [39]. A prominent example is the filling of SWNTs with water molecules, which was observed by Cambrè *et al.* [40]. The water molecules enter the SWNTs during the debundling process with surfactants: The strong sonication applied to disentangle the tubes breaks their caps, making it possible for the water molecules to enter the nanotubes. The presence of the dipoles of the water molecules induces a redshift of the tubes' emission. SWNTs have also been filled with fullerenes, creating the so-called pea pods [41]. SWNTs for in vivo imaging have, moreover, been filled with radionucleotides [42]. If the filling process is performed at high temperatures, the subsequent heat dissipation reverses the cap breaking process, resulting in sealing of the side lids of the tubes [43]. The endohedral filling technique can be exploited for various functionalities, ranging from organic to inorganic substances.
The major drawback of endrohedral functionalization is the strongly limited spatial extension of the tubes inner cavity, which is around 2 nm for the largest tube diameter. Bigger functional moieties have to be attached to the outer surface of the tubes. This can be done either non-covalently or covalently. In this work I will focus on the comparison between these two functionalization routines and the effects on the SWNTs optoelectronic properties.

3.2 Non-Covalent Functionalization

The gentlest way to chemically modify SWNTs is the non-covalent functionalization routine. The aimed moieties can be placed in the proximity of the SWNTs via physisoprtion such as polymer wrapping, micellar suspension or π-π-stacking. The non-covalent functionalization ensures non-perturbing functionalization, as neither the sp^2 network nor the π-conjugation is disturbed, preserving the intrinsic properties of SWNTs. A drawback of the procedure, on the other side, is the instability towards environmental changes, such as changes in the pH or temperature, dropcasting onto surfaces, etc.

3.2.1 Surfactants

The most prominent non-covalent chemical procedure applied to SWNTs is the debundling through surfactants (*abbr.* for surface active agents). They adsorb at surfaces and interfaces, mixing two immiscible phases. Surfactants are amphiphilic ($\alpha\mu\varphi\iota$- amphi greek for both and $\varphi\iota\lambda\iota\sigma$- philos for loving) structures, consisting of water soluble heads and hydrophobic tails. When inserted into water, the unimers aggregate forming micelles. To minimize the total

energy and entropy of the system, they build up structures in which the hydrophobic tails orient towards each other, exposing the hydrophilic head outwards, facing the water.

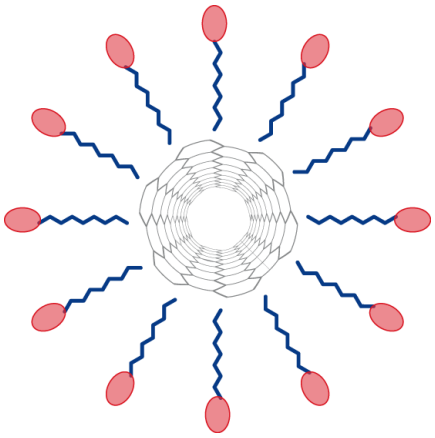

Fig. 3.2: Surfactant forming a micelle which encapsulates a SWNT.

The use of surfactants overcomes one of the biggest challenges - the water insolubility of SWNTs due to their hydrophobic nature. Surfactants help to isolate and exfoliate the SWNTs. The hydrophobic tail of the surfactants attaches to the nanotubes and solubilizes them in water by forming a micelle with a hydrophilic outer shell, enclosing the hydrophobic SWNT in their inner core (see Fig. 3.2). The range of available surfactants is huge: The head may be anionic to cationic and non-ionic and, furthermore, the tail may have alkyl chains of various length or other groups [44]. Each surfactant forms its own peculiar micellar structure at certain concentration, realizing different micelle morphologies, favouring certain tube chiralities.

Three main micelle structures form around SWNTs: Cylindrical micelles, hemimicelle and the randomly adsorbed surfactants [45]. Wenseeler *et al.* performed a study on bile salt surfactants analyzing their individualizion behavior and stability in water [46]. Specific surfactants with special symmetries also show chiral selectivity [47], [48]. To investigate such effects, polyglycerol based surfactants were customized by incorporating different aromatic cores. In Ref. [49] we showed that changes in the structure of the amphiphiles resulted in chiral selectivity of the tubes suspension. We showed that by adding more aromatic cores tubes with bigger family indexes were more efficiently dispersed. Additionally, when mixing surfactants and applying density gradient ultracentrifugation nanotubes can be sorted by their electronic character (semiconducting from metallic), chirality and even enantiometric form [50].
Surfactants not only can be used to individualize and sort tubes: By designing smart surfactants, one can incorporate advanced functionalities into the surfactant, as shown for example by Ernst *et al.* [51]. They designed a surfactant consisting of an alkyl tail for tube exfoliation, a perylene core, and dendric head for water solubility. Via π-π-stacking the perylene adsorbs onto the SWNTs while the tail and head debundle and stabilize the tubes. They not only proved that the custom designed surfactant worked efficiently as a debundling agent but further demonstrated energy transfer from the perylene to the tubes. The interaction between perylene and SWNTs will be discussed in more detailed in Chapter 6.

3.2.2 π-π-stacking

π-π-stacking or π-π-interaction refers to the non-covalent interaction between the π-bonds of two aromatic rings. Functionalization of SWNTs via aromatic molecules has been proven to be

successful [52], [53]. Aromatic fragments such as perylene, pyrene and porphyrin adhere on the SWNTs sidewalls via π-π-stacking as depicted in Figure 3.3. These fragments can, furthermore, serve as anchors to attach additional moieties in the proximity of the tubes [52].

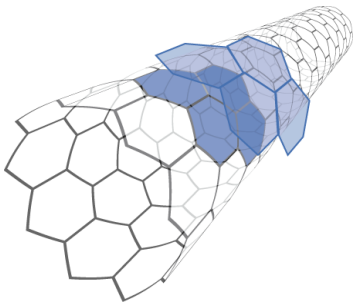

Fig. 3.3: Pyrene stacking onto a SWNT via π-π-interaction.

A correlation between the size of the π-electronic system of the molecule and the adsorption strength was experimentally and theoretically found [39]. The larger the π-electronic system of the molecule, the greater the adsorption energy. This clearly indicates that the coupling is controlled by the interaction between the π-electrons of the molecule with the π-system of the SWNTs [39]. π-π-stacking found a broad application in photoelectrical application. Pyrene derivatives have been immobilized on the SWNTs sidewalls realizing nanosized electron donor acceptor ensembles. Bluemmel *et al.* showed that pyrene, moreover, acts as an anchor for attaching the molecular switch spiropyran on the SWNTs to investigate the influence of the molecular dipole moment on the SWNTs [54].

3.2.3 Micelle swelling

The micelle swelling approach is particular easy functionalization methods as it requires no anchoring group to ensure close proximity of the functionality to the nanotubes sidewall. Wang *et al.* introduced a routine to optimize the micellar structure of surfactants encapsulating SWNTs. They observed that the addition of water-immiscible organic solvents leads to swelling of the micelle and favoured the reorganization of the surfactant after the solvent evaporated [55]. Roquelet *et al.* elaborated this effect and established a new routine to coat SWNTs with molecular moieties. They used the solvent to transport the organic molecule porphyrin within the micelles solubilizing the SWNTs. This let them study the energy transfer between porphyrins and SWNTs [56]. Kreft *et al.* demonstrated that micelle swelling could be used to carry the orthogonal switchable molecules (DHA/VHF) into the micelles close to the SWNTs while retaining the molecule switching ability [57]. Micelle swelling can be adapted to create plasmonic hybrids comprising metallic nanoparticles and SWNTs and to create nano-reactor environments to trigger polymerization around the SWNTs to establish a bridge between covalent and non-covalent functionalization of the tubes [58]. Micelle swelling is beneficial in several ways; the micellar forces ensure the tubes and switches to be confined within the hydrophobic core, providing direct proximity between nanotube and functional component. It provides excellent solubilization of the tubes and allows to control the functionality-to-tube ratio within the micelles and thus the nanotube coverage by the attached molecular moiety.

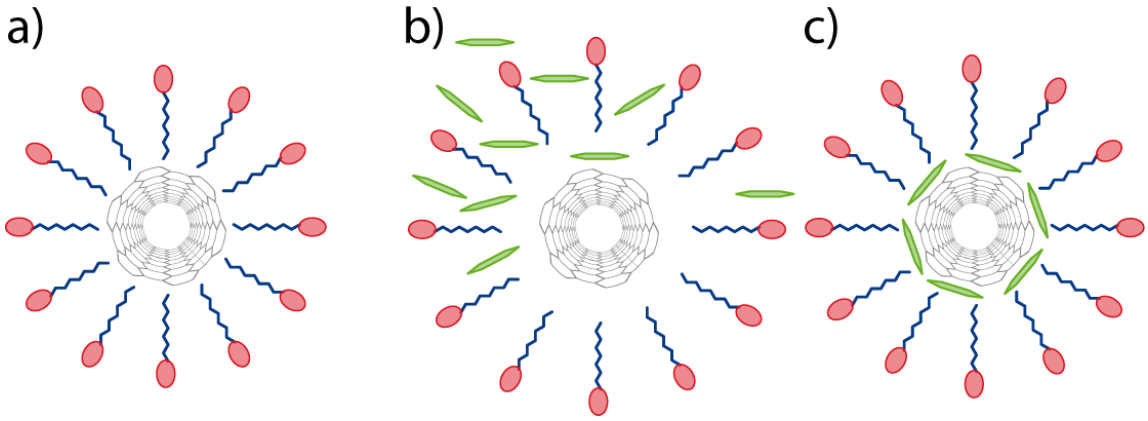

Fig. 3.4: Scheme of the micelle swelling approach: a) Micelle suspended SWNTs in water. b) After the addition of the organic solvent containing the molecule, both start to penetrate the micelle. c) The solvent will evaporate and the molecules will be encapsulated within the micelle core and arrange themselves around the SWNTs. Taken from [9].

Figure 3.4 schematically depicts the micelle swelling process. Molecular agents that are insoluble in water are solubilized in organic solvents and added to a solution with SWNTs suspended in surfactant micelles, Fig. 3.4a). While stirring, the molecular agents are transported by the organic solvent into the hydrophobic environment of the micelles' inner-core, Fig. 3.4b). After a while, the organic solvents evaporate and the molecules are enclosed within the micelles already containing the SWNTs, Fig. 3.4 c). The micelle swelling thus ensures a strong interaction between SWNTs and molecular moieties, which increases the interaction with the tubes compared to other functionalization approaches, ensuring a contiguous position on the nanotubes surface. In Chapter 5 I will show how the micelle swelling approach can be used to investigate the interaction of SWNTs with molecular dipole switches. Chapter 7 will discuss how the method can be used to achieve plasmon enhanced emission of carbon nanotubes nanometallic hybrids.

3.2.4 Polymer wrapping

The ethimology of the word polymer originates from the Greek meaning $\pi o\lambda\acute{\upsilon}$-poly = many and $\mu\varepsilon\rho o\varsigma$-meros = part. It nicely describes the characteristics of polymers: Many macromolecules (monomers) are arranged in a multiple repeating order to form an extended structure - the polymer [59]. Polymers have been useful for solubilizing nanotubes [60]. The polymer backbone wraps around the nanotube and additional side chains promote the solubilization in the solvent. Polymers are beneficial compared to surfactants and π-π-stacking as they wrap tightly around the SWNTs in a uniform way, which even endures filtration processes [61]. Nish *et al.* used different aromatic organic polymers and demonstrated selectivity towards diameter and chirality. Slight changes in the backbone structure or side chains of the polymer showed high sensitivity towards tube selectivity [60].

A prominent adoption of polymer wrapped SWNTs is their incorporation into polymer matrices to improve the mechanical properties of the matrices [62]. Polymer wrapped SWNTs were implemented for biomedical application, *e.g.* drug delivery, bioimaging, and tissue engineering. Furthermore, by modifying the monomer fragments, different functionalities can be added, making them promising candidates for photovoltaic applications and the use as sensors [63]. In Chapter 6 the functionalization of SWNTs with a perylene based polymer will be investigated, highlighting its use for bioimaging applications.

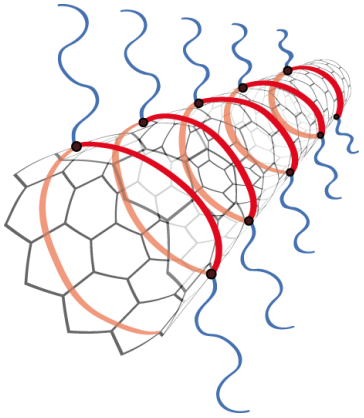

Fig. 3.5: Polymer uniformly wrapping around a carbon nanotube.

The non-covalent functionalization routines discussed so far are crucial for the immobilization of functional moieties on the SWNTs. All of them have well established protocols to ensure a close interaction between SWNTs and the functionality. They are non-perturbing, leaving the sp^2 and π-conjugation of the SWNTs untouched. The main drawback of non-covalent attachments is their sensitivity towards changes in the environment. Slight changes can lead to rebundeling of the tubes and loss of the functionality. The "gentle" nature of the covalent functionalization causes the major drawback, their instability. Covalent functionalization, on the other hand, secures a firm attachment of the functional groups onto the SWNTs surface. This procedure, however, compromise the optical properties of the SWNTs, as highlighted in the next section.

3.3 Covalent Functionalization

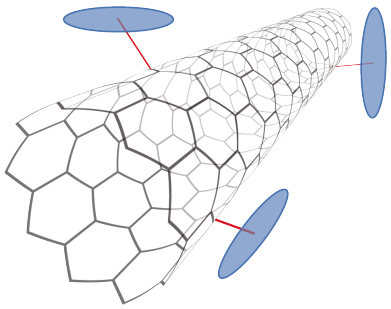

Fig. 3.6: Functional moieties covalently attached to the nanotubes sidewalls.

Covalent functionalization is based on harsh chemical treatment; thus it ensures a stable attachment of the functionality but results in the conversion of sp^2 into sp^3 carbon, disrupting the conjugated π-system. Hence it is not favourable for the optical implementation of SWNTs [64]. Covalent functionalization can be established on the defects already present in the skeletal network of the SWNTs or by creating additional defects through varying techniques *e.g.* carboxylation, thiolation, and amidation. For an elaborate review of the functionalization, especially on the chemical background please refer to Ref. [32] and [65]. Covalent functionalization ensures a stable attachment of the functional moiety, however, it compromises the optical and electronical properties of the tubes. Already mild carboxylation showed to tremendously destroy the optical

properties of SWNTs [66].
Covalent functionalization so far has mainly been used for application which do not exploit the outstanding optical properties of SWNTs. It helped increasing the wetting behaviour of SWNTs, making it possible to incorporate them into polymer and metal matrices for *e.g.* heat sink applications [67], [1]. Covalent functionalization has also been promising for biomedical applications, such as DNA sensors, biochemical sensors, and biomarkers [68]. Fluorescein for example, was attached onto the SWNTs sidewalls through carboxylation to mark leukaemia and T cells after cellular uptake[69].

In this chapter, I introduced the different approaches for chemical modification of SWNTs. The endohedral functionalization introduces small components into the interior of the tubes. This approach strongly limits the size of the inserted molecule. Another class of chemical alteration is the non-covalent functionalization. Different approaches were classified as such they all share a functionalization on the SWNTs sidewall without disturbing the π-conjugation of the electronic SWNT system. Such mild approaches are promising for tailoring the optical properties through functional moieties. The drawback of this approach is the sensitivity towards external changes. Slight changes in the environment can lead to the disruption of the functionalization. Covalent functionalization benefits from the strong attachment of the functional moiety on the SWNTs sidewall, but at the cost of disrupting the optoelectronic properties of the tubes. Up to now the covalent functionalization is dogmatically associated with loss of the optical properties of SWNTs. We developed a way to overcome this obstacle and functionalize SWNTs covalently without comprising the sp^2 network of SWNTs via a [2+1] cycloaddition reaction. I will present those results in the next Chapter.

4 [2+1] Cycloaddition

In the previous chapter different functionalization approaches for SWNTs were introduced. For optical application, non-covalent functionalization is favoured, as it preserves the intrinsic optical properties of SWNTs. The drawback is their instability, especially with respect to changes in the environment. Covalent functionalization, on the other hand, is condemned to quench the emission of the SWNTs, impeding the use of covalent functionalized tubes for optoelectronic applications. In this chapter I will introduce a novel covalent functionalization routine we developed which does not comprise the sp^2 network of the SwNTs - the [2+1] cycloaddition reaction.

4.1 The Covalent Functionalization versus Luminescence Dichotomy

Covalent attachment of functional moieties induces defects in the SWNTs skeletal network and thus degrades the optical properties of the SWNTs. In Ref. [66], we showed that already mild covalent functionalization, in this case carboxylation, destroys the optical properties of the SWNT. The SWNTs were briefly exposed (15 min) to standard acid treatment [70], resulting in covalently attached COOH groups on the tubes sidewalls. The short exposure to the acid converted some sp^2 into sp^3 bonds, disrupting the π-network. We analysed the changes of the optical response after chemical functionalization and observed an overall decrease in the emission intensity of the tubes. I performed PLE mapping and observed the vanishing of the emission of certain chiralities. Figure 4.1 b) shows the PLE map of the tubes before and after acid treatment. Most of tubes loose their emissive behaviour due to the induced defects. The acid treatment leads to a protonation of the SWNTs sidewall, injecting holes into the π-system near the reaction site. In Section 2.5.1 we introduced the concept of diameter dependent reactivity, which can be nicely observed for this covalent functionalization approach. The tubes with larger diameter (namely the (10,2) and (9,4) tubes) are more resistant towards the acid treatment and can be still observed. Nearly all tubes with a small diameter vanish after functionalization. Only a tiny fraction of the (6,5) with small diameter remain observable as this is the most abundant tube in the SWNT batch.

This behaviour is also reflected in the absorption measurements. Figure 4.1 d) shows that the S_{11} and S_{22} absorption bands of small diameter tubes (short wavelengths highlighted in yellow) disappear after the treatment. Raman measurements as well show the disruption of the sp^2

hybridized carbon. The functionalized tubes show a dramatic increase of the D peak compared to the pristine tubes (see Fig. 4.1) which indicates formation of defects in theπ-network. The D to G ratio increases from 0.02 to 0.63, indicating the loss of sp^2 carbon in the tubes after carboxylation, further explaining the quenching of the tubes emission.

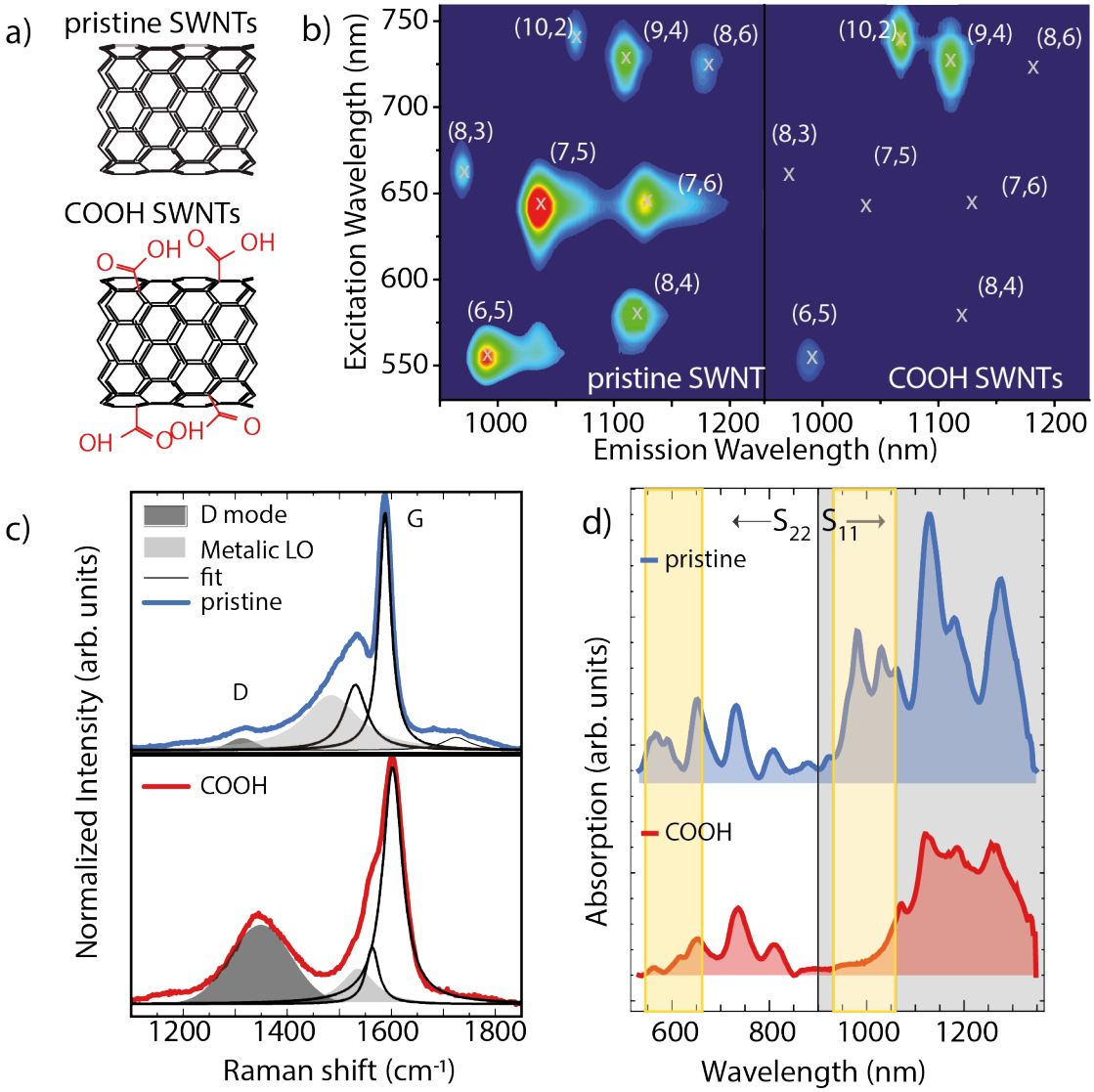

Fig. 4.1: a) Sketch of the pristine and carboxylated SWNTs. b) PLE maps: the left one shows the bright emission of the pristine tubes, whereas the functionalized nanotubes exhibit strong quenching of the emission. c) Raman spectra of the carboxylated and pristine tubes excited at 2.33 eV. The comparison shows a distinct increase in the D band for the functionalized batch indicating the induced defects. d) Absorption spectra of the unfunctionalized and the functionalized SWNTs. The peaks show the transition energies of the SWNTs and clearly indicate a loss of the smaller diameter tubes. Adapted from Ref. [66]

The results of Fig. 4.1 are in agreement with other observations in literature. Cognet *et al.* performed a study that directly showed the effect of defect sites on the SWNTs emission [64]. They performed single molecule chemical reactions (reversible and irreversible) to convert single carbon atoms from sp^2 to sp^3 hybridization and observed the photoluminescence with a NIR-photoluminescence microscope. The experiments showed that the defect sites, where the reaction took place, lead to quenching of the emission. This finding is explained by the

interaction of the electron with the cavity induced in the π-system. The exciton will non-radiatively recombine at those sites.
So far there is only one covalent functionalization scheme that showed brightening of the nanotubes photoluminescence: The aryl -based functionalization [71]. This functionalization locally converts an sp^2 carbon atom into the sp^3 form by attaching an aryl-ring without creating a dangling bond or inserting structural defects into the tubes. After the covalent attachment of aryl groups the conversion of sp^2 to sp^3 triggered the activation of dark excitons, enabling strong luminescence at the expense the loss of their one dimensionality [71]. The aryl functionalization induced an alteration from one dimensional, delocalized excitons to zero dimension localized emission [72]. Such single photon sources operating at room temperature and in the telecom range are the building block for new technologies, such as sub-diffraction imaging, quantum key distribution, and photonic quantum information processing. Despite this specific example is the general believe that covalent functionalization always destroys the optical properties of SWNTs.

4.2 Cycloaddition Reactions

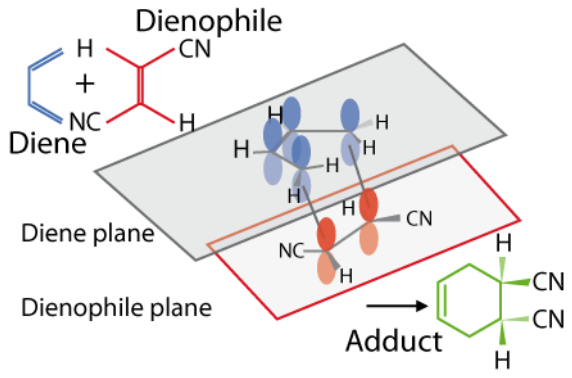

Fig. 4.2: Illustration of the Diels-Alder reaction between diene and dienophile visualizing the product of a cyclic reaction. Adapted from Ref. [73].

The quenching and disturbance of the opto-electronical properties of SWNTs are a major drawback for the covalent functionalization routine. Theoretical predictions, however, introduced the idea of overcoming this limitation with a novel covalent attachment via cycloaddition reactions [74]. A cycloaddition is a pericyclic chemical reaction, involving at least two unsaturated systems that form a cyclic adduct. The specific cycloaddition is defined by the number of π-electrons participating in the reaction. [p+q] cycloaddition refers to the implementation of p π-electrons of the first molecule and q π-electrons of the latter. Figure 4.2 depicts a [4+2] cyclo addition also referred to as Diels-Alder reaction. Here the diene with four π-electrons reacts with the dienophile forming the cyclic adduct. The advantage of some cycloaddition reaction is the use of the π-bonds instead of the σ-bonds for attachment, potentially leaving the sp^2 hybridization unperturbed. This, however, is not automatically granted for all cycloadditions. Several experimental approaches have been pursued showing successful attachment of moieties on the SWNTs sidewall. However, none of them could validate the theoretical assumption made in preserving π-conjugation of SWNTs. For a review on this topic please refer to Ref. [75].
Marzari and co-workers theoretically investigated the [2+1] cycloaddition reaction of carbene to SWNTs and predicted it to preserve the transport characteristics of SWNTs. They concluded

that this approach could be a valid candidate for covalent functionalization with preserved optoelectronic properties [74]. By applying density functional theory (DFT), they moreover investigated the addition of nitrene and carbene groups on the SWNTs sidewall. The added groups saturate the double bond between two carbon atoms resulting in a cyclopropane-like three membered ring.

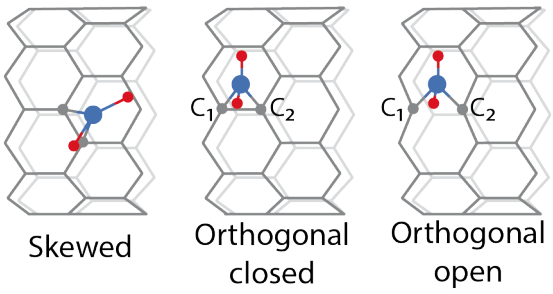

Fig. 4.3: Different functionalization configurations of a molecular moiety on the SWNTs sidewall: The skewed, orthogonal closed and orthogonal open configuration. Adapted from Ref. [74].

The reaction can proceed on two different sites, the skewed and the orthogonal position. Their findings showed that the tubes favour the orthogonal configuration. Furthermore, the relaxed position showed a larger than expected C_1-C_6 distance indicating a broken bond. Thus, two configurations are possible in the orthogonal case - a closed and an open configuration. In the closed form the two carbon atoms bridge the added functional group through an sp^3 state. The open configuration is more favoured in SWNTs with respect to flat graphene due to their curvature. Here the carbon-carbon bond below the functionality is released, restoring the sp^2 configuration and thus preserving the π-configuration. Marzari and co workers argued that the orthogonal configuration, when undergoing bond cleavage, maintains the conductance properties of SWNTs [74].
A first experimental confirmation of the benefits of cycloaddition was reported by Liu *et al.* [76]. Through a [2+1] cycloaddition they attached dichlorocarbene on the SWNTs sidewalls. The attachment preserved the electrical conductance of the metallic SWNTs but converted the semimetallic into metallic ones. They revealed that the metallic SWNTs kept the sp^2 configuration through bridge opening. The sp^2 configuration of the s-SWNTs, however, converted into a sp^3 hybridization during the functionalization step. While the preservation of the π-conjugation of the carbon network in the metallic tubes hints towards the conservation of the optical properties of SWNTs. The conversion of the semiconducting into metallic tubes hindered any analysis of the functionalization outcome on the optical response of the tubes. Several experimental groups tried to implement the theoretical predictions, but, as mentioned before, they could not preserve the optoelectronic properties of SWNTs.

We proposed a way to establish a [2+1] cycloaddition reaction that matched the theoretical predictions [8]. For the first time, we could report on the preservation of the optoelectronic properties of covalently functionalized carbon nanotubes[1]. Differently to prior approaches, we used an aromatic nitrene derivate for the [2+1] cycloaddition. The azidodichloro-triazine

[1]The following part of the chapter are based on our publication in Nature Communications 8, 14281 (2017). The publication was a joint interdisciplinary project within the SFB 658 funded by the DFG. I contributed to this work by preparing the SWNT sample for optical characterization, performed and evaluated the optical characterisation of the samples and contributed to the experiments design. The contributions of the collaboration partners are highlighted in the corresponding sections.

attaches via the nitrene onto the SWNTs, as sketched in Figure 4.4. The created adduct exhibits strong strain at the functionalization site. The C-C bond below the triazine breaks and the electron lone pair of the binding nitrogen restores the sp^2 configuration of the SWNTs, while integrating the triazine into the π-conjugated system. In a single functionalization step both the ring opening and rehybridization take place, creating a fully conjugated hetero-bridged nanotube[2], please refer to the SI of Ref. [8] for a detailed description of the compounds synthesis. This assumption was confirmed by quantum chemical calculation[3], as reported in Fig. 4.4 b). In the following sections I will describe the chemical and physical characterization of the new compound and provide an insight into the universal and promising implementation of the new functionalization routine.

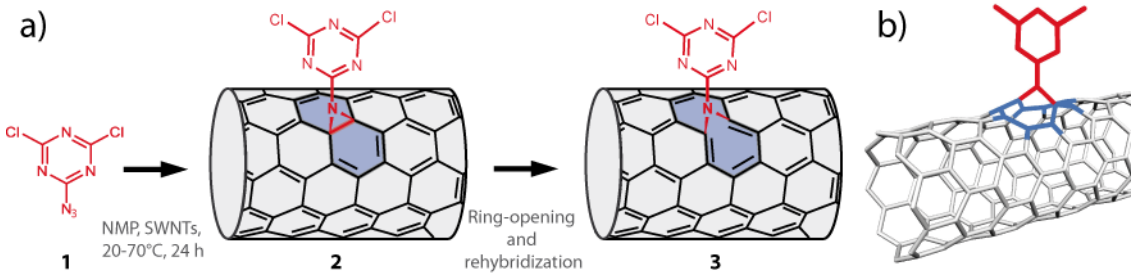

Fig. 4.4: a) Functionalization scheme of the [2+1] cycloaddition reaction on SWNTs. b) Quantum theoretical calculation proving the ring opening configuration of SWNTs under the triazine moiety.

4.3 Characterization

Different independent characterization methods were needed in order to fully proof the successful covalent attachment of the triazine according to our expected configuration. Triazine covalently attached onto the tubes as sketched in Fig. 4.4 is only one of the possible reaction outcomes between the tubes and the triazine-derivative. The triazine could also stack non-covalently on the SWNTs sidewalls or build a supra molecular assembly around the tubes, to name some of the possible reaction products. To ensure the covalent functionalization we preformed thermogravimetric analysis (TGA), X-ray photo electron spectroscopy (XPS) and high resolution transmission electron microscopy (HRTEM)/ electron energy loss spectroscopy (EELS) measurements. At the end of this chapter the optical properties of the samples will be investigated in order to verify the undisturbed π-configuration.

4.3.1 HRTEM

Transmission electron spectroscopy (HRTEM) was used to investigate the morphological, compositional, and crystallographic formation of a material. Electron microscopy uses electron

[2]Mohsen Adeli synthesized the functionalized SWNTs.
[3]Frederica Maschietto and Beate Paulus performed quantum chemical calculations.

beams instead of light, increasing the resolution of the measurement. The electron passes through a preferably thin sample. The image is formed from the interaction of the electrons with the sample as the beam is transmitted through the specimen. High resolution TEM additionally detects the scattered and transmitted electron, leading to a higher resolution of the imaging. The resulting image is an interference pattern between the forward-scattered and diffracted electron waves from the specimen. An image is formed from the interaction of the electrons with the sample as the beam is transmitted through the specimen. The observed structure can be as small as a crystal unit cell which is valuable in analysing small structures. Such as the attachment of the triazine onto the SWNTs sidewall. In the HRTEM image we observe a small bundle of tubes with molecular moieties attached to its sidewall. This area is depicted in the high angle annular dark field image in Figure 4.5. In order to analyse the nature of those moieties, to ensure the presence of triazene, energy loss spectroscopy (EELS) on different spots of the sample was performed[4].

4.3.2 EELS

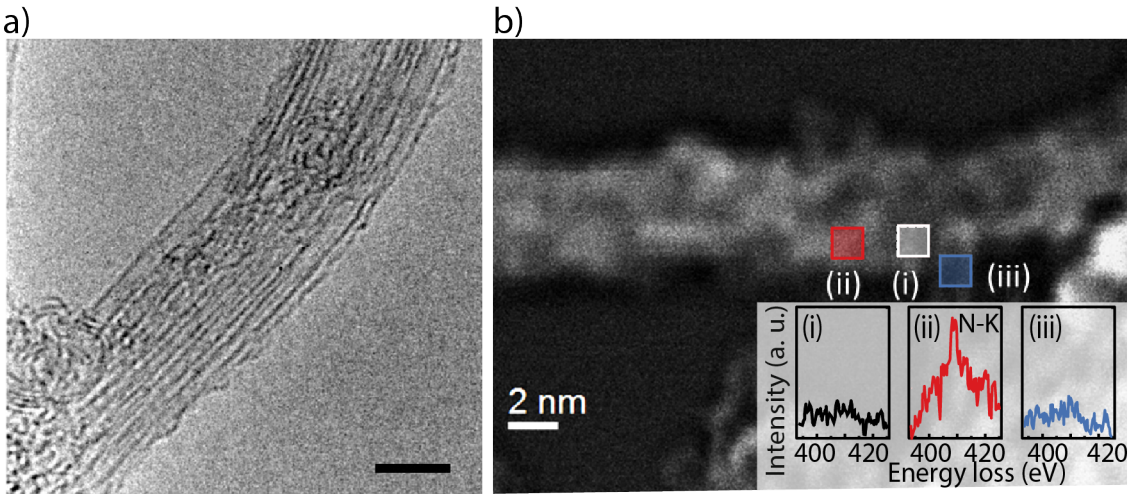

Fig. 4.5: a) High resolution image of the functionalized SWNTs bundle. b) EELS measurements were performed on three (i-iii) different spots on the nanotube as seen on the HRTEM image. In ii) the N-K edge can be observed indicating the presence of the triazine.

During EELS the SWNTs are exposed to an electron beam with a narrow range of kinetic energies. The electrons undergo inelastic scattering at the material, causing a loss in energy of the detected electrons. This loss originates from phonon excitation, inter and intra band transitions, plasmon excitation, Cherenekov radiation, and inner shell ionization. The latter one helps identifying the composition of the investigated material [77]. The loss in energy can be directly linked to the energy needed to remove an inner electron from a certain atom, e.g. an energy decrease by 285 eV indicates that the material comprises carbon. Thus the EEL spectra reveals the composition of the material. Here we wanted to proof the attachment of triazine on the tubes sidewalls and observed the N-K edge around 400-420 eV. EELS measurements

[4]The HRTEM measurements were performed by Raul Arenal.

were performed on three different spots as depicted in Fig. 4.5. The inset on the lower right corner shows the EELS of different spots. Two spots were chosen with bare SWNTs sidewalls (Fig. 4.5 white and blue square, respectively i and iii) and one with the molecular moieties on the SWNTs sidewalls (red square). The EELS measurement of the second spot (Fig. 4.5ii) red square) exhibits a N-K edge indicating the presence of nitrogen. The spots of the bare SWNTs sidewall did not reveal a N-K edge. As there is no other source of nitrogen in the samples this proves that the moieties observed in the HRTEM images are triazene localized on the SWNTS sidewalls[5].

4.3.3 TGA

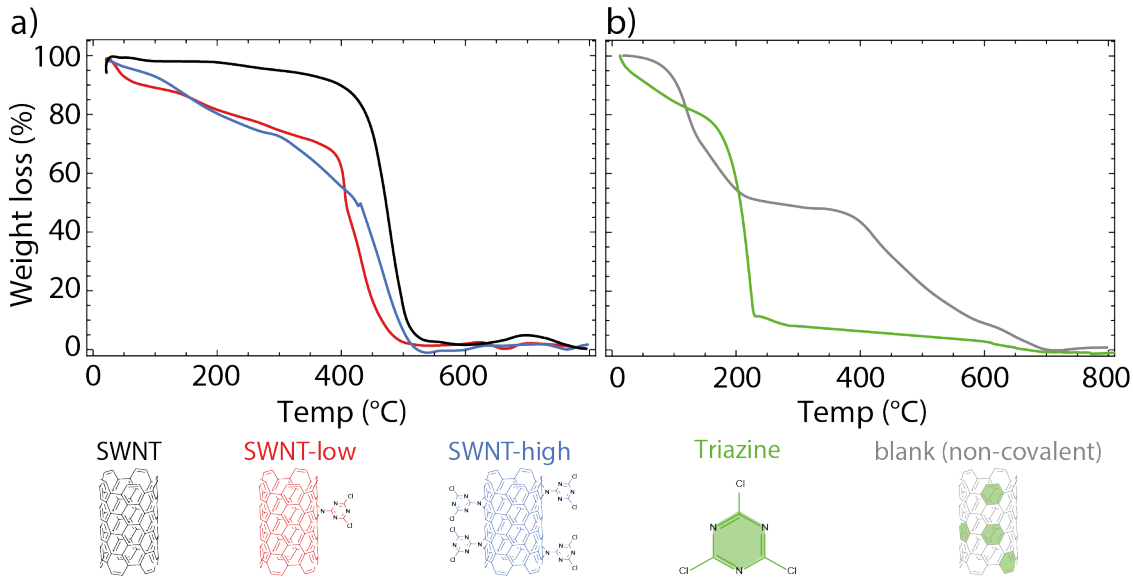

Fig. 4.6: TGA spectra of the a) pristine, high and low SWNTs and the triazine compound as well as for SWNTS with b) non-covalently attached triazine.

Thermogravimetric analysis is a tool used for material characterization. TGA provides information about second order phase transitions related to weight, such as sublimation, adsorption, desorption and vaporization. Additionally, it can also provide chemical information such as the chemisorption, decomposition, and desolvation. During a TGA process, the substance is placed on a microbalance and gradually heated up. The changes in weight are monitored, revealing information about the composition of the material. To further characterize the functionalized samples, we investigated five samples: Pure SWNTs labelled as SWNTs, Fig.4.6 a), triazine functionalized tubes with low (SWNT-low, Fig.4.6 b) and high (SWNT-high, Fig.4.6 c) density of functional groups, pure azidodichlorine (Fig.4.6 d) and SWNTs coated with the triazine derivative physisorbed onto its surface and not covalently attached (Fig.4.6 e)
The pristine tubes are stable up to 400°C and do not decompose until 450°C, where a steep drop in weight can be observed followed by a complete combustion at 500°C. The low and high functionalized tubes (respectively Fig.4.6b and Fig.4.6 c) show a faster decomposition rate up

[5]The EELS studies were performed and evaluated by Raul Arenal.

to 450°C compared to the pristine tubes, indicating the decomposition of the triazine. Similarly to the pure tubes, they fully decompose at around 500°C. The triazene undergoes a steady decrease of the mass up to 200°C followed by a steep jump, indicating the loss of most of the materials at 350°C, where it decomposes resulting in a full loss of the material (Fig.4.6 d). The blank sample (tubes with triazine physiosorbed on their sidewalls Fig. 4.6 e) was burned as well, revealing a markedly different decomposition pattern compared to the covalently functionalized SWNTs. Up to 200°C the sample exhibits a steeper decrease compared to its covalent correspondents. The slope is comparable with the one of the triazine and might be an indication of the loss of the triazine. Between 200°C and 400°C a plateau is reached followed by gradual decomposition until 700°C. The two distinct onsets indicate the decomposition of the separate components - the triazine and the SWNTs. The samples decomposition behaviour clearly differs from the pristine tubes and the non-covalent functionalized tubes, providing the first indication of the successful covalent functionalization[6].

4.3.4 XPS

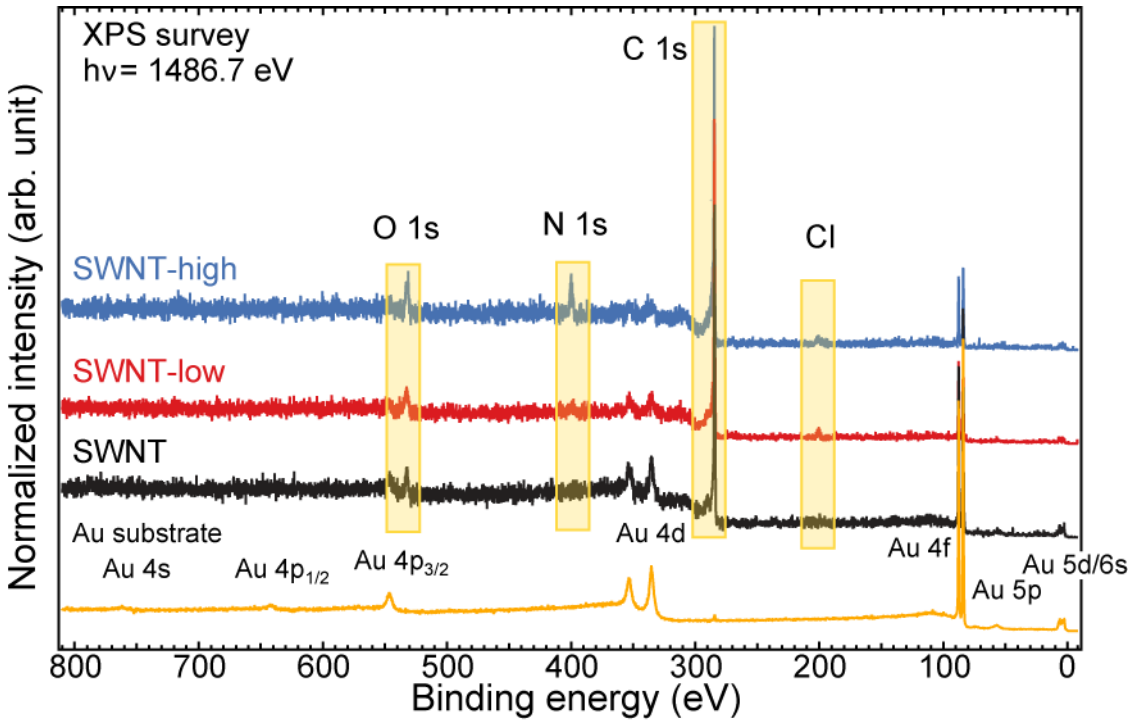

Fig. 4.7: XPS overview of the pristine, high and low nanotube samples and the gold substrate as a reference. The measurement reveals the presence of oxygen, nitrogen, carbon and chlorine.

X-ray photoelectron spectroscopy is a non-destructive, surface sensitive method for analysing the elemental composition of a material and the nature of the chemical bonds between the components. Monochrome photons are used to detach electrons from the investigated sample. In a typical XPS spectra the number of electrons are given versus the binding energy of the exposed electrons. Each element has a characteristic set of peaks at specific binding energies.

[6]The TGA measurements were conducted and evaluated by Mohsen Adeli.

Those peaks identify the elements present at the surface. The different spectral positions represent the electron configuration within the atoms. The spectra can be further used to estimate the amount of the elements present in the sample. Here we want to use XPS to identify the elements and electron configuration of our samples and to attain the degree of functionalization.

In the XPS measurements we compared the pure SWNTs with the high and low functionalized samples. Figure 4.7 displays the complete XPS spectra of the samples. A strong band around 284 eV arising from the main element of SWNTs - carbon, can be observed in all three SWNT samples. The second strongest signal arises from the gold substrate located between 80 and 90 eV. A smaller peak is located around 532 eV indicating the presence of oxygen, due to oxidation of some defects sites. In the high and low functionalized samples additional peaks could be monitored: Around 400 eV a band corresponding to nitrogen could be observed, while the peak around 201 eV indicates the presence of chlorine. Those features are not present in the pure SWNT samples and clearly indicate the presence of triazine in the functionalized sample. The first rough comparison of the samples already indicates the successful functionalization. By analysing the individual peaks in more detail we could confirm the functionalization. Figure 4.8 (lower panel) displays the C1s XP spectra of the pure SWNT. The peak is mainly positioned at 284 eV and shows a side band up to 292 eV indicating different carbon species. For a full classification of the individual bands please refer to the SI of our corresponding publication [8].

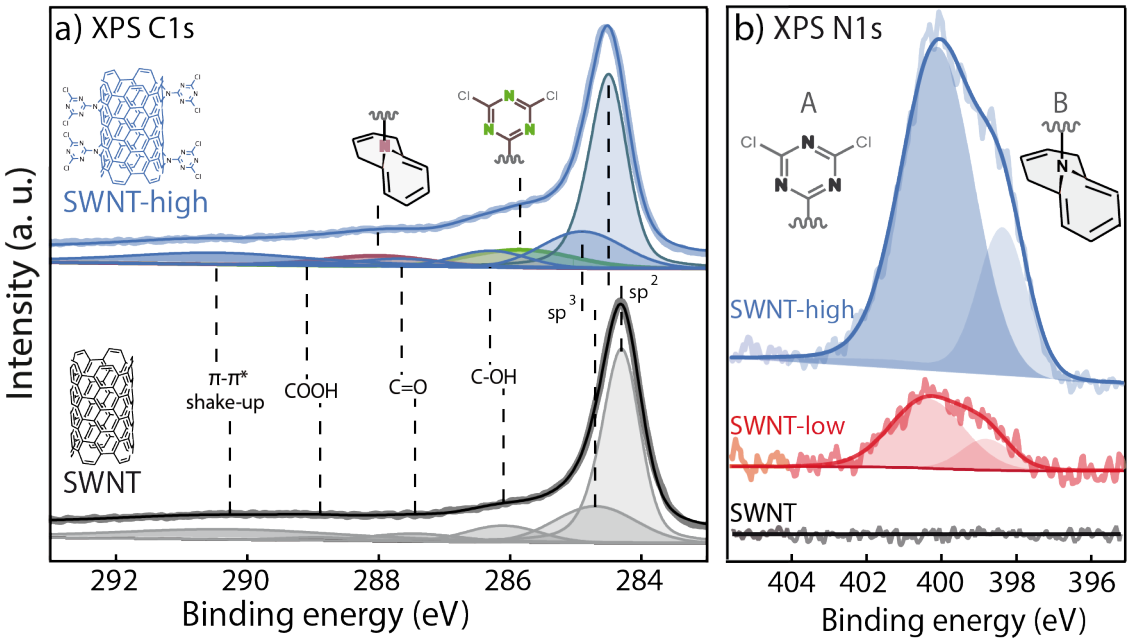

Fig. 4.8: a) XPS C1s spectra of the high functionalized and pristine tubes showing the presence of carbon in the sample. The two additional peaks in the triazine sample indicate the successful binding of the triazine. b) N1s XPS spectra indicates the presence of nitrogen. The increase of nitrogen in the high sample compared to the low samples proofs the higher functionalization of the tubes.

The noteworthy feature are the additional bands in the spectra of the high functionalized tubes (Fig. 4.8a upper panel), namely a peak at 285.84 eV and one at 288.01 eV. Those peaks are a clear indication for the successful covalent functionalization of the tubes. The peak at 285.84 eV corresponds to the three carbon atoms in the triazine component and to the peak positioned at 288.01 eV resembles the carbon atoms which are bridging to the nitrogen atom of the triazine. The presence of the two additional peaks confirms the covalent functionalization of the tubes with the triazine moieties. Figure 4.8 b) displays the XPS N1s spectra of the three investigated samples. For the pure SWNTs no features were observed in the range around 400 eV as expected. The two functionalized samples show distinct peaks at 400 eV, sheating two peaks: Peak A originates from the nitrogen in the triazine ring and peak B is associated with nitrogen bridging to the nanotube. The presence of the additional peaks clearly indicates the successful functionalization. Furthermore, by taking the peaks areas of the XPS spectra into account we can quantify the overall amount of functional groups. A detailed evaluation of the XPS data is given in the supporting information of Ref. [8]. Here the end results are summarized giving a quantification of the functionalization (see Tab. 4.1). The XPS measurements showed a coverage of one triazine molecule per 104 and 24 carbon atoms, respectively for the low and high functionalized samples. XPS helped to confirm and quantify the covalent functionalization.

Sample	pristine	low	high
DFG	0	1/104	1/24

Tab. 4.1: Summary of the density of functional groups per carbon atom for the different triazine coverage.

The presence of the nitrogen and chlorine peak in the functionalized tubes strongly indicate the successful functionalization. The close up of the carbon and nitrogen spectra confirm the assumption on the bridging of the nitrogen of the triazine onto the carbon nanotubes[7].

4.3.5 Raman

Another way to prove the undisturbing nature of the functionalization routine is obtained through Raman spectroscopy. The spectroscopic technique detects vibrational, rotational, and other low-frequency modes in a system, identifying the structural fingerprint and electronic state of a molecule. A detailed description of the Raman processes in SWNTs is given in Ref. [18].

[7] Daniel Przyrembel and Martin Weinelt performed the X-ray photoelectron spectroscopy analysis.

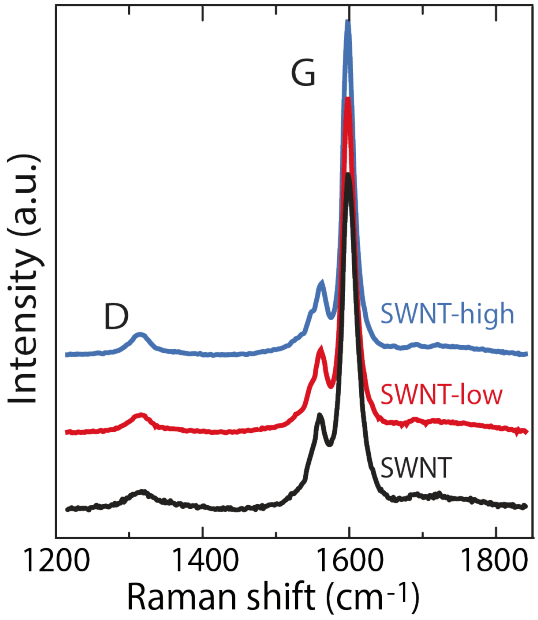

Fig. 4.9: The Raman spectra of the samples do not show any changes with higher degrees of functionalization.

For SWNTs, mainly the D and G peak are of interest as well as the radial breathing modes (RBM). The RBM is unique for each chirality as it scales with the diameter. It provides direct proof of the SWNTs existence in a sample and verifies the present chirality composition. The G band originates from the stretching of the C-C bonds in sp^2 materials. The D band on the other hand arises from disorders in the sp^2 network, thus is sensitive to defects in the carbon network. In the beginning of this chapter, we showed that already mild covalent functionalization lead to a strong increase in D Mode (see Fig. 4.1). A change in D to G ratio always indicates structural defects in the nanotubes. Figure 4.9 shows the Raman spectra of the pristine, low, and high functionalized tubes. The samples show a nearly constant D to G intensity ratio and no change in the D bands, indicating that no additional defects were induced and the π-conjugation is preserved by the covalent functionalization[8].

4.3.6 Optical Characterization

In the previous sections we provided evidence for the successful covalent functionalization of the SWNTs. To prove the non-destructive nature of the [2+1] cyclo addition functionalization, I investigated the emission ability of the samples, as it provides the most straightforward proof about their structural integrity and the preservation of their quantum optoelectronic properties. Figure 4.10 displays a 2D excitation map of SWNTs with three different degrees of functionalization. Figure 4.10 a) displays the pristine SWNTs, showing the distinctive peaks corresponding to the different chiralities. In Fig. 4.10 b) and c) we can observe the emission from the functionalized tubes. The triazine functionalized SWNTs show bright emission, proving to remain the undisturbed π-network even after covalent treatment. Showing emission in highly covalently functionalized tubes is a milestone in the nanotube community. Up to now the dogma was established that covalent functionalization always quenches the emission of nanotubes. On the contrary, our study has shown that the emission of some tubes are even enhanced. The *laola* family of the 23 tubes, e.g. hardly emits in pristine tubes after the functionalization their luminescence is significantly increased. Figure 4.10 d) displays a pseudo PLE map and depicts the intensity of the individual chiralities. The radius of each circle is proportional to the intensity of the tubes. One can observe that with bigger tube diameter the intensity of the tubes increases, where as the intensity of small diameter tubes is reduced.

[8]Georgy Gordeev and Stephanie Reich performed the Raman characterization of the metallic SWNTs.

This phenomena is highlighted in Fig. 4.10 e) comparing the change in intensity versus the tubes diameter. SWNTs with diameters bigger than 0.85 nm show an increase in intensity between 100% to nearly 300%. The smaller diameter tubes (<0.85 nm) decrease up to 70%. Absorption spectroscopy (Fig. 4.10 f) confirmed that the composition of the samples did not change after functionalization, ruling out that the decrease of the emission intensity is due to nanotube loss.

The diameter dependency hints towards a selectivity of the functionalization routine due to the curvature of the tubes. The functionalization routine strongly modifies the small diameter tubes with higher curvature and higher reactivity. Conventionally, one could expect that the functionalization induces more defects in those tubes and consequent quenching of the emission. The stable D to G intensity ratio of the Raman measurements, however, disproves this assumption. Another explanation could be that the changes in luminescence are connected to the changes in chemical potential due to the functionalization. Smaller tubes due to the expected higher reactivity might experience a higher functionalization and such a bigger change in chemical potential, lowering the overall emission yield. To understand the intensity decrease of the small tubes with respect to the bigger diameter tubes further investigation needs to be conducted. For example, standard separation techniques could be applied to the functionalized tubes in order to investigate the functionalization effect on the single chiralities.

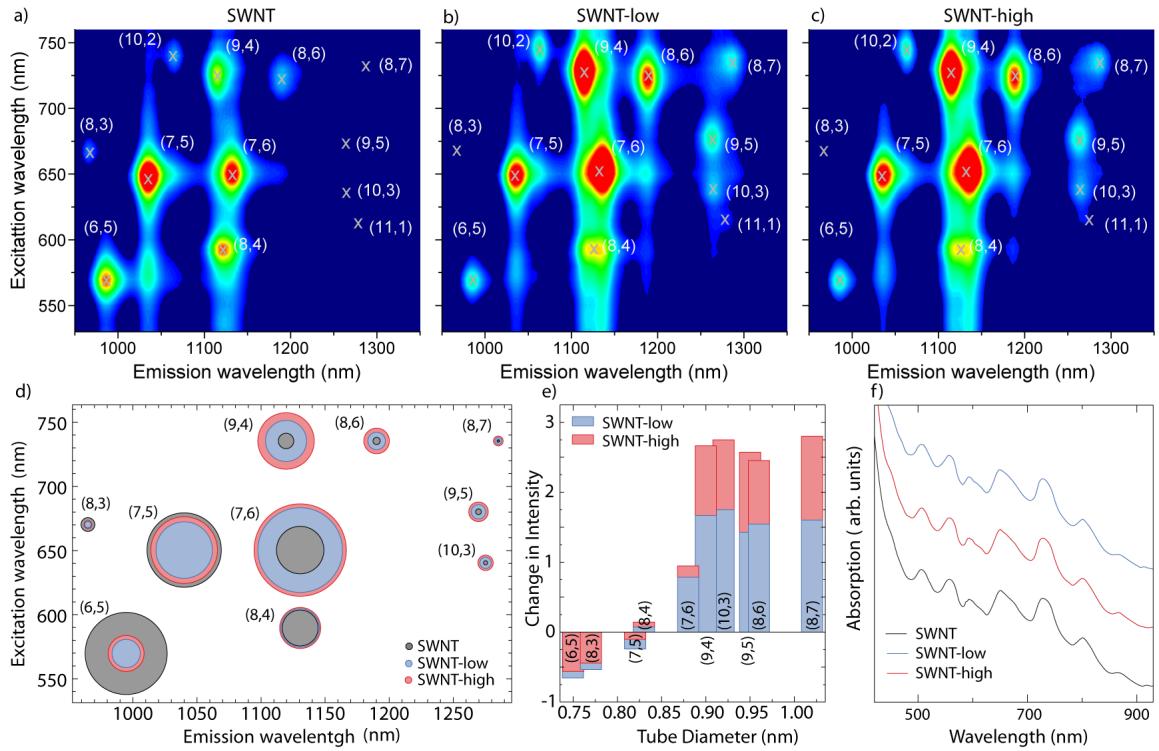

Fig. 4.10: 2D excitation maps of the a) pristine SWNTs, b) SWNT-low, and c) SWNT-high samples. d) Pseudo PLE map comparing the different samples to highlight the changes in intensity. e) Change of the tubes intensities versus the tube diameter. f) Absorption spectra of the SWNT samples.

4.4 Influence on the SWNTs Properties

The successful covalent immobilization of triazine onto the SWNTs sidewalls profoundly influences the intrinsic properties of the SWNTs themselves. The nitrogen bridging the triazine onto the nanotubes' sidewall is now an integrated part of the conjugated sp^2 network and its lone electron pair increases the overall chemical potential of the tubes. XPS and Raman measurements showed changes in the Fermi energy supporting this doping-by-functionalization picture. The XPS C1s spectra in Figure 4.11 revealed a shift of the position of the sp^2 carbon peak. The shift towards higher binding energies can be clearly observed in all the samples see Fig. 4.11. The higher the degree of functionalization the bigger the shift. Their peaks analysis revealed a shift of the Fermi energy of 119 meV and 202 meV, respectively, for the low and high functionalized sample. The shifts also provide a further confirmation of the successful covalent attachment. If the triazine would only interact non-covalently with the nanotubes a shift in the opposite direction towards lower binding energies would be observed, as reported by Cervenka *et al.*[78]. The shift to higher binding energies can occur only if the N atom is covalently integrated into the carbon network. An opposite trend can be observed in the nitrogen spectra. The binding energy corresponding to the bridging nitrogen shifts to lower binding energies. This confirms that the lone pair of the attached nitrogen contributes to the π-conjugation of the SWNTs. Changes in the Fermi energy can also be monitored by Raman spectroscopy. The

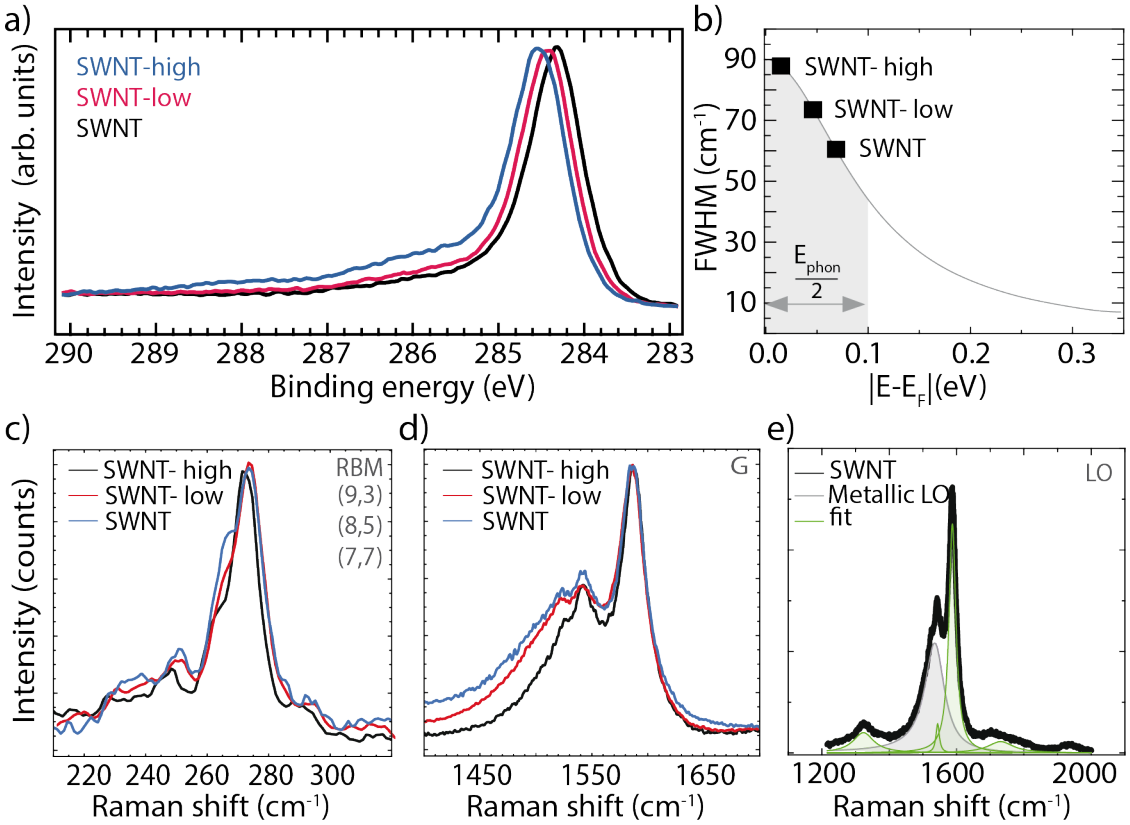

Fig. 4.11: a) XPS C1s spectra of all samples indicating the shift of the carbon sp^2 peak. b) Broadening of the G band fit in respect to the Fermi level. Raman spectra of the c) RBM and d) the G band. e) Fitting of the G band (green) and the metallic LO (grey)

G band of metallic tubes is split into two peaks named G^+ and G^-. The former is located at 1580 cm^{-1} and is associated with the transversal optical phonon. The latter is connected to longitudinal optical (LO) phonon and responsive towards changes of the Fermi energy. A shift in the Fermi level, crossing of valence and conduction band, continuously increases the LO phonon lifetime and decreases the full width at half maximum (FWHM) of the LO peak.
We resonantly excited the tubes at 532 nm and investigated the G peak as well as the radial breathing modes to monitor changes in the Fermi level. Fig. 4.11 displays the RBM, identifying the (9,3), (8,5) and (7,7) species, showing the same set of chiralities in all investigated samples. Fig. 4.11 displays the G peak with its splitting into the G^+ and G^- bands. The G^+ position remains constant in position and width, whereas the G^- broadens. The peak was fitted to a Lorentzian dispersion model and the shift in Fermi energy is ascertained through the model obtained in Ref. [79]. The position of the pristine tubes with respect to the high functionalized is shifted by approx. 6 cm^{-1}. The analysis of the G^- band suggests a doping level of -70 eV, -40 eV, and +20 eV, respectively for the pristine, low and high functionalized tubes. The values obtained for the shift in Fermi energy via Raman spectroscopy are smaller than the ones from the XPS results. The XPS measurements investigated all the nanotubes, where as the Raman measurement selectively investigated a limited number of small diameter tubes.
Those results show that, even if the covalent functionalization of the SWNTs does not disrupt their optoelectronic structure, it still strongly influences the instrinsic properties of the SWNTs by injecting additional charges to the nanotubes' delocalized π-system.

4.5 Exploiting the new Covalent Functionalization Routine

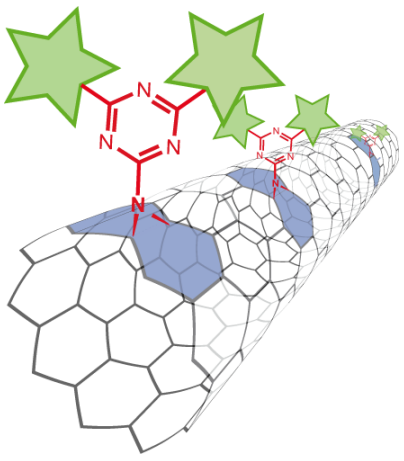

Fig. 4.12: Sketch of the triazine functionalized SWNTs highlighting the versatility of the new approach by attaching different functional moieties on the Cl atoms.

The attachment of functional moieties leads to impressive changes of the intrinsic characteristics of SWNTs, paving the way for technological applications. The potential alteration of the intrinsic properties of SWNTs through the interaction with functional moieties offers an endless range of applications from sensors to bio markers [7]. The field of optoelectronic manipulation of SWNTs has tremendous potential. With our new unperturbating covalent functionalization approach we showed that covalent functionalization does not always disrupt the optoelectronic propeties of SWNTs and therefore offers an approach for rigid attachment of functional moieties onto the SWNTs sidewalls.

In the remaining parts of this thesis the tailoring of the optical properties through different functional moieties will be investigated. The interaction of the following functionalities with the SWNTs will be examined:

1. Spiropyran, a molecular dipole switch:
   The decoration of spiropyran on the SWNTs is predicted to lead to reversible alteration of the tubes transition energies.

2. Perylene, an aromatic dye:
   Energy transfer between the dye and the SWNTs result in monochrome excitation of several SWNT chiralities.

3. Plasmonic metal nanoparticles:
   The strong electromagnetic field of the plasmonic nanoparticles leads to enhancement of the SWNTs luminescence.

To perform a critical, comparative investigation, I will first use well known and established non-covalent approaches for the immobilization of functional moieties on the SWNTs sidewalls. Next, I will compare them with the newly discovered non-perturbating [2+1] cycloaddition. The attached triazine offers a remarkable opportunity to attach other functional moieties onto the nanotubes via exchanging the chlorine atoms at the ends, creating a new toolbox for rigid immobilization of functionalities onto the SWNTs sidewalls. Here I will give a first insight into the potential of the new functionalization routine.

5 Molecular Switches

In this chapter I will show how to use molecular dipole switches to tailor the optical properties of carbon nanotubes. Molecular switches attached on SWNTs have remarkable potential as they reversible change the SWNTs properties without additional chemical modification. In this chapter, I will provide a short introduction on molecular switches, especially the dipole switch spiropyran, and their interaction with SWNTs. Afterwards, the micelle swelling technique will be exploited to experimentally investigate the effect on the optical properties of the SWNTs induced by the presence of the dipole switch and compare with the theoretical prediction. In the last part of this chapter I will focus on the covalent attachment of spiropyran through the [2+1] cycloaddition and how this influences the tubes properties. The results described in this chapter are based on the publication in Ref. [9] and [8].

5.1 Molecular Switches

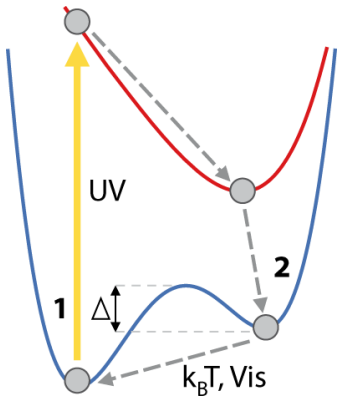

Fig. 5.1: Sketch of the potential landscape of molecular switches. Adapted from Ref. [17]

Molecular switches are molecular entites with two metastable configurations. They can be exploited for engineering sensors [80] and memory devices [81], [82]. Upon external stimuli such as light, temperature, or change in pH, they can convert between two states. Photochoromic switches react to light as stimuli. Upon light exposure with a certain wavelength, the molecule is excited from its global minimum to the first excited state from where it relaxes into a local minimum of the ground state, which corresponds to the second metastable form. This process is depicted in Fig. 5.1. In order to transform back into the initial configuration, the potential barrier Δ needs to be overcome either thermally or by absorption of photons. The isomerization process can induce changes of different nature in the switch, such as conformational or conjugational modification, or changes in the dipole moment. Conformational switches *e.g.* have been incorporated into surfactants and successfully solubilized and isolated SWNTs [83], [84]. Upon light exposure the micelle enclosing the SWNTs disrupts due to the conformational change of the switch, hence the tubes precipitated. This instance was irreversible for stilbene as the switching component and reversible for azobenzes. It can be

exploited to potentially deposit nanotubes in patterned way to create micro or even nanoscale system. Functionalization of carbon nanotubes with other kinds of molecular switches has been of great interest: The decoration of SWNTs with molecular switches enables to control the conductance in nanoscale electronics [85], is promising to build photoactive nanometer-sized mechanical switches in electronics [86], or can store energy in solar thermal fuels [87].

Here I concentrate on spiropyran, a molecule that can reversible alter the optical properties of SWNTs when attached onto its sidewalls. Spiropyran is a photochromic molecule consisting of a benzopyran and an indole moiety connected via a sp^3 hybridized carbon atom (Fig. 5.2 a). Spiropyran can be reversibly switched between the open merocyanine (MC) and the closed spiropyran (SP) conformation. During the isomerization process, driven by ultraviolet light, the spiro carbon-oxygen bond breaks, converting the spiro center to an sp^2 hybridized carbon atom. The new co-planar arrangement of the benzopyran and indole moieties in the merocyanine with the π-electron delocalized along the entire molecule generates an absorption band in the visible around 590 nm (see Fig. 5.2 b). The newly formed merocyanine is an extended π-conjugated system with a zwitterionic character. It is much more polar then the SP form, giving rise to a large dipole moment (14-18 D). For a detailed overview of the properties of spiropyran, please refer to Ref. [88].

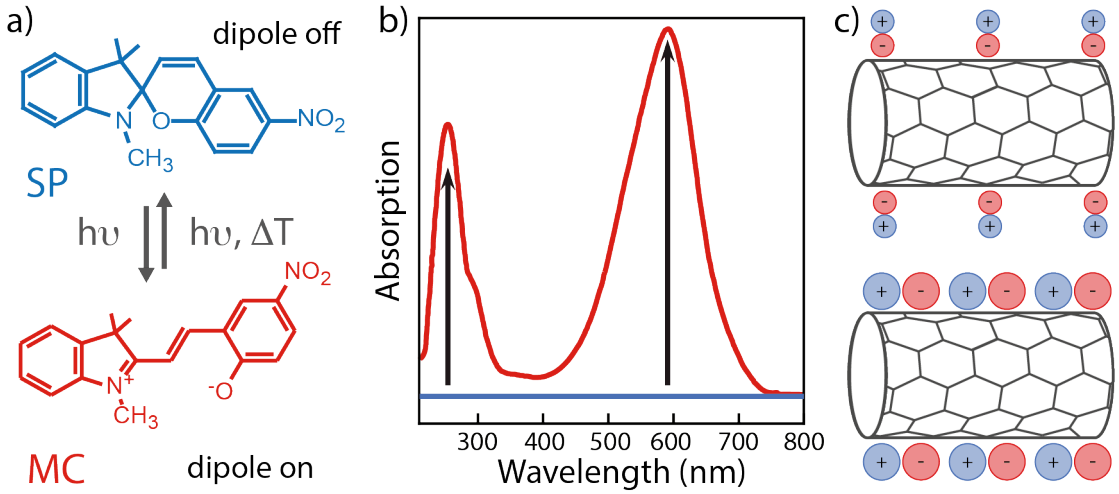

Fig. 5.2: a) Structure of the SP and MC. b) Absorption spectra of SP and MC. c) Dipole configuration in respect to the SWNT for SP and MC. Adapted from Ref. [17]

5.2 SWNT-Dipole Interaction

The change of dipole moment in the molecular dipole switches enables a way to reversibly and optically tune the direct electric surrounding of the tubes. The coupling of the molecular dipole moment with the excitons of the SWNTs is expected to strongly affect the optical properties of the SWNTs. Malic *et al.* predicted a shift of several meV in the exciton transition energies when undergoing the mero-spiro transition [89], [90]. Furthermore, they investigated different tube-

switch configurations and showed that the largest shifts are observed for a dipole orientation of 90° perpendicular to the tubes' axis and optimal switch coverage of 0.25 nm^{-1}. The Coulombic dipole-dipole interaction decreases with an increase in relative switch-tube distance; hence a close proximity is aimed to observe the strongest shift. The dipole distribution, on the other hand, has no measurable effect on the transition energies. At the same concentration, randomly and homogeneously distributed dipoles provide the same shifts in excitonic energies. Bluemmel *et al.* verified the theoretical predictions by Malic *et al.* and experimentally observed reversible shifts of the absorption bands of specially engineered SP-pyrene molecules which were non-covalently anchored onto the tubes via π-π-stacking [91], [54]. In these studies, the limiting factor to fully exploit the dipole-dipole interaction was the SWNT-switch separation, which could not be made small at will, as in this approach it is limited by the necessity of an anchor group to be conjugated to the switch part [54], [92]. The studies showed that the interaction between molecular switches and SWNTs increased when decreasing their separation. The most significant effects, however, were observed on the merocyanine (with strong shifts of its absorption bands and an increase of the merocyanine lifetime with respect to the spiropyran form) and not on the tubes. This approach, furthermore, was limited by the induced back isomerization (induced by the photons needed to optically excite the SWNTs) during the PLE measurements. This inhibited the observation of the influence of the dipole moment on the transition energies of the tubes. For more information please refer to Ref. [91], [92]. To circumvent such limitations we established a routine which yields SP-SWNTs hybrids with a close switch - SWNTs proximity by exploiting the micelle swelling approach.

5.3 Micelle Swelling

The micelle swelling approach, a new and simple functionalization approach which does not require sophisticated chemistry [55] (see Section 3.2.3) has been exploited to ensure a close tube switch proximity. It allows to investigate the interaction of molecular moieties when they lie in the close proximity of SWNTs without the need of specialized surfactants comprising both SWNT debundling and switchability [93], [94], [83]. It does not require any anchoring group to ensure the proximity of the switch to the nanotubes sidewall. The micelle swelling thus ensures a strong interaction between SWNTs and molecular switches, which increases the dipole-tube interaction compared to our previous studies, ensuring a contiguous position of the switch on the nanotubes surface.

5.3.1 Experimental

SWNTs were dispersed in SDS as described in Ref. [95] and [96]. A solution of CoMoCAT tubes (0.1 g/L) were dispersed in water with 1 wt% SDS and sonicated for 1 h at 20 W, followed by centrifugation at 31000 g. The prepared stock solution was used for preparing all of the samples to ensure identical amount of tubes in all the experiments. To transport molecules

into the tubes-containing micelles, 150 μL of THF yielding, respectively, 0, 50, 100, 150 μg spiropyran were added to 3 mL of nanotube stock solution. The mixture was stirred for 48 h in a water quench at room temperature. For the optimization study, the temperature was adjusted to 30°C, 45°C, and 55°C. The temperatures have been chosen to be lower than the boiling point of the solvent to avoid its evaporation before the switches penetrate the micelles. After the swelling procedure, the samples were centrifuged for 10 min to remove bundles that might have been formed or tubes no longer enclosed by a micelle. The samples were divided into two groups: One set was prepared in complete darkness (we will refer to them as the DARK samples in the rest of this thesis) while the other set was prepared under UV irradiation with a 366 nm lamp (we will refer to this as the UV sample). In the case of the UV samples, the switch solution was irradiated already before adding it to the SWNT suspension. In this way we ensure that the molecules entering the micelles in the DARK samples were mostly in their SP form while in the UV samples were mainly in the MC form. Please note that, while irradiating the samples with UV light, we reach a photostationary state that is given by the balance between the SP-to-MC light induced isomerization and the MC-to-SP thermally induced back isomerization. The value of this ratio is the highest conversion rate we may achieve at the working temperatures and in the given solvent. Thus, half of the final samples (the UV ones) were tubes coated with merocyanine and the other half (the DARK ones) with spiropyran.

5.3.2 Effect of the Dipole Coverage

As predicted by Malic *et al.*, the dipole-dipole interaction between the MC and the tubes lead to redshifts in the transition energies of the nanotubes. Up to now, the only experimental evidence of such shifts were changes of the absorption bands of the carbon nanotubes [89], [92], [54]. It was impossible to conduct photoluminescence excitation (PLE) measurements of the tubes coated with MC, as the excitation radiation (500-800 nm) required for performing a PLE map causes the back isomerization of MC into SP [91], [92], [54]. Absorption measurements, on the contrary, require less intensities; they do not trigger back isomerization and let us observe the influence of the dipole moment on the absorption bands of the tubes. Previous studies have shown that the lifetime of the merocyanine form gets longer as it gets closer to the nanotube sidewall, due to the increased π-π-interaction between the merocyanine π-electron and the tubes [91], [92], [54]. If merocyanine is directly adsorbed onto the nanotube surface, then it is expected to be locked in its state without isomerizing back. Such a behaviour was already observed for MC on a gold surface [97]. The micelle swelling approach offers the advantage to stabilize the state of the switch inside the micelle and to lock it. The switch remains in its configuration and back isomerization is inhibited, making it possible to study the emission energies of SWNTs decorated with spiropyran switches in both the SP and the MC form.
As the theoretical predictions suggest an optimal dipole-dipole interaction for specific dipole coverage, we varied the SP/MC switch concentrations in the micelle swelling to verify the effect of the coverage onto the optical response of the tubes. Figure 5.3 a) and b) depict the absorption spectra for the different switch concentrations in darkness and under UV radiation,

respectively, identifying the state of the switch. The characteristic MC peaks at 390 nm and 500 nm are observed in both the DARK (Fig. 5.3 a) and the UV (Fig. 5.3 b) sample. The increase in switch concentration shows an increase in the bands intensities. The absorption of the UV sample includes an additional peak around 400 nm, which is associated with stacked MC [98]. It is interesting to note that Fig. 5.3 a) indicates the presence of the MC peak even in the DARK sample, which should only exhibit the ring-closed SP form. The micelle swelling process inserts the molecules into a highly complex environment made of carbon nanotubes, water, THF and SDS. This presumably affects the SP/MC equilibrium point and leads to such behaviour. As water is polar, the hydrophobic SP is trapped in the special limited hydrophobic tube-micelle environment. This special environment and the limited space between the micelle and the tube can lead to the presence of MC in the DARK sample. Albeit the locked MC state and the presence of the MC in the DARK sample indicates tube-switch interaction, the main goal of this study was to observe the influence on the transition energies of the SWNTs for both the excitation and the emission of the tubes.

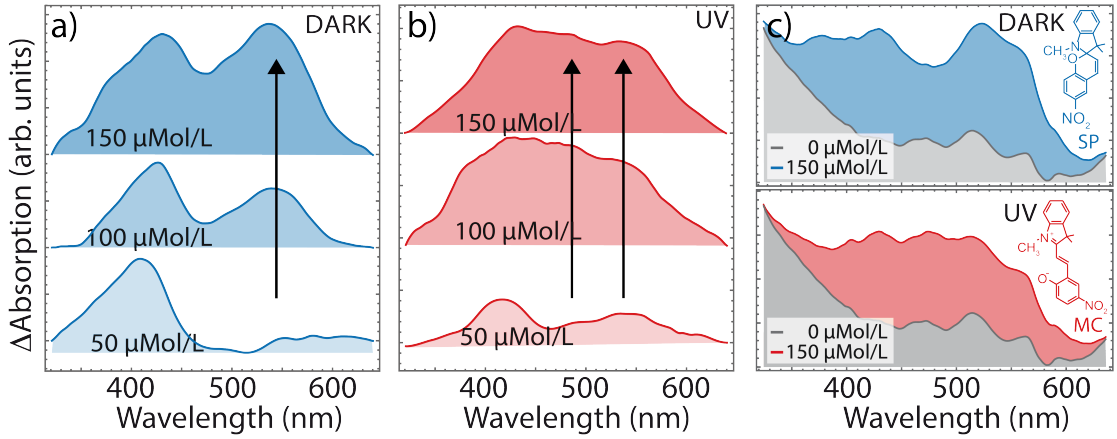

Fig. 5.3: Differential absorption spectra (reference spectrum: Pristine SWNTs) of the a) DARK and b) UV samples with different switch concentrations. c) Absorption spectra of the 150 μ mol L^{-1} samples in comparison to the pristine tubes.

The PLE measurements show clear differences between the UV and the DARK samples. A first striking feature is that, with increasing switch concentration, the emission yield from the DARK samples rises. The UV samples exhibit the opposite behaviour with a decrease in tubes emission when increasing the switch concentration. This behaviour is depicted for the (7,5) tube in Figure 5.4 a). We believe that the increase of emission of the DARK sample is due to the fact that the SP, which is a non-planar moiety, promotes exfoliation of small nanotube bundles and yield their further debundling, in a similar fashion as cholate derivatives do exfoliate the tubes. The interaction between strong MC dipoles within the micelle core and the ionic head of the surfactant could lead to destabilization of the micelles, resulting in a loss of tubes.
The presence of the switch, though, does not only affect the overall intensity emitted from our samples. As predicted by the theory, the dipole-dipole interaction between the switch and the SWNTs changes the excitonic binding energies of the tubes. The emission by the (7,5) tube species in Figure 5.4 b) demonstrates that the transition energies in the DARK sample remain constant. The points scatter by 2 meV around the pristine nanotube position, for both emission

and excitation energies. The UV sample, on the other hand, exhibits a shift of 9 meV for the E_{11} transition (emission energies) and 12 meV for the E_{22} transition (excitation energies). This trend is also observed for the other tubes. The pseudo PLE map in Fig. 5.4 c) compares the transition energies for the DARK and UV samples. The tubes in the DARK sample hardly show any peak shift with increasing switch concentration. Contrary, the UV samples exhibit diverse shifts for different nanotube chiralities and switch concentrations as highlighted by the bent arrows in the right panel. The fact that the shift increase with higher switch coverage of the tubes indicates that the given switch concentration is still below the optimal dipole coverage of 0.25 dipole/nm. When surpassing this value, lateral dipole-dipole interactions start interfering with the dipole-exciton interaction, leading to a decrease of the effective switch influence on the transition energies of the tubes. This phenomenon was experimentally observed by Kreft *et al.* for the switching molecule DHA/VHF [57]: The shifts increase by increasing the coverage of the tube and, after reaching a critical coverage, the shift will decrease. In our case, we observed a monotonous trend of continuous increase of the shift intensity by increasing the switch concentration and do not observe reduction of the shifts.

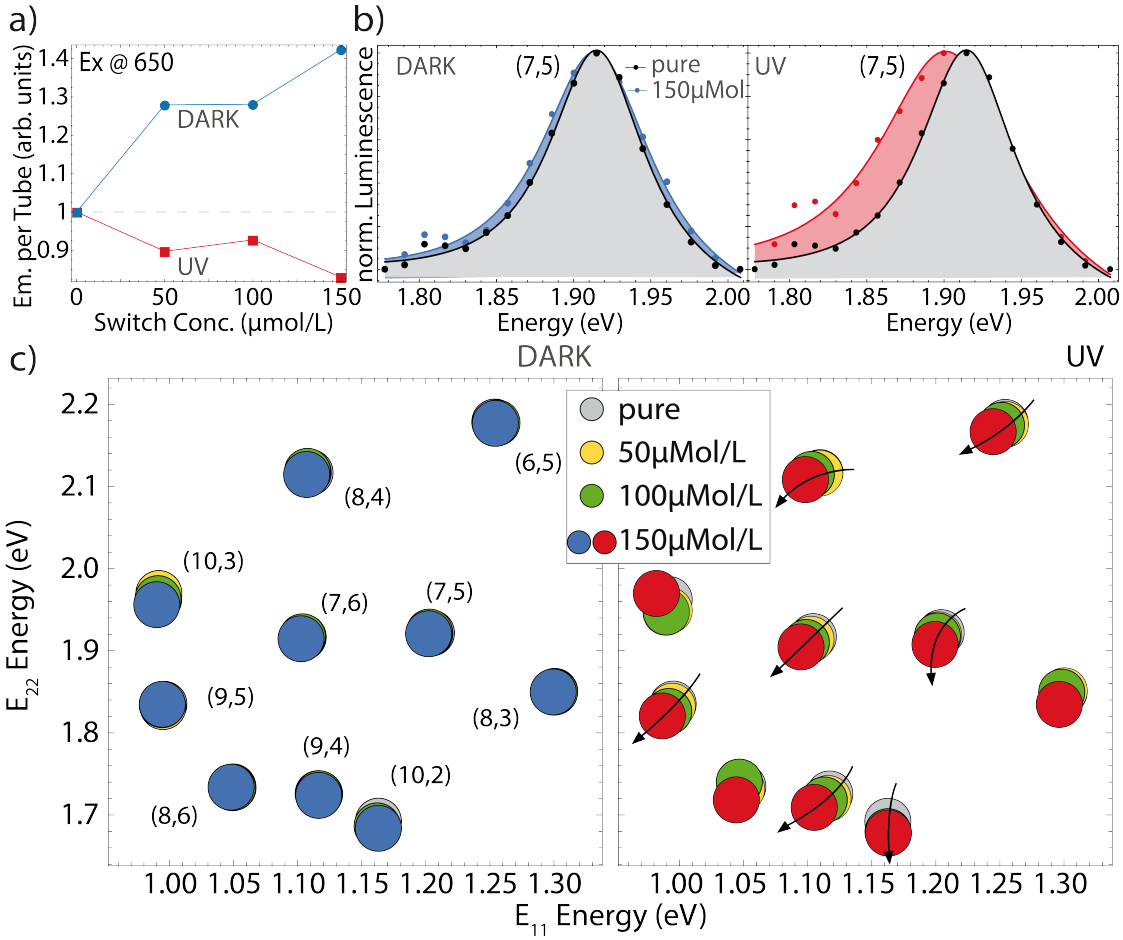

Fig. 5.4: a) Average luminescence of the tubes excited at 650 nm, obtained by the emission peak areas divided by the area of the absorption band after background removal. b) Emission of the (7,5) tube in the DARK sample and emission of the (7,5) tube of the UV irradiated sample. c) Pseudo PLE map of all the tubes. Left of the DARK sample and right of the UV sample.

5.3.3 Effect of the Dipole Intensity

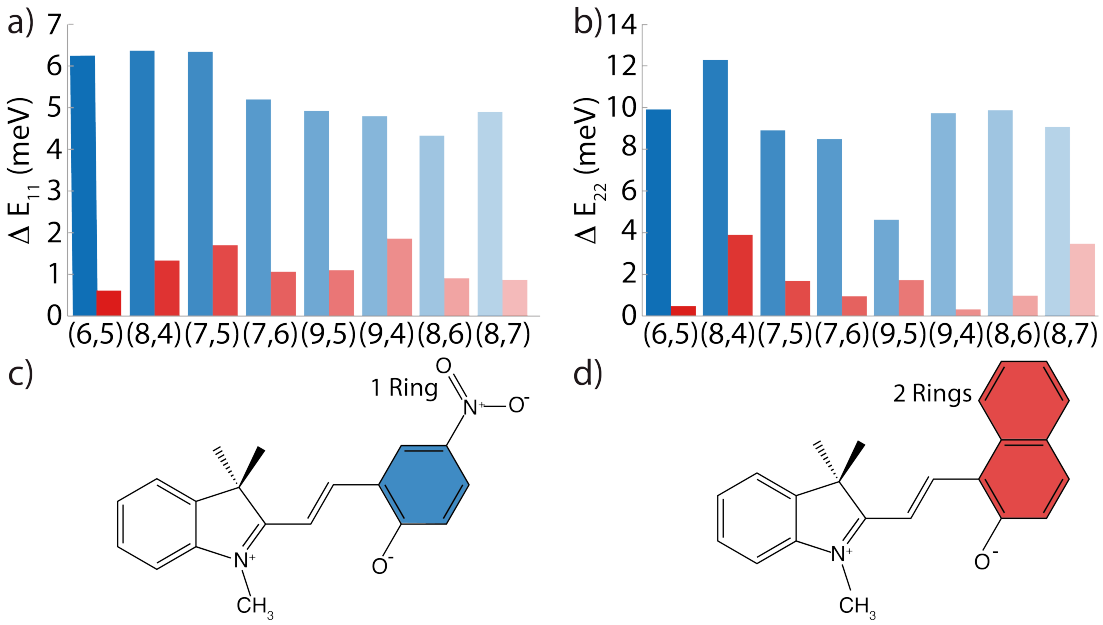

Fig. 5.5: Shifts in transition energy for the one (blue) and two (red) ring spiropyran derivative for a) E_{11} transition energies and b) E_{22} transition energies. Schematic illustration of the SP derivatives: c) Spiropyran with one aromatic ring and d) spirooxazin with two aromatic rings.

To further confirm the theoretical predictions, I monitored the shifts of the exciton energies for dipole switches with different dipole moments. I compared the dependence of the energy shifts to the magnitude of the dipole moment. To this purpose, I used two different derivatives of the spiropyran molecule of comparable size, sketched in Fig. 5.5: i) spiropyran, which has only one phenyl ring in the benzopyran part, highlighted in blue in Fig. 5.5 c), ii) spirooxazine, which has two phenyl rings, highlighted in red in Fig. 5.5 d). All derivatives undergo the ring opening and closing isomerization. By increasing the number of rings, the structures get more and more extended and the dipole moment becomes smaller (13.9 D for spiropyran, 6.64 D for spirooxazine) in the ring open form [99]. Those derivatives thus allow us to change the strength of the dipole moment while keeping orientation and coverage constant. The bar chart in Fig. 5.5 a) shows the shifts of the E_{11} transition energies and Fig. 5.5 b) the shifts of the E_{22} transition energies of the different tubes (150 μmol) for the different switches in their mero form. The biggest shift is observed for the one-ring derivative, whereas the switches with lower dipole moments induce smaller shifts. This supports the prediction that the change in exciton energy is proportional to the magnitude of the dipole.

5.3.4 Improving the Micelle Filling and Composition

We further improved our samples and studied the influence of the temperature on the production of our SP/MC-SWNTs hybrids. At higher temperatures the micelles expand [100], giving the switches more space to re-arrange, improving the homogeneity of the switch coating on

the tubes' surface, hence optimizing the micelle swelling process. To prevent the solvent to evaporate before entering the micelles we worked below the boiling point of THF (60°C), namely at 30°C, 40°C, and 55°C. Fig. 5.6 a) displays the influence of the temperature on the emission intensity of the resulting UV samples. The plain micelle-encapsulated tubes without any switch show a decrease in intensity with increasing temperature. All chiralities behave in the same manner, as it can be seen in the first column of Fig. 5.6 a). The other two columns depict the behaviour for samples with different concentration of switches, 100 μmol/L in Fig. 5.6 a) middle panel and 150 μmol/L switch concentration in Fig. 5.6 a) right panel. Those samples show a distinct increase in intensity for higher production temperatures.

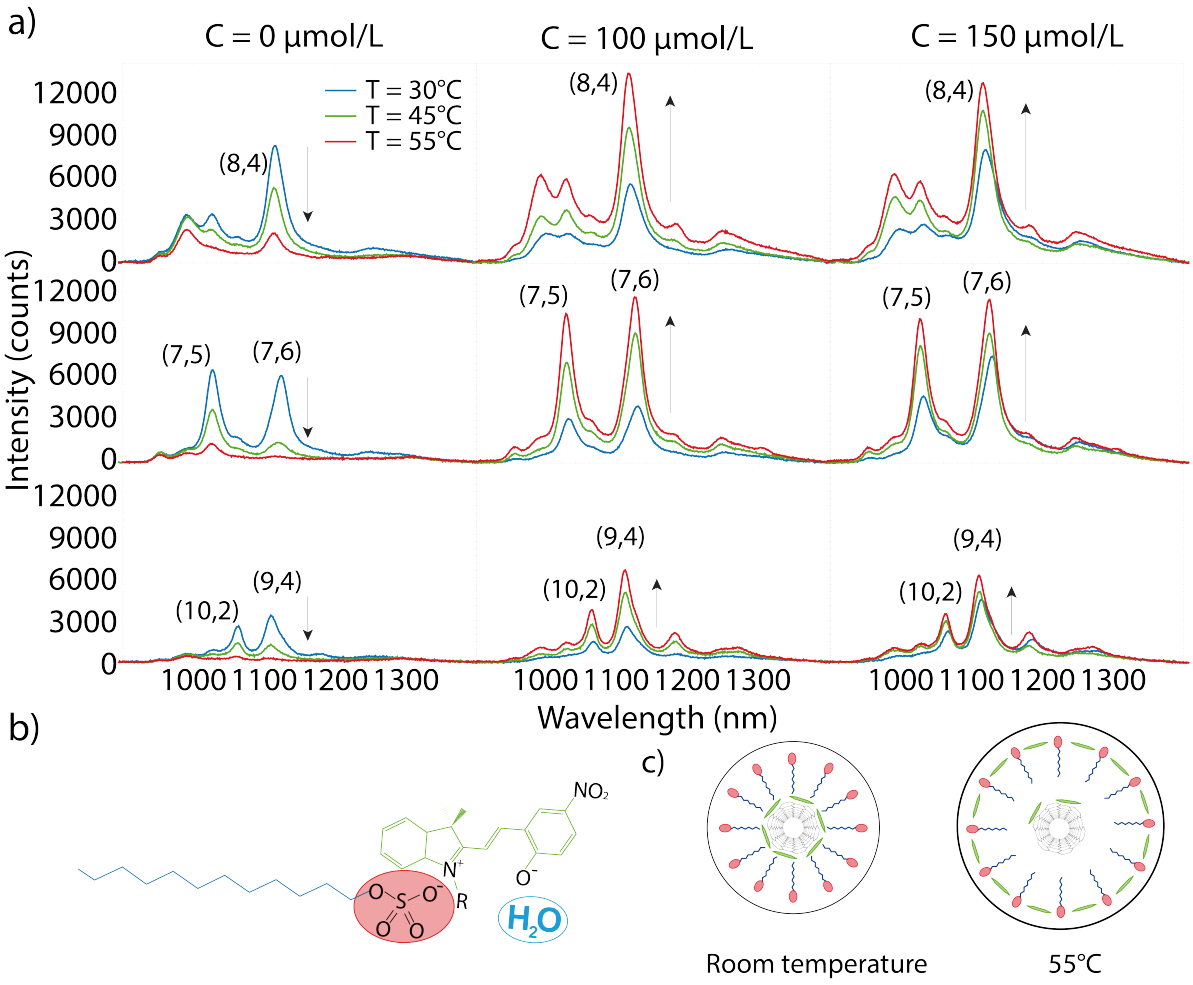

Fig. 5.6: a) Photoluminescence intensities of the samples prepared under UV radiation. The different producing temperatures (T=30°C, 45°C, 55°C) are indicated through the different plotting colours. From left to right the intensities of the different concentrations are displayed (c=0 μmol/L, 100 μmol/L, 150 μmol/L). From top to bottom the different chiralities corresponding to the different excitation energies (λ_{22} =590 nm, 650 nm, 730 nm) are shown. Additional mechanism influencing the micelle swelling process: b) Schematic structure of the MC- SDS ion pair with a water molecule as stabilization. c) Schematic structure of the new SDS-switch hybrid micelle. Due to the incorporation of the switch into the micelle less switch content is in close proximity to the SWNTs.

This behaviour can be explained when considering the micellization process. An increase in temperature results in a more pronounced movement of the SDS molecules making it more difficult for the anionic molecule to remain encapsulated within the micellar core. Some micelle break, triggering the SWNTs re-bundling or precipitation, resulting in quenched luminescence. The increase in intensity of the UV samples, on the other hand, indicates a stabilization of the micelles. The presence of the dipole moment of the switch reduces the polarity of the surfactants by forming MC-SDS ion pairs (Fig. 5.6 c), making the micelle less ionic [101]. The size of non-ionic micelles enlarges with increasing temperature, thus more and more switch content is able stabilize and penetrate the micelle [100]. Fig. 5.6c) depicts the stabilization process of the expanded outer shell: The SDS-MC ion pair, the water molecule between the methyl-group on the indolinic part, and the oxygen of the benzopyran moiety stabilizes the ion pairs.

Even if higher temperatures expand the micelles, competitive processes lower the composition of the final structures and only a tiny fraction of the switches is now penetrating and remaining within the micelle core. The other fraction will stabilize the hydrophilic shell of the micelle, resulting in a reduction of the overall dipole coverage of the tubes and thus affecting the shifts magnitude. The change of composition and morphology of the micelles swelled at higher temperatures changes the phenomenology of the optical response of the samples. The PLE measurements of the higher temperature samples display a different behaviour than samples prepared at room temperature. With an increase in temperature, we observe that the shifts do not correlate any more to the switch concentration, they rather depend upon the tube diameter, the larger the diameter the greater the shift. This behaviour is depicted in Fig. 5.7 a) for the 150 μL concentrated DARK and UV samples prepared at 55°C and compared to the 30°C ones. A similar but much weaker behaviour is also observed for the other samples at higher temperatures and even at lower switch concentrations. It is worth noting that such diameter-dependent shift was not observed for the samples prepared at room temperature. The difference in the phenomenology is ascribed to the fact that by increasing the temperature, the separation between the tubes and the switches increases. This reduces their mutual Coulomb interaction. At higher temperatures, the MC dipoles are localized in the outer shell of the micelles, so far away to make the dipole-dipole induced shifts negligible and no constant dipole-induced shifts can be observed.

The shifts we experimentally observe nicely follow the trend described by the Choi and Strano model for solvatochromic effects on SWNTs [29]. As highlighted in Section 2.4.4, those shifts in the emission and absorption of a nanosystem originate from changes in the dielectric environment [49]. Table 5.1 depicts the values for the DARK and UV samples prepared, respectively, at 30°C and at 55°C. The values for the slope increase for the higher production temperature. The main changes can be observed in the emission (E_{11}), e.g. the value for the UV sample rises from 0.076 eV^3 nm^{-4} (30°C) to 0.101 eV^3 nm^{-4} (55°C), concluding that the formation of the SDS-MC hybrid surfactant is changing the dielectric environment of the tubes leading to higher solvatochromic shift which are known to be diameter tube dependent [29].

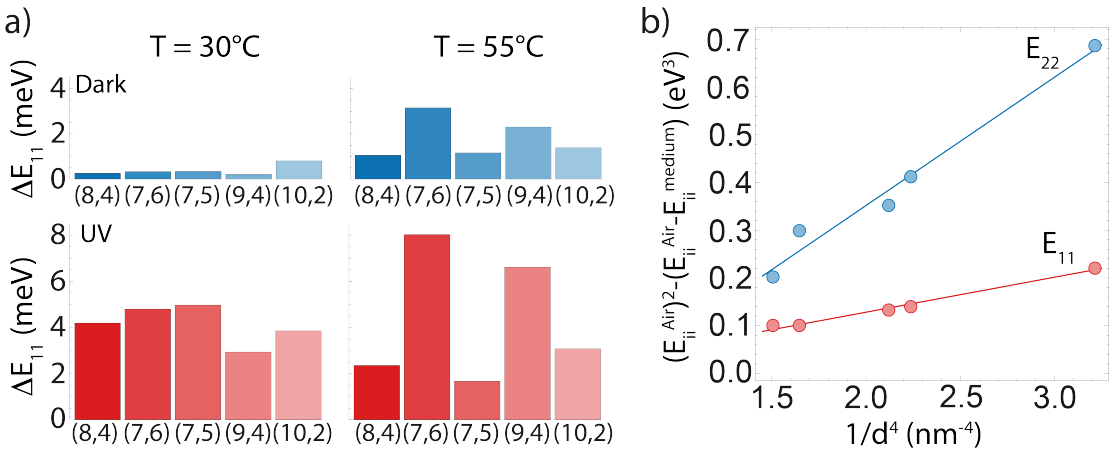

Fig. 5.7: a) Comparison of the shifts for different tube species between DARK and UV samples with a concentration of 150 μmol l^{-1} prepared at 30°C (left panel) and 55°C (right panel). b) Solvatochromic shifts of the E_{11} transition of the 150 μmol samples prepared at 30°C and 55°C.

The increase in temperature stabilizes the micelles by incorporating the switches into their outer hydrophilic shell, which lowers the number of molecules at the surface of the SWNT. The dipole-dipole interaction of the tubes and the switches becomes negligible. We observe the solvatochromic shifts of the SWNT transition energies due to the change in the dielectric environment. Working at room temperature, therefore, is the best configuration to ensure that the switches are closest the to the SWNT sidewall. It is thus the most beneficial for observing the dipole-dipole induced shifts in the transition energies for SWNTs decorated with molecular switches.

30°C	E_{11} (eV^3 nm^{-4})	E_{22} (eV^3 nm^{-4})	55°C	E_{11} (eV^3 nm^{-4})	E_{22} (eV^3 nm^{-4})
DARK	0.074	0.27	DARK	0.082	0.28
UV	0.076	0.29	UV	0.101	0.3

Tab. 5.1: Comparison of slopes obtained for the DARK and UV samples prepared respectively at 30 °C and at 55 °C.

5.3.5 Challenges

The micelle swelling technique is helpful to investigate the general interaction between the dipole moments of molecular switches and the transition energies of SWNTs. However, it has several disadvantages. The first striking feature is the locking of the switch state. For real technical application such as sensors and memory devices the ability to isomerize back and forth reversibility must be preserved. Another downside is the sensitivity towards changes in the environment. Drop-casting of the compound would lead to a bursting of the micelle and disruption of the close tube-switch interaction. In order to overcome this obstacle the newly introduced [2+1] cycloaddition method provides a way to firmly anchor spiropyran on the tubes sidewalls. In the coming section I will show our results on this approach.

5.4 Covalent Functionalization

Here I will show how the new introduced [2+1] cycloaddition reaction can be utilized to attach photochromic molecular switches on the SWNTs. I will then highlight the novel phenomenology arising when pursuing this approach[1].
The spiropyran was synthesized on the sidewall of the triazine decorated nanotube. Figure 5.8 a) displays a sketch of the synthesis of the SP-SWNT hybrid. In the first step indoline replaced the chlorine atom of the triazine, forming an SWNT-indol compound. In an additional step nitrosalicylaldehyde was added forming the aimed SP-SWNT hybrid. The elemental analysis and XPS characterization confirmed the attachment of spiropyran onto every 100th carbon atom. The spiropyran decoration mainly induces additional peaks in the N1s XPS spectra (see Fig. 5.8 b): Peak D is weakly observed below the peak of the bridging nitrogen B and the nitrogen of the triazine ring A. It corresponds to the nitrogen present in the indol part of the spiropyran. The second peak, located at 405.49 eV, is connected to the nitro group C. The presence of those supplementary peaks confirms the successful spiro functionalization. For the complete chemical characterization of the synthesis please refer to the supporting information of Ref. [8]. Here I will mainly focus on the influences of the change of the switch state on the optical properties of the SWNTs.

5.4.1 Isomerzation Process

Spiropyran undergoes a ring opening transition under UV irradiation. This can straight forwardly monitored by the change in absorption spectra. The characteristic bands arising at 390 nm and around 590 nm indicate the ring opening process and can be reversed by visible light or thermally by storing in darkness. To monitor the isomerization process after the attachment we irradiated the samples with UV light (see Fig. 5.8 c). The most striking difference between free merocyanine and SP-SWNTS is that the latter only displays the absorption band at 390 nm. The characteristic merocyanine band at 590 nm - which gives MC its colour - is not detectable. This peak is ascribed to the π-electron confined along the MC structure. The vanishing of the peak is the core of the innovative character of the novel functionalization approach. The attachment of the spiropyran on the nanotube enables the electron to extend over the entire construct including the nanotube. This results in a shift of several hundred nanometers into the far infrared, a region which is not detectable any longer. Such a redshift was already observed before for SP attached onto several molecular moieties [102]. The net effect of the isomerization is thus a release of the electron into the SWNTs. This effects the electron density of the tubes and induces an additional, reversible shift in the position of their Fermi level.

[1]The results of this section have been published in Nature Comm. [8].

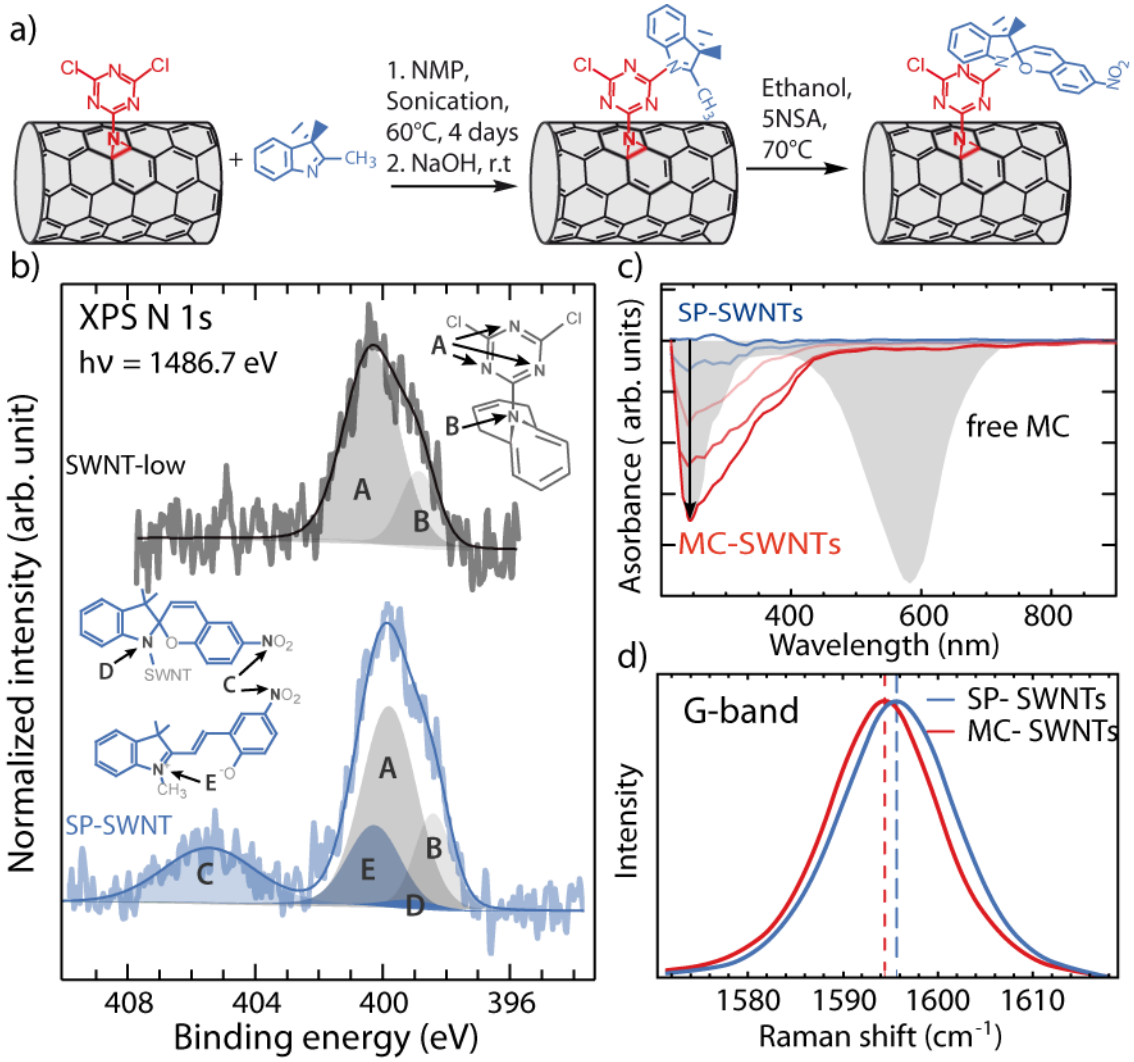

Fig. 5.8: a) Synthesis steps for the immobilization of spiropyran on the triazine. b) XPS N1s spectra of the low functionalized triazine sample and the spiropyran sample. c) Absorption spectra of the isomerization process of the attach spiropyran on the SWNTs. d) Raman spectra of the SP-SWNTs and MC-SWNTs samples.

5.4.2 Effects on the optical properties of the Tubes

The changes in Fermi level were observed via Raman measurements, depicted in Figure 5.8 d). Comparing the SP-SWNTs before and after UV irradiation (MC-SWNTs) we observe a shift of the position of the G band by 2 cm^{-1}, corresponding to a 0.2 eV change in Fermi level. The change could be reversed by back isomerization: Please note that the back isomerization could not be triggered by irradiation with visible light as the 590 nm band is now missing in our samples. The new SP-SWNT hybrid got restored to its ground state by thermal back reaction in darkness. The reversible change in Fermi level is attributed to doping due to the exposure of ultraviolet photons. The release of charges after the isomerization process does not only affect the Raman response of the tubes, but has tremendous impact on the luminescence behaviour of the tubes as well. Figure 5.9 displays the 2D PLE maps of the SP-Tubes before and after isomerization. The attachment of the SP on the tubes sidewalls does not alter the optical

properties of the SWNTs. After the isomerization process, however, we observe a strong change in the emission intensity. After irradiation with UV light, we observe quenching of the emission of approx. 50%. The quenching effect was reversed after storing the sample in darkness. This effect is due to the change in Fermi level that reduces the rate of radiative emission of the tubes, consistent with similar previous observation for other doped nanotubes systems [103], [104].

Our original idea was to coat SWNTs with the molecular switch spiropyran to observe the coupling of the molecular dipole moment with the excitons of the SWNTs to influence the transition energies, as already observed for the non-covalent approach. As seen in Fig. 5.9 b) the isomerization process induces no changes in the transition energy of the tubes. One could assume that the tube-switch separation might be too large due to the triazine "spacer" as observed by Bluemmel *et al.* [92]. Another explanation is that the dipole coverage is too low as we only have one SP attached to every 100th carbon atom. The doping of the SWNTs and the absence of the 590 nm absorption band, however, suggest that the π-conjugated system looses the zwitterionic character of the MC changes due to the linkage to the nanotube. The π-electron of the MC is no longer trapped inside the spiropyran molecule but delocalized along the nanotube. This reduces the charge density of the MC inhibiting the change of the dipole moment and the dipole interaction with the SWNTs.

The new hybrids reveal outstanding optical properties. The injection of UV photons induced changes in the Fermi level and lowered the light emission of SWNTs. Thus, we can reversible control the optoelectronic properties of nanotubes with the new functionalization routine, paving the way to advanced applications such as light-switchable ballistic transport channels.

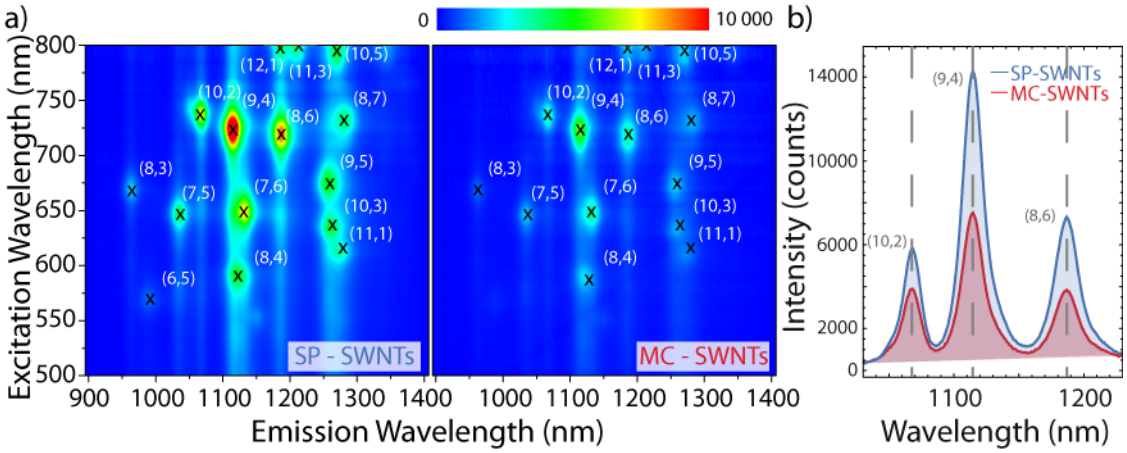

Fig. 5.9: a) 2D PLE map of the SWNTs functionalized with the molecular switch. The left panel shows the SWNT emission in the spiro state, whereas the right panel shows the luminescence of the tubes in the mero form. It can be seen that the isomerization process quenches the tubes intensity. b) Single emission line at 725 nm comparing the intensity of the (10,2), (9,4), and (8,6) before the and after UV radiation.

5.5 Comparison

In this chapter I investigated the interaction of the molecular dipole switch spiropyran with carbon nanotubes. Several functionalization routines are possible to immobilize the molecular switch spiropyran on the sidewalls of SWNTs. Using pyrene as an anchor hinted towards the theoretical prediction made by Malic *et al.* The limitation was set by the tube-switch distance and the back isomerization of the merocyanine induced during the PLE measurements. Micelle swelling helped overcoming this problem by locking the switch state inside the surfactant micelle and realizing a close tube switch interaction. We demonstrated that micelle swelling is a simple and successful method to investigate the interaction of the dipole switch spiropyran with carbon nanotubes. We verified the theoretical predictions on the effect of the dipole moment of merocyanine on the excitation and emission energies of the SWNTs. To further validate the predictions, I compared the shifts for molecules with similar morphologies but different intensity of their dipole moments. We investigated the effect of the temperature on the hybrid production process to identify the preparation conditions with the highest dipole coating of the tubes. The aimed reversible alteration of the optical properties could not be achieved as the strong π-π-stacking inside the micelle prohibits any back isomerization from MC to SP. Attaching the spiropyran covalently on the tubes revealed new promising physical features. The reversible injection of electrons from the spiropyran into the SWNTs lead to reversible alterations of the optoelectronic properties of the tubes, allowing for new sophisticated optoelectronic applications.

6 CNT-Dye hybrids

One of the characteristics features of SWNTs is their polydisperse occurrence and the requirement of a special excitation wavelength that is unique for a certain chirality, as mentioned in Sect. 2.4.3. Thus, using a specific excitation wavelength, only a small fraction of the tubes present in a sample will be able to emit, making direct optical excitation a relatively inefficient process. At this stage of the growth technology it is impossible to grow a batch of a single SWNT chirality. Being able to excite all tubes in one sample at once would be beneficial for optical applications of SWNTs. One solution would be to separate the nanotubes to achieve enriched single species. Several approaches have been made to sort SWNTs post production. It was shown that specific DNS strands show selective behaviour towards certain diameters [105], [106]. Krupke *et al.* successfully separated solubilized metallic SWNTs via dielectrophoresis [107]. Density gradient ultracentrifugation could separate semiconducting tubes [108], [50]. Other methods showed to be successful to even individualize single chiralities [109]. All approaches are quite promising but lack in efficiency and scalability. An alternative solution to this problem can be achieved through indirect excitation of the tubes via energy transfer from chromophores immobilized on the SWNTs. Energy transfer in nanotube chromophore complexes enables the excitation of SWNTs through a single excitation wavelength, paving the way for efficient nanotube field effect transistors or full implementation of SWNTs as biomarkers. In the following I want to introduce the interaction between SWNTs and dyes, paying particular attention to the dye perylene.

6.1 Chromophore-SWNT Interaction

Chromophore is an ancient greek word ($\chi\rho\omega\mu\alpha$ chroma-colour and $\varphi o\rho o\varsigma$ phoros-carrier) meaning colour bearer and derives from their intense colour. A chromophore is an extended delocalized system of electrons, giving rise to its staining. Chromophores can be exploited as a major tool to overcome the chirality selective excitation of polydisperse carbon nanotubes and the consequently polychromic excitation wavelength. The monochromic nature of chromophores can be used to trigger simultaneously light emission from all species in one sample. Chromophores, furthermore, show a broad emission in the visible range, usually matching the absorption range of SWNTs (E_{22} transistion). Thus, when exciting a chromophore immobilized on a SWNTs sidewall, their excitation energy can non-radiatively transfer into the SWNTs, indirectly exciting all the tubes whose E_{22} transition overlaps with the emission of the chromophore. The concept itself seems to be quite trivial, the implementation though

remains rather challenging. The dye-tube distance is crucial as the efficiency of the energy transfer in Förster - like processes scale with $\sim r^{-6}$, demanding a close proximity between both components.

The first attempt towards energy transfer between dyes and SWNTs had been pursued by Qu *et al.* [110]. They covalently functionalized SWNTs with a pyrene derivative and observed quenching of the pyrene emission. Anyway, as the tubes' emission was quenched due to the covalent functionalization, no proof of indirect excitation of the tubes could be observed. A more concrete proof of energy transfer in SWNT chromophore complexes was observed in MWNT covered with perylene. A change in photocurrent was observed, indicating formation of additional e-h pairs due to the perylene excitation [111]. Ehli *et al.* investigated the interaction of functional perylene bisimides surfactants with SWNTs. They designed perylene surfactants and observed charge transfer between the SWNTs and the dye accompanied with strong quenching of the perylene by a factor of more than 100 [112]. The first proof of emission through indirect excitation of SWNTs through a dye was provided by Ernst *et al.* with perylene and by Roquelet *et al.*with porphyrin.

Ernst *et al.* introduced an amphiphilic perylene-based molecule for functionalizing SWNTs. The PerPG (perylene polyglycerol dendron) is a rationally designed functional surfactant with alkyl chains for isolating the SWNTs, hydrophilic dendron heads for ensuring the SWNTs solubilisation, and the perylene core as the functionality. They observed highly efficient energy transfer (~ 1) from the PerPG to the tubes, making it possible to excite at one distinct wavelength several SWNT chiralities. The energy transfer comes at the cost of the perylene luminescence, which is quenched by a factor of 10^4. The perylene sticks via strong π-π-stacking on the SWNTs with a tube dye distance of approx. 0.9 nm [51]. Roquelet on the other hand exploited the micelle swelling approach. They swelled porphyrin molecules inside the micelle encapsulating the SWNTs, observing indirect excitation of the (6,5) tubes mediated through the dye [56], [113].

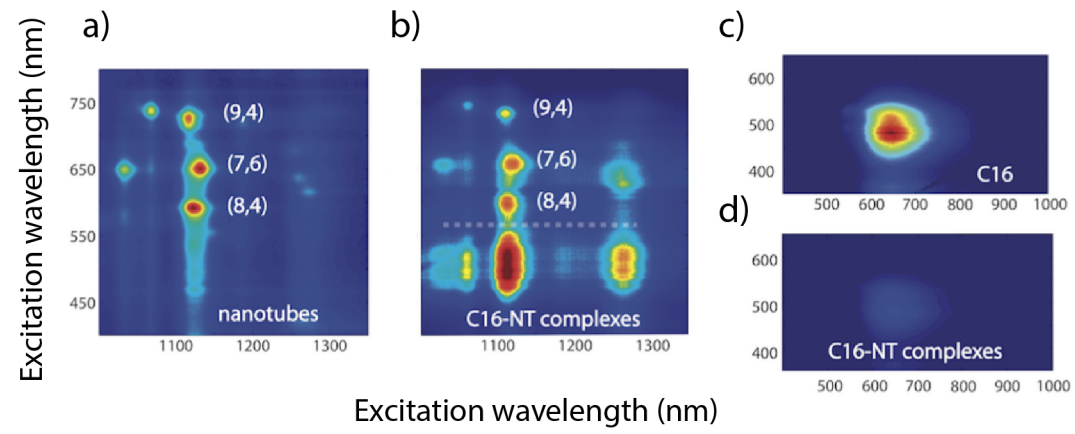

Fig. 6.1: a) PLE map of Sodium Cholate suspended SWNTs and b) PLE map of amphiphilic perylene-based molecule functionalized SWNTs. In both samples the characteristic emission and excitation peaks of the SWNTs can be observed. The perylene samples additionally exhibit indirect emission of the SWNTs through the perylene (below the grey line). c) The perylene emission before and d) after attachment onto the SWNTs. A clear quenching can be observed. Figure taken from Ref. [114]

6.1.1 Förster Resonant Energy Transfer

The interaction in perylene-SWNTs hybrids can be described as a Förster energy transfer. In this process, the excitation of a donor (perylene) is transferred via dipole-dipole interaction non-radiatively into the acceptor (SWNTs). This process occurs if the emission of the donor overlaps with the absorption spectrum of the acceptor, as seen in Fig. 6.2 a). The processes also depends strongly on the distance between acceptor and donor. Figure 6.2b) schematically displays the distance dependence between the donor and acceptor. For smaller donor-acceptor distances the energy transfer efficiency (ETE) is increased. A more efficient energy transfer process leads to an stronger fluorescence signal of the acceptor while respectively, is the emission of the donor gets quenched. The quenching magnitude is an important factor for determining the ETE.

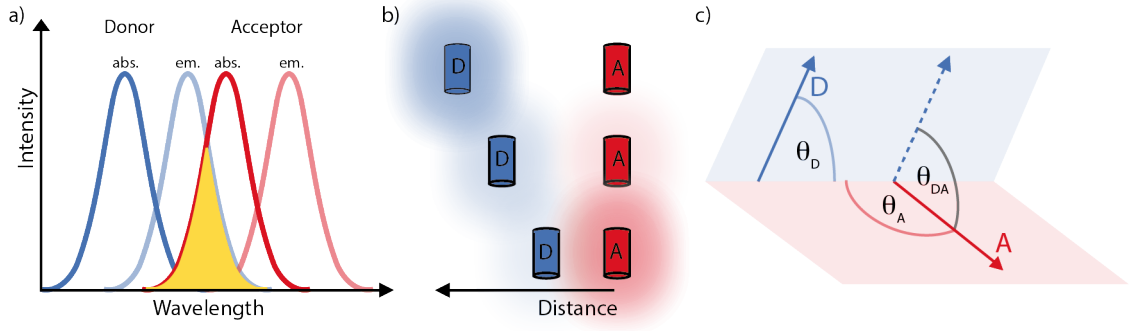

Fig. 6.2: a) Scheme of the spectral overlap required by the Förster transfer to take place. b) Schematic depiction of the excitation transfer from the donor to the acceptor. With decreasing distance the donor excites the acceptor, consequently does this process induce quenching of the donor. c) Orientation of the vibrational plane of the donor and acceptor involved in the Förster transfer. Adapted from Ref. [115], [116].

The main parameter of the Förster transfer is the Förster radius R_0. It describes the distance at which half of the donors excitation is transferred to the acceptor. R_0 can be derived by the following equation:

$$R_0 = 0.2108\,[\kappa^2\,\Phi_{0D}\,n^4\int_0^\infty I_D(\lambda)\,\epsilon_A(\lambda)\,\lambda^4\,d\lambda]^{1/6}, \tag{6.1}$$

where Φ_{0D} is the fluorescence quantum yield (QY) of the donor in absence of the acceptor, n is the refractive index of the medium, κ^2 is the oriental factor including the orientation of the emission dipole of, both, the acceptor and the donor and can be calculated according to:

$$\kappa^2 = (\cos\theta_{DA} - 3\cos\theta_D\cos\theta_A)^2, \tag{6.2}$$

I_D is the fluorescence spectrum of the donor and is normalized to $\int_0^\infty I_D(\lambda)d\lambda = 1$.
$\epsilon_A = \frac{A}{cL}$ can be obtained via the absorption and concentration of the SWNTs and the optical

path length. Given the Förster radius and the distance between the donor and acceptor the ETE can be calculated as:

$$\Phi_T = \frac{k_T}{1/\tau_D^0 + k_T} = \frac{1}{1 + (r/R_0)^6,} \tag{6.3}$$

where k_T is the rate transfer between the donor and acceptor at distance r. Φ_T defines the expected ETE of an investigated system.

From the experimental data the actual ETE can be calculated according to the following equation:

$$\Phi_{Ex} = 1 - \frac{\gamma_{A \longrightarrow D}}{\gamma_D}, \tag{6.4}$$

with $\gamma_{A \longrightarrow D}$ being the transfer rate from donor to acceptor and γ_D the excitation rate of the donor. This value is given by the quenching of the donor (perylene) luminescence in the presence of the acceptor and can be directly obtained from the PLE measurements of the in presence and absence of the acceptor (SWNTs).
Last, the magnitude of the expected indirect emission η_T of the tube with the actual experimental observed one can be compared by:

$$\eta_T = \Phi_{Ex} \cdot \frac{f_{perylene}}{f_{SWNT} \cdot N} \tag{6.5}$$

$$\eta_{ex} = \frac{I_{transfer}}{I_{SWNT}}, \tag{6.6}$$

where $f_{perylene}$ is the oscillator strength of perylene (~ 0.1) and, respectively, f_{SWNT} of SWNTs (~ 0.01) and n the perylene coverage [117]. $I_{transfer}$ is the fluorescence intensity of the indirect SWNTs emission and I_{direct} of the direct tube emission obtained from the PLE measurements.

Here I will report on the results of novel strategies we developed to decorate SWNTs with perylene will be introduced. Instead of incorporating perylene into the core of a surfactant, a perylene based polymer was synthesized to ensures strong immobilization of the perylene on the SWNTs sidewall [118] . Polymer wrapping is beneficial compared to surfactants as they i) wrap more firm around the SWNTs sidewall, ii) are more robust towards environmental changes, and iii) are more versatile - the single building blocks of the polymer can be changed and alternating functional moieties can be incorporated. In the second approach the perylene was attached via the covalent [2+1] cycloaddition[1].

[1]Both projects were joint collaborations between the group of Prof. Haag from the chemical department Berlin and the group of Prof. Reich from the physics department at the Freie Universität Berlin. I contributed to both project by participating in the experiments design, preparing the SWNT solutions as well as performing the optical characterization of the perylene SWNT hybrids. Section 6.2 is taken from our publication in Small [118] with a shared first authorship between Katharina Huth and me.

6.2 Polymer Wrapping

Polymer wrapping is a well-established functionalization routine to individualize SWNTs and to attach functional moieties to their sidewalls. This method benefits from the tight and uniform enclosure of the SWNTs by the polymer. It endures filtration, local changes in the pH, and other environmental changes [61]. We exploited the polymer wrapping method to functionalize SWNTs with the bright chromophore perylene. The polymer complex consists of an alkylated polymer conjugated with dendronized perylene bisimides. This way, the perylene can be attached onto the SWNTs in a monotonous and well-ordered structure, preventing stacking of the perylene. An additonal advantage of this method is that the SWNTs serve as a skeleton allowing to align the perylene in a ordered structure, localizing the fluorescence marker around the tube. This can be be beneficial for biomedical purposes. The experimental details of the perylene-polymer synthesis and characterization, performed by Katharina Huth, can be found in Ref. [118].

6.2.1 Optical Characterization of the SWNT-Polymer Hybrid Complex

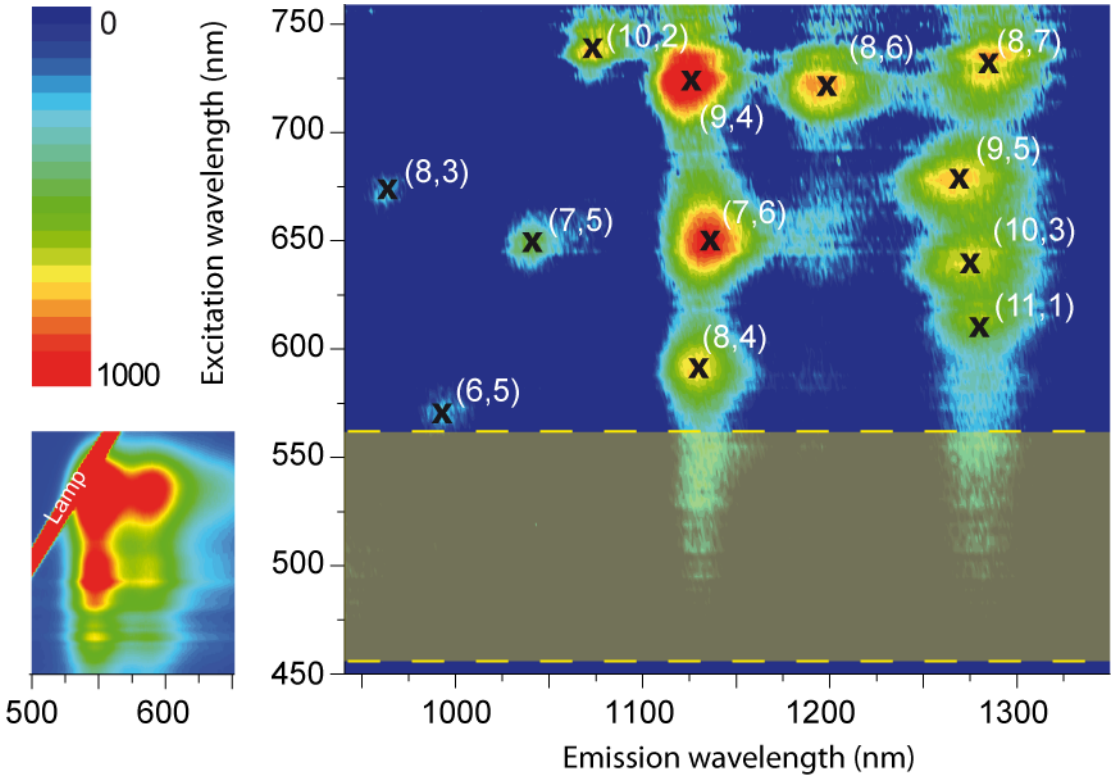

Fig. 6.3: a) The 2D-PLE map of the debundled $P_{perylene}$-P_{alkyl} complex shows no energy transfer in the expected excitation window between 460 to 560 nm. In the yellow highlighted area perylene mediated emission would be expected. The 2D-PLE map of $P_{perylene}$ on the left serves as a guide to the eye.

To ensure that the SWNTs are well isolated, I conducted photoluminescence excitation (PLE) measurements. I monitored the dispersion ability of the polymer wrapped SWNTs and the influence of the perylene on the tubes and vice versa. In a first step the perylene-polymer ($P_{perylene}$) was wrapped around the SWNTs. Here it is crucial to a) find a sufficient coverage to observe the energy transfer between the dye and the tubes and b) not exceed a certain coverage to prevent interaction between the dendrons, and c) provide enough of the polymerbackbone (P_{alkyl} to ensure debundeling of the tubes. PLE measurement with a dye concentration of 10^{-5} μM showed that the amount of polymer was too low to individualize the SWNTs successfully. In a second step, additional polymer (P_{alkyl}) (1.8 g/L) was added to ensure further debundeling of the tubes without increasing the dze concentration. I monitored the emission of the SWNTs to estimate the polymers' solubilization ability and any potential dye-tube interactions as depicted in the 2D PLE map of the $P_{perylene}$-P_{alkyl}-SWNT complex in Figure 6.3. The map shows emission from up to 12 different tube species after debundling, which proves the successful solubilization of the tubes. The yellow highlighted region in the PLE map corresponds to the absorption region of the dye polymer $P_{perylene}$, shown on the left side of the panel in Figure 6.3). Indirect emission of the SWNTs mediated by the perylene would have occurred in this region [51]. No energy transfer from the perylene to the tubes can be observed.

To further investigate the tube-dye interaction I monitored the emission of the perylene. After the first functionalization step with the $P_{perylene}$ I observed a drop in the perylene emission intensity, of approximately 75%, as seen in Figure 6.4. When further promoting the SWNTs debundling by the addition of the P_{alkyl}, I observed an increase of the perylene emission, which gets restored up to 50% of its initial intensity. The quenching factor allows to determine the ETE of the $P_{perylene}$-P_{alkyl}-SWNT system. According to Eq. 6.4 Φ_{Ex} is equal to 0.5. The perylene coverage of the tubes with the given concentration of 10^{-5} μM is in the range of $\sim$ 2% [2]. The expected intensity of the perylene mediated SWNT emission should be 10% of the direct SWNT emission intensity (Eq. 6.5), a rather inefficient yield compared to other energy transfer systems. Even an increase in perylene concentration did not result in the aimed energy transfer[3]. The recovery of the perylene emission after the addition of P_{alkyl} indicates a

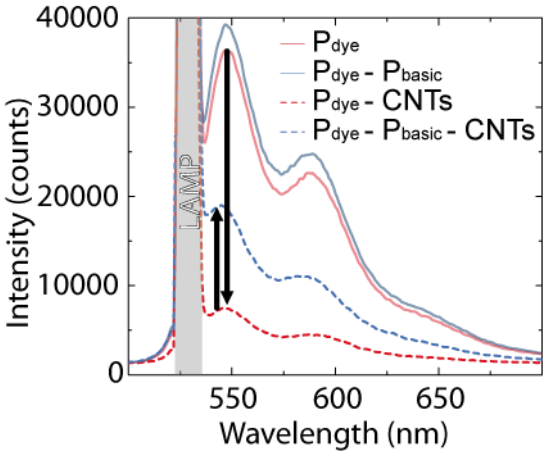

Fig. 6.4: Perylene emission spectra of indicated compounds at an excitation wavelength of 530 nm. The functionalization of the dye polymer onto the SWNTs leads to a decreased perylene emission intensity. Later addition of native polymer P_{alkyl} recovers the emission.

[2] Ernst *et al.* achieved a perylene coverage of 10% with a concentration of $6{\cdot}10^{-5}$ μM, thus, I reasoned to have a six times lower coverage of $\sim$ 2%

[3] I prepared samples with higher perylene concentration (ranging from 10^{-5} μM-10^{-6} μM) to increase the perylene coverage of the tubes, none of those samples showed indirect emission of the tubes.

shielding effect. It can be assumed that P_{alkyl} further covers the tubes and inhibits the dye from interacting with the tubes and vice versa. Furthermore, can be expected that the perylene is oriented nearly orthogonal to the tube. Such an arrangement reduces the ETE tremendously. Those findings revealed that the setup of our $P_{perylene}$-P_{alkyl}-SWNT system is not suited for energy transfer. The nature of the samples, however, offers the alternative to use the hybrids for biomedical purposes.

6.3 Biomedical Application

Fluorescent nanomaterials are expected to revolutionize medical diagnostic, imaging, and therapeutic tools due to their superior optical and structural properties. Their inefficient water solubility, cell permeability, biodistribution, and high toxicity, however, limit the full potential of their application. Different nanosystems, such as quantum dots, micelles, and silica particles have been investigated to overcome such barriers [119], [120]. Also carbon nanotubes have excellent prospects for cancer therapeutics as well as for a broad range of biomedical purposes. They can be used for DNA, protein, and virus detection, for tissue engineering, biological imaging, and targeted drug delivery [6]. Their long and hollow structure offers the possibility to enable more than one function on the same tube, contrast agents, drugs, or reporter molecules can be used simultaneously. Cancerous cells could be detected, visualized, and treated by inserting only one therapeutic SWNT-hybrid [121]. SWNTs stand out in the nanometric world for their exceptional length to side ratio called aspect ratio. Their sidewalls extend up to the micrometric level, providing a stable platform for immobilization of active molecules at large concentrations and with high degree of localization. Their emission in the near infrared (NIR) makes them especially attractive for biological imaging. The transparency window of biological tissue lies in the range of 650 to 1350 nm: The first optical window is located between 650 nm and 950 nm matching the excitation range of SWNTs and the second optical window covers the range from 1000-1350 nm, which coincides with the emission range of SWNTs [122]. Their insolubility, toxicity, and low emission quantum yields (QY below 1%) has hampered them from extensive use in biomedical applications. Bile salt surfactant have shown to debundle SWNTs and to increase their quantum yields but at cost of their biocompatibility [123]. Non-covalent PEGylation has shown to promote the biocompatibility of SWNTs but compromising their low QY [123]. Welsher *et al.* found a way to combine both aspects. They first solubilized SWNTs with sodium cholate and then replaced it with phospholipid-PEG, sustaining their QY [119], [7]. The use of nanoplasmonic colloids represents another promising way to increase the QY by enhancing the SWNT emission [11]; but generally QYs remain low compared to common fluorescent dyes such as cy3 (4%), rhodamine (12%), or bodipy (4%) typically used in fluorescence microscopy [124], [125], [126].

Also perylene bisimides possess excellent properties for bioimaging purposes such as high chemical and photophysical stability, outstanding fluorescence properties, and long emission wavelength. They have been versatile employed as fluorescent labels [10], [127], [128], [129], [130],

membrane markers [131], [132], or anti-inflammatory agents [133]. A major drawback is their aggregation tendency in aqueous solution caused by the polyaromatic scaffold of the perylene cores resulting in fluorescence quenching. Charged groups have been introduced in the bay-regions [134] or imide positions [10], [133] to overcome the aggregation behaviour and preserve their fluorescence properties with QYs up to 100% [10].

We exploited our polymer-functionalized SWNTs with bright perylene fluorophores as cytocompatible SWNT hybrids for potential bioimaging applications. Polymers are attractive dispersing agents for SWNTs because they can wrap around the SWNT backbones attaching different functional moieties onto their sidewalls [60], [135], [136], [137], [138] The well-established polymer wrapping method benefits from the tight and uniform enclosure of the SWNTs by the polymer, which endures environmental changes. In addition, polymers promote the biocompatibility of SWNTs by shielding their backbones [139], [140], [141], [142]. We hypothesized that the functionalization of SWNTs with dendronized perylenes on alkylated polymers would result in water-soluble, individualized, and biocompatible SWNT complexes applicable for bioimaging studies. Benefiting from the high brightness of ionically charged systems, we sought to improve the QYs of perylene by introducing charged groups on the dendritic head groups. The combination of perylene fluorophores emitting in the visible range and intrinsically fluorescent SWNTs emitting in the NIR creates a dual fluorescent system, which allows the imaging in the 1st and 2nd optical transparency window of tissue. In the following, we employed polymer-functionalized SWNTs with bright perylene fluorophores as cytocompatible SWNT complexes for potential bioimaging applications. Each component of the $P_{perylene}$-P_{alkyl}-SWNT complex system fulfils a certain purpose: i) the alkyl chains of the polymer ensure hydrophobic interactions with the SWNT scaffold, ii) the cytocompatible polymer solubilizes and coats the toxic tubes, iii) the dendron introduces hydrophilicity and prevents dye quenching, iv) the perylene serve as a fluorescent label, and v) the SWNTs are the basic immobilization scaffold.

6.3.1 Toxicity

To investigate whether polymer wrapping promotes the cytocompatibility of our SWNT complexes, we performed a toxicity study with the HeLa cell line. The viability of HeLa cells treated with the free dyes, polymers, SWNT complexes, and pristine SWNTs was monitored after an incubation time of 24h as depicted in the different sections of Figure 6.5 a). The results demonstrate high cell viability of the free dyes, polymers and functionalized SWNTs with viability rates around 100% proving no cytotoxicity effects of the compounds at the tested concentration. The advantageous application of our polymers towards commercially available surfactants is demonstrated in the surfactant section (yellow). As comparative surfactants, non-ionic polyether block copolymer Pluronic and ionic alkyl sulfate SDS were chosen. While our polymer-solubilized SWNTs were able to increase the cell viability of pristine SWNTs from 66% to $\geq$ 98%, surfactant-solubilized SWNTs decreased their viability to $\leq$ 20% . The cellular

degradation triggered by surfactant solubilization of the SWNTs can additionally be seen in Figure 6.5 b). While cells treated with P_{alkyl}-solubilized SWNTs show good viability, cells treated with SDS-solubilized SWNTs have a high rate of mortality even up to the extinction of the entire cell population[4].

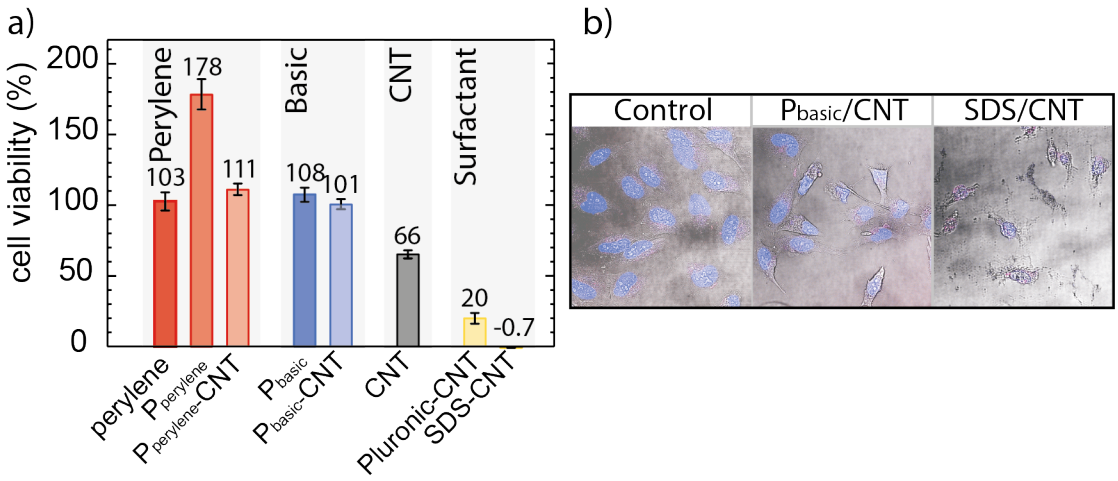

Fig. 6.5: a) Cytotoxicity study of HeLa cells incubated with the free perylene, the $P_{perylene}$ ($c_{dye}=1\,\mu M$),P_{alkyl} ($c_{polymer}=0.13\,\mu M$), and $P_{perylene}$-P_{alkyl}-SWNT complex ($c_{SWNT}=0.01\,g\,L^{-1}$). For comparison, HeLa cells were further incubated with pristine SWNTs or surfactant-solubilized SWNTs ($c_{surf}=1wt\%$). The values obtained were normalized to the non-treated cell population as control. b) Live-cell microscopy images of HeLa cells treated with P_{alkyl}-solubilized SWNTs and surfactant-solubilized SWNTs. The control represents the untreated cell population. Cell nuclei are shown in blue. Scale bar: 50 μm. The study shows good viability with our SWNT complexes and a low viability up to cell death with surfactant-treated SWNTs.

6.3.2 Microscopy and Flow Cytometry

To assess the biocompatibility of our non-covalently polymer functionalized SWNTs, in vitro uptake were performed on human epithelial HeLa cells [143]. The cellular uptake of the free dyes, polymers, and polymer-wrapped SWNTs was qualitatively monitored by live-cell confocal microscopy[5] and quantitatively analysed by flow cytometry as shown in Figure 6.6. After an incubation time of 4 hours, the free perylene-dyes showed no staining of HeLa cells. In contrast, the $P_{perylene}$ showed a vesicular uptake pattern after internalization into the cell's cytoplasm. The vesicular staining pattern presumably stems from cytoplasmic inclusions of the $P_{perylene}$ or $P_{perylene}$ functionalized SWNTs inside lysosomes and endosomes most likely by endocytosis. The study proves that a covalent binding between the dye and polymer backbone is essential to maintain the fluorescence of perylene after cellular uptake.

This observation was further proven by the fact that neither the free dye nor the free dye mixed with alkyl polymer showed a fluorescence signal after incubation. The protecting effect caused

[4]The toxicity tests were performed by Katharina Achazi.
[5]The live-cell confocal microscopy imaging and flow cytometry were performed by Katharina Achazi.

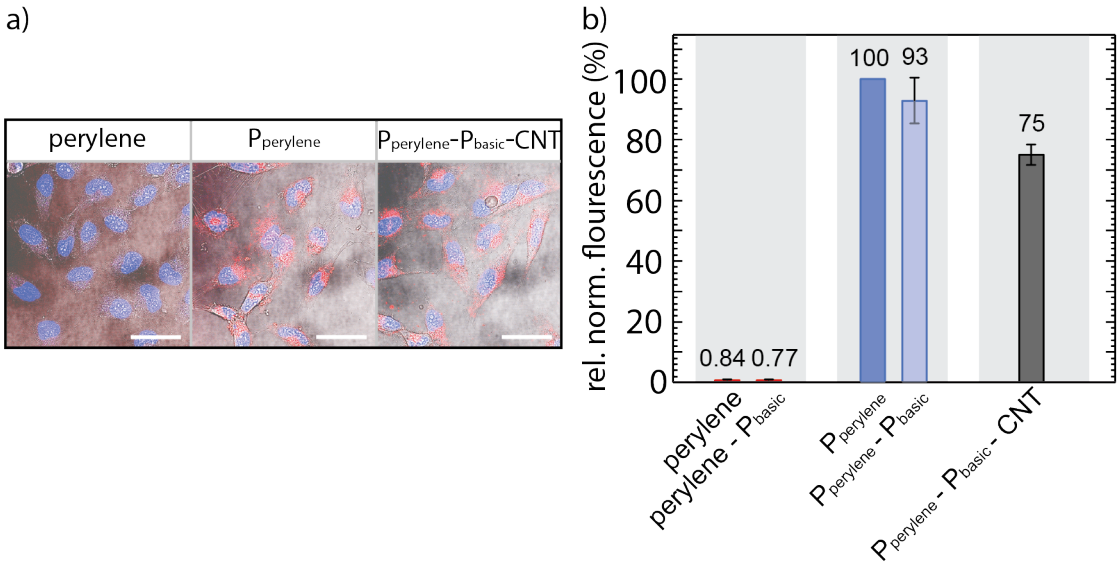

Fig. 6.6: a) Live-cell microscopy images of HeLa cells treated with perylene-based compounds (red) after 4 h of incubation. Cell nuclei are shown in blue. Scale bar: 50 μm. b) Flow cytometry analysis of HeLa cells treated with indicated compounds. The results prove an improved uptake behaviour and staining efficiency of the polymer and complexes.

by covalent dye-conjugation of the polymer not only allows for bright intracellular signals of $P_{perylene}$, but also bright intracellular signals of $P_{perylene}$ functionalized SWNTs. Thus, the conjugation of perylene efficiently prevents intermolecular π-π-stacking of the fluorophores among each other or to the SWNT scaffold and therefore enables an application of perylene as staining agent. The brighter fluorescence signal steams from an improved sterical shielding caused by the ionic sulfate groups, which prevent dye-dye or dye-polymer self-quenching. Flow cytometry analysis confirmed the trend seen in the microscopy study with low intracellular fluorescence intensities of free dyes and high intensities for the $P_{perylene}$, $P_{perylene}$-P_{alkyl} and $P_{perylene}$-P_{alkyl}-SWNT sample (Figure 6.6 b).

6.3.3 Photoluminescence and Raman Imaging of the Hybrid inside the HeLa Cells

As the polymer wrapping ensures the strong immobilization of the perylene on the SWNTs, we assumed that an intracellular signal of the $P_{perylene}$ simultaneously indicates the cellular uptake of the SWNTs. However, the size of single pristine SWNTs is below the resolution limit of the optical microscope. Additionally, the intrinsic fluorescence of debundled SWNTs above 900 nm is out of detection range of the used confocal microscope (400 to 800 nm). Thus, confocal microscopy solely ensures the uptake of the perylene-moiety by monitoring the perylene fluorescence. To affirm the cellular uptake of the entire multifunctional polymer SWNT hybrid, we resorted to Raman spectroscopy. It was previously reported that the cellular uptake of functionalized graphene sheets can be monitored via Raman microscopy [144].

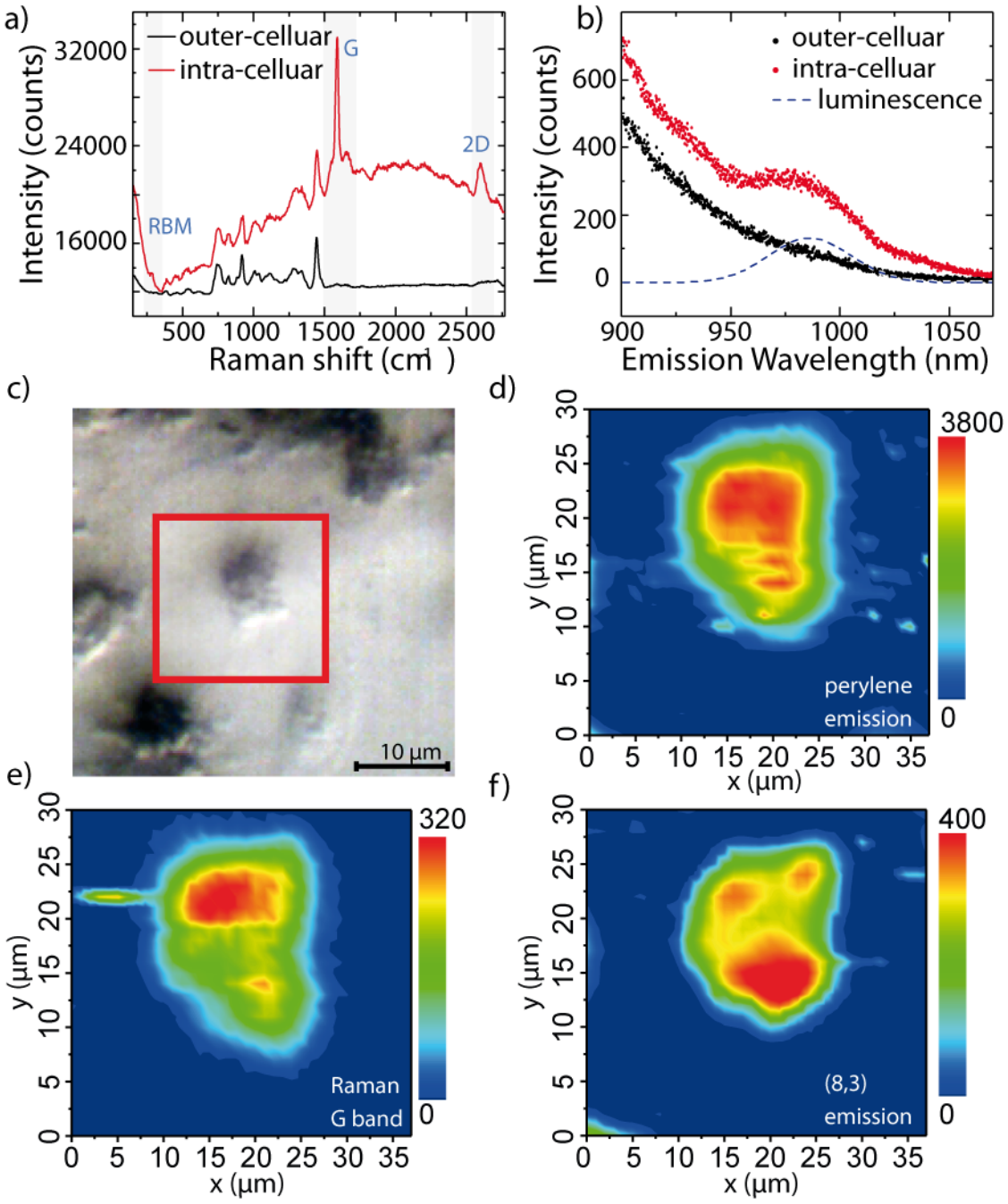

Fig. 6.7: a) Raman spectra of the $P_{perylene}$-P_{alkyl}-SWNT sample at 1.9 eV inside and outside the HeLa cell incubated. The RBM, G, and 2D bands are only visible inside the cell clearly indicating the penetration of the SWNTs into the cells. b) SWNT Photoluminescence at 1.9 eV inside and outside the HeLa cell. Again, the signal is only visible inside the cell indicating successful cellular uptake. c) Optical image of HeLa cells incubated with sulfated complex $P_{perylene}$-P_{alkyl}-SWNT. The red frame shows the area in which PL and Raman measurements were conducted. d) Spacial PL map of the perylene' emission excited at 532 nm. e) Spacial distribution of the SWNTs' Raman G band excited at 638 nm. f) Spatial PL map of the (8,3) tubes' emission excited at 650 nm. The intracellular emission signal of the SWNTs strongly resembles the shape of the investigated HeLa cell, thus, indicating a successful internalization of the entire polymer-SWNT complex into the cell.

Inspired by this approach, we employed Raman spectroscopy combined with PL measurements to verify the cellular uptake of the perylene-covered SWNTs. For that purpose, several cells were incubated with $P_{perylene}$-P_{alkyl} SWNT hybrids and scanned with an optical microscope. Figure 6.7 c) depicts a set of cells with a 10 times amplification. The red frame highlights the area in which the photoluminescence and Raman signals of the selected cell were taken. To ensure whether the polymer is still bound to the SWNTs after the cellular internalization, Raman spectroscopy of the SWNTs was performed. We located the SWNTs' Raman signals using the lower excitation energy line (1.9 eV). We compared Raman spectra inside and outside the cell as seen in Fig. 6.7 a). The three major carbon nanotubes Raman modes (RBM, G, 2D) are only present inside the cells, indicating the cellular uptake of the SWNTs (Fig. 6.7 a).
In Figure 6.7 e) the spatial distribution of the Raman G band of the nanotubes inside and outside the cell is depicted and exactly resembles the cells shape. Despite the low PL quantum yield of SWNTs, we were further able to demonstrate the uptake of the functionalized SWNTs by direct monitoring of the PL signal of the (8,3) tube species. The PL signal was obtained by also exciting the tubes at 1.9 eV (E_{22}) and monitoring at 1.3 eV (E_{11}). The PL signal of the tubes could only be observed inside the cells as seen in Fig. 6.7 b). Again, we established the spatially-resolved map of the intensity of the tubes' emission signal depicted in Figure 6.7 f). The spatial distribution of the nanotube emission strongly overlaps with the cell shape 6.7 c). As a reference and to verify the presence of the $P_{perylene}$ we also measured the emission of the perylene. For the excitation of the perylene-polymer the 532 nm laser line was used, to match the perylene $S_0 \longrightarrow S_0$ transition. At this excitation, two emission bands at 550 nm and 592 nm dominate the optical signal. In Figure 6.7 d) the intensity of the 592 nm band was plotted as a function of the spatial position. A strong signal from the area inside the cell could be detected indicating the successful transfer of the label polymer into the cell, which is consistent with the results reported for the cell imaging[6]. The high image contrast confirms the efficient uptake of the functionalized SWNTs inside the living cell. The spatially-resolved PL signal of the perylene and SWNTs and the Raman signal of the SWNTs, strongly resemble the shape of the cell acquired in the microscope image. The overlapping of the $P_{perylene}$ PL and the SWNTs' Raman signals indicate that the perylene-SWNT hybrid platform remains unperturbed after uptake process. These results prove three major findings, i) the successful cellular uptake of the perylene-SWNT hybrid complex, ii) the stability of the platform ensured by the strong wrapping of the polymer around the SWNTs, and iii) the direct monitoring of the cellular uptake through several independent system parameters, which demonstrates the versatility of the perylene-polymer SWNT complex.

We developed a multifunctional polymer-SWNT complex and probed their performance as bioimaging agents. The rationally designed complex consists of dendronized perylene as fluorescent labels, long alkyl chains as hydrophobic units, a polymer backbone as solubilizing and shielding moiety, and SWNTs as general immobilization platform. The optical characterization of the complexes revealed moderate QYs of 5.1% for the sulfated SWNT complexes. The hybrid

[6]The Raman and PL measurements of the Hela cells with incubated SWNTs were performed by Georgy Gordeev.

system did not show energy transfer processes suggesting a preserved perylene luminescence after complex formation. The biological suitability of the complexes was analysed by toxicity and uptake in vitro studies on HeLa cells. The cytotoxicity study displayed the superior compatibility of the polymer-wrapped SWNTs compared to pristine or surfactant-solubilized SWNTs; the cellular uptake study revealed the internalization of the entire intact polymer-SWNT complex via the perylene and SWNT emission. We demonstrated that the functionalization of SWNTs with perylene-conjugated polymers results in water-soluble, fluorescent, and debundled SWNT complexes suitable for bioimaging studies. Our supramolecular complex allowed for the direct imaging of the SWNTs' cellular uptake and drastically improved their cytocompatibility.

The combination of perylene fluorophores and intrinsically fluorescent SWNTs allowed the intracellular detection of the complexes in the 1st and 2nd optical transparency window of tissue. The development of such a dual imaging system is non-trivial since transfer processes between the fluorophores and SWNTs can cause the luminescence quenching of the dyes. These results render the sulfated multifunctional SWNT complexes as potent candidates in fluorescent bioimaging for a broad readout in two optical windows. The versatile modification routine for the formation of SWNT complexes with multipurpose functionalities may, furthermore, be of great benefit for sophisticated biomedical applications in the future.

6.4 Covalent Functionalization

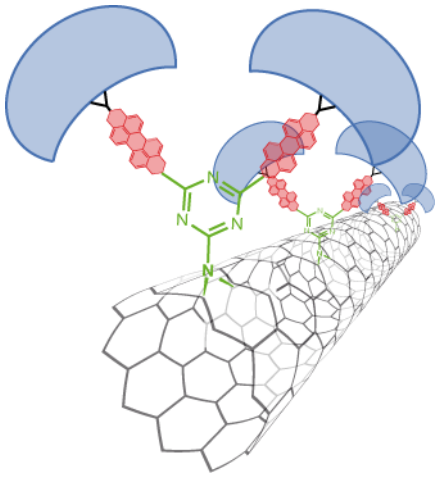

Fig. 6.8: Covalent attachment of perylene via the nitrine based [2+1] cycloaddition.

Even though the polymer wrapping produced stable perylene-nanotube the almost orthogonal relative orientation between the dyze and tubes made the Förster process very inefficient. To improve the efficiency of the progress we tested an alternative configuration. Accordingly, we synthesized perylene-SWNT hybrids with the [2+1] cycloaddition and investigated the influence of perylene on the optical properties of the SWNTs. Prior to the SWNT-functionalization hydroxylated dendronized free dyes bearing a hexyl liner with an monofunctional azide group (HO-[G3]-PBI-hexyl-N3) were prepared according to the procedure introduced in Ref. [10]. Triazine-functionalized SWNT (SWNT-Trz) were synthesized by the reaction of SWNTs with 2-azido-4,6-dichloro-1,3,5-triazine as reported in Ch. 4 and Ref. [8]. Propargylation of the triazines' chlorine atomes by nucleophilic substitution gave intermediate SWNT-propargyl [145] which was subsequently click coupled [146], [147] with the azide-carrying perylene dye to yield the final

water-dispersible covalently dye-conjugated SWNTs (HO-[G3]-PBI-hexyl-triazole-SWNT)[7]. XPS measurement were performed to prove the successful attachment of the perylene onto the SWNTs sidewalls. The spectra showed a change in composition during the different reaction steps, the pristine, triazine functionalized, and the tubes with attached perylene. All three sample show the C1s carbon spectra arising from the SWNT backbone. The SWNT-Trz shows an additional nitrogen and chlorine peak and SWNT-Trz-perylene show a further oxygen peak, which indicates the successful immobilization of triazine and perylene. Monitoring the C1s peak confirms the successful functionalization even more. The sp^2 peaks show a gradual shift during the different reaction steps towards higher binding energies, similar as reported in Sect. 4.4. In the SWNT-Trz sample the onset of a C-O/C-N peak can be observed. Those peaks are even more dominant in the SWNT-Trz-perylene sample. Those results prove the succesful functionalization of the perylene onto the SWNTs. From the given XPS results an overall perylene coverage of 12% could be calculated[8].

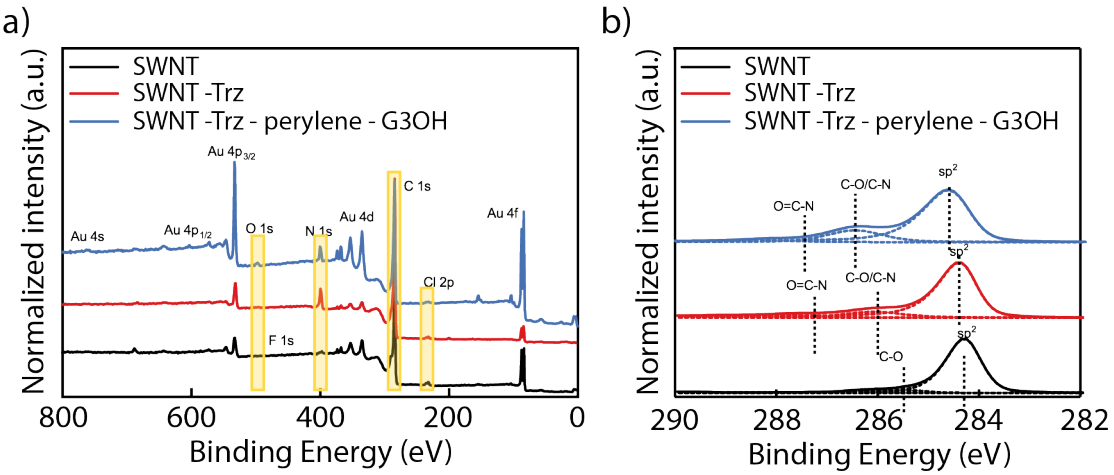

Fig. 6.9: a) XPS overview of the pristine, triazine functionalized, and perylene functionalized nanotube samples b) Highly resolved C1s spectra of the different components.

6.4.1 Photoluminescence Excitation

Proven the succesfull functionalization of perylene on the SWNTs, I conducted PLE measurements to investigate influence of the perylene on the optical properties of the SWNTS. To perfom PLE measurements of the perylene and triazine functionalized SWNTs both samples were debundled using the surfactant Sodiumtaurodeoxycholate (NaDOC). 1wt% NaDOC was added to a 0.1 g/L SWNTs solution. The mixture was sonicated at 20 W for 1 h. Afterwards PLE measurements were performed to characterize the sample. Figure 6.10 displays the PLE map of the two components, triazine and perylene functionalized SWNTs, respectively. In both samples the (6,5), (8,4), (7,5),(7,6), and (8,3) tubes can be observed. The presence of the

[7] A manuscript describing the full synthesis as well as the following results is currently in preparation.
[8] The XPS measurements were performed by Ivgen Donskyi and only a short summary is illustrated here. A full XPS description will be part of the manuscript which is in preparation.

tubes' emission shows the successful debundeling of the tubes, and further that the emission was preserved after the functionalization. The peaks above the grey line originate from the direct emission of the SWNTs. In the perylene-SWNTs sample an additional signal can be observed in the lower excitation range, see Fig. 6.10. The perylene functionalized tubes show a signal around the excitation range between 480 nm to 495 nm with an emission signal around 950 nm to 1000 nm. The excitation region overlaps with the excitation region of the perylene. The emission range of the signal corresponds to the emission wavelength of the (6,5) tubes and indicates indirect emission of the (6,5) tubes through the perylene. The presence of only one distinct perylene mediated emission strongly indicates a Förster resonant energy transfer. Thus, I evaluated the observed energy transfer according to the formula introduced in Sect. 6.1.1. I will calculate the Förster radius for the given system and compare the expected energy transfer efficiency with the experimentally observed one and deduct the expected intensity of the perylene mediated emission of the tubes.

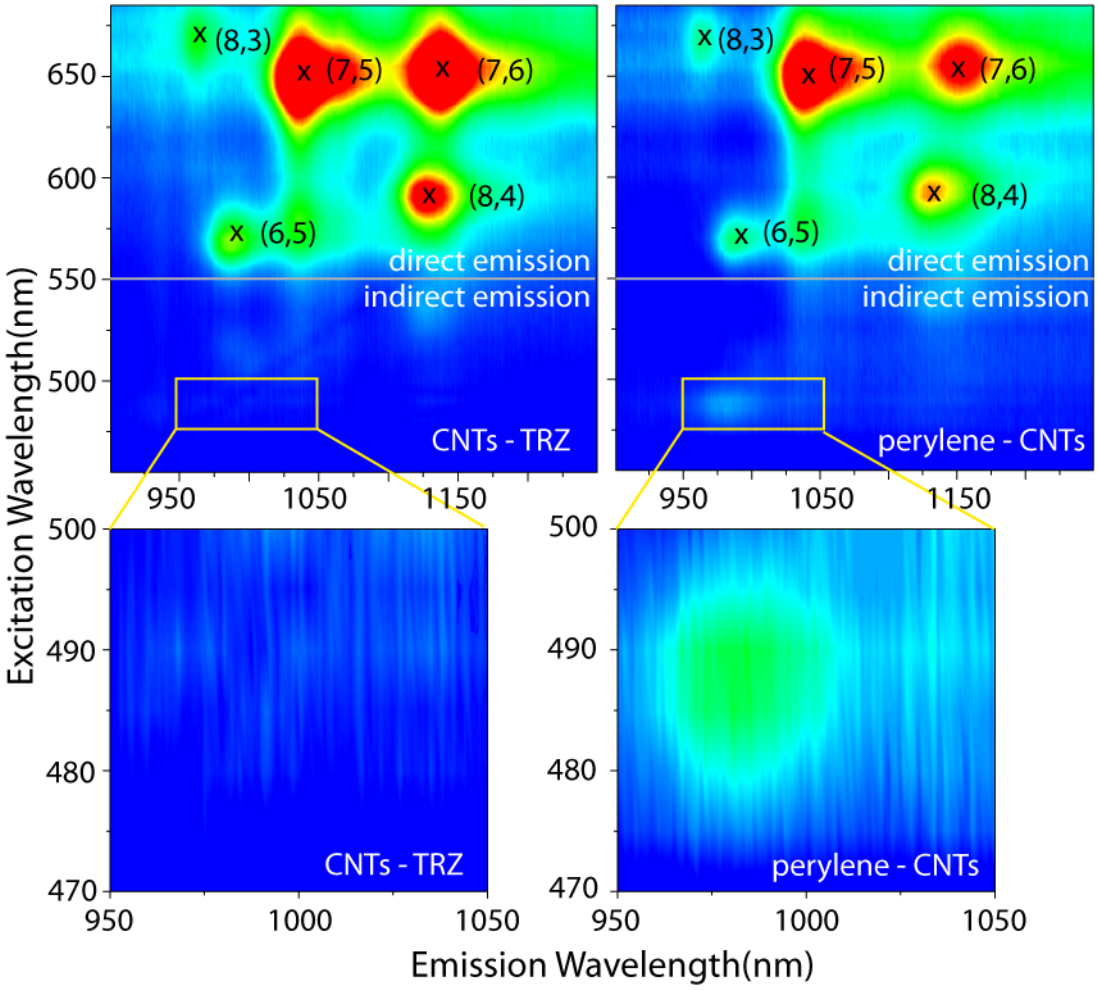

Fig. 6.10: 2D PLE map of the a) triazine functionalized SWNTs and b) the perylene functionalized tubes. An additional peak in the 450-500 nm region can be observed in the perylene functionalized sample. The enlarged excerpt shows that this peak is not present in the triazine samples and clearly indicates energy transfer in the perylene sample.

6.4.2 Energy Transfer Efficiency

To obtain the energy transfer efficiency, the Förster radius needs be quantified according to Eq. 6.1. The normalized fluorescence spectrum of the donor was calculated using the 490 nm excitation line of the perylene spectrum. ϵ_A is given by A/cL, where A is the absorption of the (6,5) tubes taken the UV-Vis measurements and c the SWNTS concentration[9] ($3.8 \cdot 10^{-6} mol/L$) and L the length of the optical path. The quantum efficiency of 0.34 for the perylene derivative was determined by Katharina Huth.

κ^2 was calculated according to Eq. 6.2. Figure 6.11 displays the orientation of the SWNTs and the perylene indicating the corresponding angles. Knowing all those parameter the Förster radius can be calculated, resulting in a value of 1.62 nm. To obtain the expected transfer efficiency the actual distance between the perylene and SWNTs needs to be determined. The distance according to the different orientation of the perylene to the SWNTs a mean distance of 1.58 nm was (see the Appendix).

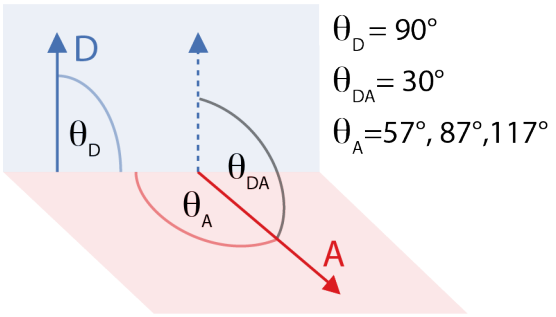

Fig. 6.11: Orientation of the vibrational plane between the SWNTs and perylene for the three potential allignments.

With those two values the theoretical expected ETE of the system can be calculated according to Eq. 6.3, yielding a value[10] of $\Phi_T = 0.54$. The PLE measurements of the perylene before and after attachment onto the SWNTs reveals the actual experimental observed transfer efficiency Φ_{Ex}. Figure 6.12 displays the emission of the free perylene and the perylene attached onto the SWNTs. The emission of the perylene is roughly quenched by a factor of 6. The experimentally observed ETE thus yields, according to Eq. 6.4, an value of $\Phi_{Ex} = 0.82$. The experimental and theoretical values show a slight deviation. The variation could stem from the estimated SWNT concentration and the approximation of the perylene distance, both are strongly affecting Φ_T. Furthermore, the SWNT-perylene sample could also inherit a certain fraction of free perylene which non-covalent sticks onto the SWNTs sidewalls[11]. This could increase the actual coverage of perylene on the tubes and was not accounted in pure perylene sample when preparing the free perylene sample used for Φ_{Ex}. This would lead to less quenching of the perylene and a lower energy transfer efficiency.

[9] The SWNTs concentration was calculated according to Ref. [148]. With a mean diameter of 0.78 nm and a mean length of 1000 nm and with 41% of (6,5) tubes present in the ComoCats (6,5) batch. For a full calculation see the Appendix.

[10] $\Phi_T = \frac{1}{1+(r/R_0)^6} = \frac{1}{1+(1.58/1.62)^6} = 0.54$

[11] Post-synthesis the samples underwent several washing cycles to ensure removal of access of unbound perylene. However, a residue of unbound perylene cannot be excluded.

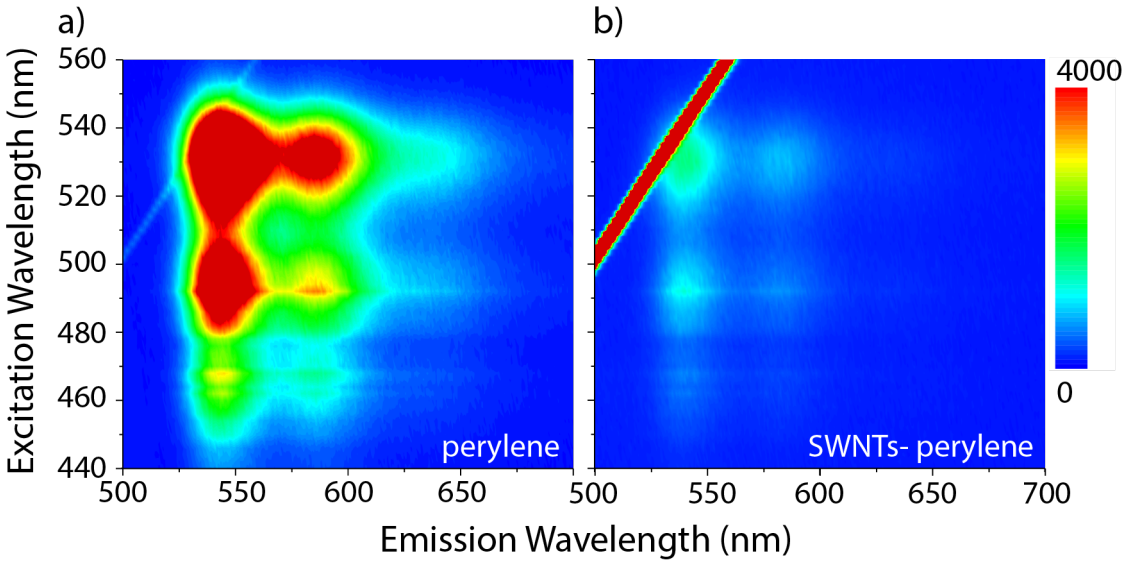

Fig. 6.12: 2D PLE map of a) free perylene and b) perylene covalently attached to the SWNTs. The perylene covalently attached to the tubes shows a strong quenching of the perylene emission.

Lastly, we can compare the magnitude of the expected indirect emission η_T of the (6,5) tube with the actual experimental observed one given by Eq. 6.5 and Eq. 6.6. The experimental observed ratio can be obtained from comparing $I_{transfer}$ the fluorescence intensity of the indirect SWNTs emission and $I_{(6,5)}$ of the direct (6,5) emission, accounting η_{ex}=0.5. The η_T can be calculated with the theoretical ETE and the coverage of the SWNTs which yields a values of 0.65. Given the different estimations in the theoretical calculation, both values are comparable. The perylene functionalized tubes via [2+1] cycloaddition yielded hybrids which showed indirect perylene mediated emission of the (6,5) tube. The observed energy transfer in the covalent perylene functionalized is lower compared to the one observed by Ernst *et al.* or Roquelet *et al.* The main reason is the bigger perylene dye distance as well as the orientation of the perylene in respect to the tubes. Ernst *et al.* achieved a system with a parallel alignment between the two dipoles, where as our system exhibits a misalignment of ~ 30 degrees. The distance of the perylene was approximated to the perylene centre, as the perylene is not aligned parallel to the tubes. The actual position to the tubes surface could further differ due to the flexible linker between the triazine and perylene. Both aspects lead to a decrease in energy transfer efficiencies.

The other main difference to the experimental observationd by Ernst *et al.* is the observation of only one distinct indirect emission peak corresponding to the (6,5), as seen in Fig. 6.13. This indicates the pure nature of a Förster resonant energy transfer process and is consistent with the dependence on the spectral overlap of the donor and acceptor. Figure 6.13 shows the spectral overlap for the (6,5), (7,5) and (9,4) nanotube also present in the investigated sample. We can see that for tubes with higher excitation energy the spectral overlaps decreases. This inevitable reduces the Förster radius and hence the energy transfer efficiency. The strongest overlap can be seen for the (6,5) tube, which resembles the experimental observed indirect emission of the (6,5) tube, explaining why we only could observe indirect emission of the (6,5) tube.

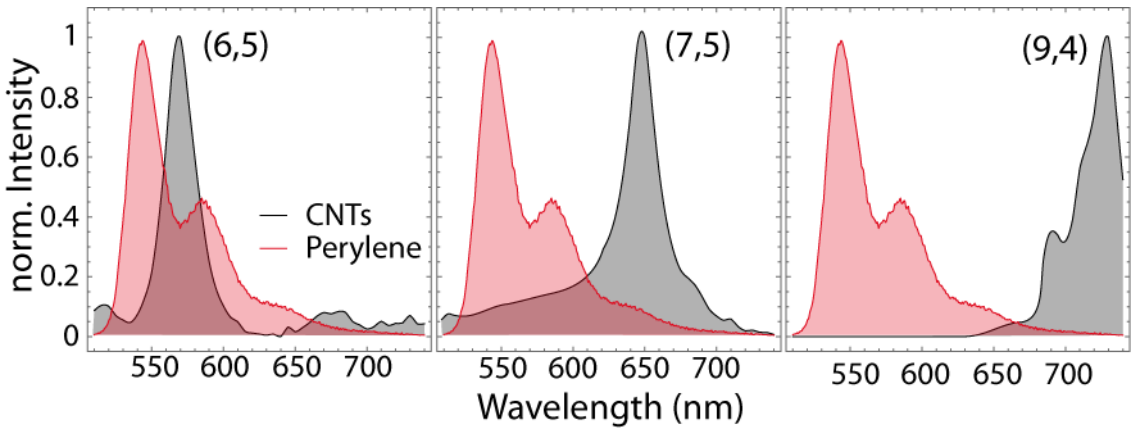

Fig. 6.13: Spectral overlap between the donor emission (in red) and acceptor absorption(in black). For the (6,5) tube a clear spectral overlap can be seen between the perylene emission and the tubes excitation. For the (7,5) and (9,4) the spectral overlap decreases as the excitation wavelength of the tubes increases.

The covalent perylene functionalized tubes showed Förster resonant energy transfer. An indirect perylene mediated emission of the (6,5) tubes could be observed. Compared to other SWNT dye systems the ETE is rather low. Unfortunately, does the given nature of our system limit the ETE and we can not expect a higher indirect emission of the tubes. The covalent perylene functionalization of SWNTs through the [2+1] cycloaddition is promising, however, is it currently limited by its given morphology. In order to improve the system a higher perylene coverage, a smaller tube-dye distance, and a more parallel alignment of the perylene to the SWNT dipole needs to be aspired.

6.5 Comparison

In this chapter I discussed two different functionalization methods for the immobilization of perylene on the SWNTs sidewall. In the first part perylene was incorporated into a polymer, allowing a uniform and tight attachment of the perylene. I monitored the solubilization ability of the polymer and tube-dye interaction. The perylene-polymer was used at concentration in the range of 10^{-6} to 10^{-4} μM. The polymer concentration here was too low to successfully debundle the SWNTS. The addition of basic polymer produced well isolated tubes as proven by the PLE measurements, showing the distinct PLE peaks of 12 different nanotube species. After the addition of basic polymer also the restoring of the perylene emission was observed, indicating a shielding effect between SWNTs and perylene. From the observed perylene quenching a ETE of 0.5 could be calculated. With a coverage of 2% an indirect tube emission of 10% of the direct emission could be expected but was not observed in the PLE measurements. The aimed energy transfer was not observed. Both, the ETE and expected indirect emission are rather low compared to other energy transfer system which makes the setup of polymer wrapped SWNTs rather unfavouring for energy transfer studies. Given the failure of the energy transfer we resorted to another application of the produced hybrids. Perylene is a common fluorescent

label used for bioimaging applications. We incubated the hybrid system into HeLa cells and performed cell imaging, flow cytometry, Raman and PL measurements inside the cell as well as toxcicity test. The perylene-polymer-SWNTs hybrids enabled direct imaging of both the SWNTs ans perylene inside the cells and showed a drastical improvement the biocompatibility of SWNTs. These results render the multifunctional SWNT hybrids as potent candidates for fluorescent imaging in the 1st and 2nd optical transparency window of tissue. In the future, the versatile monomers of the polymer could be further exploited to incorporate receptor for cell binding. The hollow structure of the SWNTs could encapsulated drug, enabling targeted and monitored drug release through the sophisticated SWNT hybrid.

In the second approach, the new introduced [2+1] cyclo addition reaction was used for the perylene immobilization. The synthesized SWNT-perylene compounds were debundled with the help of surfactants. The PLE maps showed luminescence of the tubes and revealed energy transfer. Indirect, perylene mediated excitation of the (6,5) tube could be observed. With the given structure of the system, I calculated the Förster radius and obtained the expected ETE. The experimental observed ETE was gained from the quenching magnitude of the perylene in presence of the SWNTs. Both values were in good agreement, considering the possible derivations due to the estimation of the tube-dye distance and the SWNT concentration. Furthermore, showed the system a clear FRET, only the tube (6,5) with the strongest spectral overlap of the perylene emission and the tube absorption showed energy transfer. The [2+1] cycloaddition proved to be successful in allowing energy transfer system. The setting of the system, however, proved to be less efficient than the surfactant or micelle swelling approach. An optimization of the perylene coverage as well as the dipole orientation could lead to an increase of the ETE and would be beneficial, as the covalent functionalization is more robust compared to the surfactant and micelle swelling approach.

7

Plasmonics

In the last chapter I highlighted the versatile utilization of SWNTs for biomedical applications. I showed that the decoration of SWNTs with dyes created bright fluorescent markers for cell imaging. Their NIR emission makes SWNTs themself attractive for biological imaging, as biological tissue is transparent in two ranges between 650 and 1350 nm. The first optical window is located between 650 nm and 950 nm [122]. This region, however, is disguised by the autofluorescence of the tissue. The second optical window from 1000-1350 nm shows a better signal to noise ratio, making it preferable for cell detection. The second transparent window coincides with the emission range of SWNTs making them potential bioimaging agents [122]. Welsher *et al.* performed different bioimaging experiments, demonstrating the successful binding of SWNTs to specific cells and the visualization of the targeted region through the excitation of the SWNTs [7], [149],[150].

One of the major drawbacks of SWNTs is their low quantum yield compared to other biocompatible fluorophores, which has hampered them from extensive utilization [51], [151], [152], [153]. Several approaches have been made to overcome this obstacle: For example SWNTs were placed into cavities, giving a 30-fold enhancement of their emission [154]. Inserting them into photonic crystals resulted in an enhancement factor of 50 [155]. Such experimental configurations demonstrated enhancement of the luminescence and allowed fundamental studies, however, those systems lacked integrability with real applications. The enhancement only occurred as long as SWNTs were placed in the special environment. The setups were macroscopic in scale; they cannot be exploited for the implementation into biological systems. A more flexible route involves the attachment of fluorophores onto colloidal metallic nanoparticles [156]. This concept led to a 40-fold enhancement of the fluorophore IR800 attached to gold nanoshells [157]. The interaction of metals with fluorophores and its effect on the radiative process was subject of interest already in the 1970s when Drexhage *et al.* analysed the influence of a metal interface on fluorophores. These investigations showed that the presence of a metal tremendously influences the lifetime and emission intensity of the fluorophore [158]. Hong *et al.* exploited this mechanism for SWNTs by placing them onto rough gold surfaces. They observed enhancement of the tubes luminescence by a factor of 10 [159]. This configuration, anyway, still lacked the scalability to nanoscale dimension. To possibly combine both aspects one can decorate SWNTs with metallic nanoparticle for achieving enhanced emission. A first proof of principal was reported in our publication [11]. I was able to create gold nanoparticle-SWNT hybrids with enhanced luminescence, the π-hybrids.

In this chapter I concentrate on the approach to create SWNT-gold hybrids through the non-covalent micelle swelling technique. To further improve the hybrids and understand the underlying physical mechanisms, I observed the influence of the stirring time [12], conducted a resonance study by tuning the plasmon resonance of the attached particles, and analysed the lifetimes of the hybrids [13]. I will show results of first SWNT-gold nanoparticle hybrids built up via the covalent [2+1] cycloaddition [8]. I will start this chapter with a short introduction into the basic concepts on plasmonic and metal enhanced fluorescence. This chapter is based the following publications: [12], [13], [8], and [11]. Most of the parts are directly copied from the article and have been slightly adjusted.

7.1 Plasmonic Enhanced Fluorescence

Materials in the nanoscale exhibit extraordinary properties. In particularly metals show drastic changes in the nanoscale, novel physical and chemical properties arise compared to the macro scale. Metallic nanoparticles (MNP) exhibit bright colours ranging from yellow to green to red and purple and even intense blue. This phenomenon was already exploited in ancient Roman times, where metallic nanoparticles were used to stain glass. A famous example is the Lycurgus cup, see Figure 7.1 a). Another extensive use of MNPs was the staining of church windows, Figure 7.1 b). When irradiated with light, such glasses reveal outstanding colours according to the kind and shape of metal nanoparticle incorporated (Fig. 7.1 c).
Those optical characteristics arise from surface plasmons. Plasmons are coherent oscillations of the electron cloud initiated through irradiation with light. The incoming light induces a displacements of the electron cloud with respect to the lattice nuclei. The conducting electrons will experience a restoring force towards the nuclei leading to oscillations of the cloud, sketched in Figure 7.1 d). The frequency of the oscillations is governed by the electron density and mass, the kind of metal, and the shape and size of the particle. For a spherical MNP, only one surface plasmon resonance is observed. The electrons are displaced into all directions but due to their symmetry it resembles only one polarization direction and thus one plasmon band. A gold nanorod (AuNR), on the other side, has two symmetry axis, a longitudinal and transversal, thus showing two modes (see Fig. 7.1 e). The resulting electromagnetic waves are in the visible range explaining the intense staining of the metallic nanoparticles.
Another interesting phenomenon of nanosized metals is their ability to strongly enhance and localize electromagnetic (EM) fields. The ratio between their extinction and physical cross section indicates the ability of the particles to localize the electric field in their proximity. If the ratio extends beyond unity they can strongly concentrate the EM field in their close surrounding. For metallic nanoparticles the ratio between extinction and physical cross section surpasses the value of one leading to an overall enhanced EM field [160]. Sharp tips or ends promote the enhancement even more as the electrons agglomerate stronger at those sides leading to the so called lightning rod effect. A fluorophore placed in the close vicinity of a nanoparticle experiences the enhanced electric field, strongly influencing its physical response. The metal

enhanced fluorescence (MEF) can occur through two different processes: (i) Non-radiative coupling between the surface plasmon resonances (SPR) of the nanoparticle and the excited state of the fluorophore, which results in excitation of the SPR and (ii) enhanced absorption of the light by fluorophores due to the enhanced electric field around the nanoparticle.

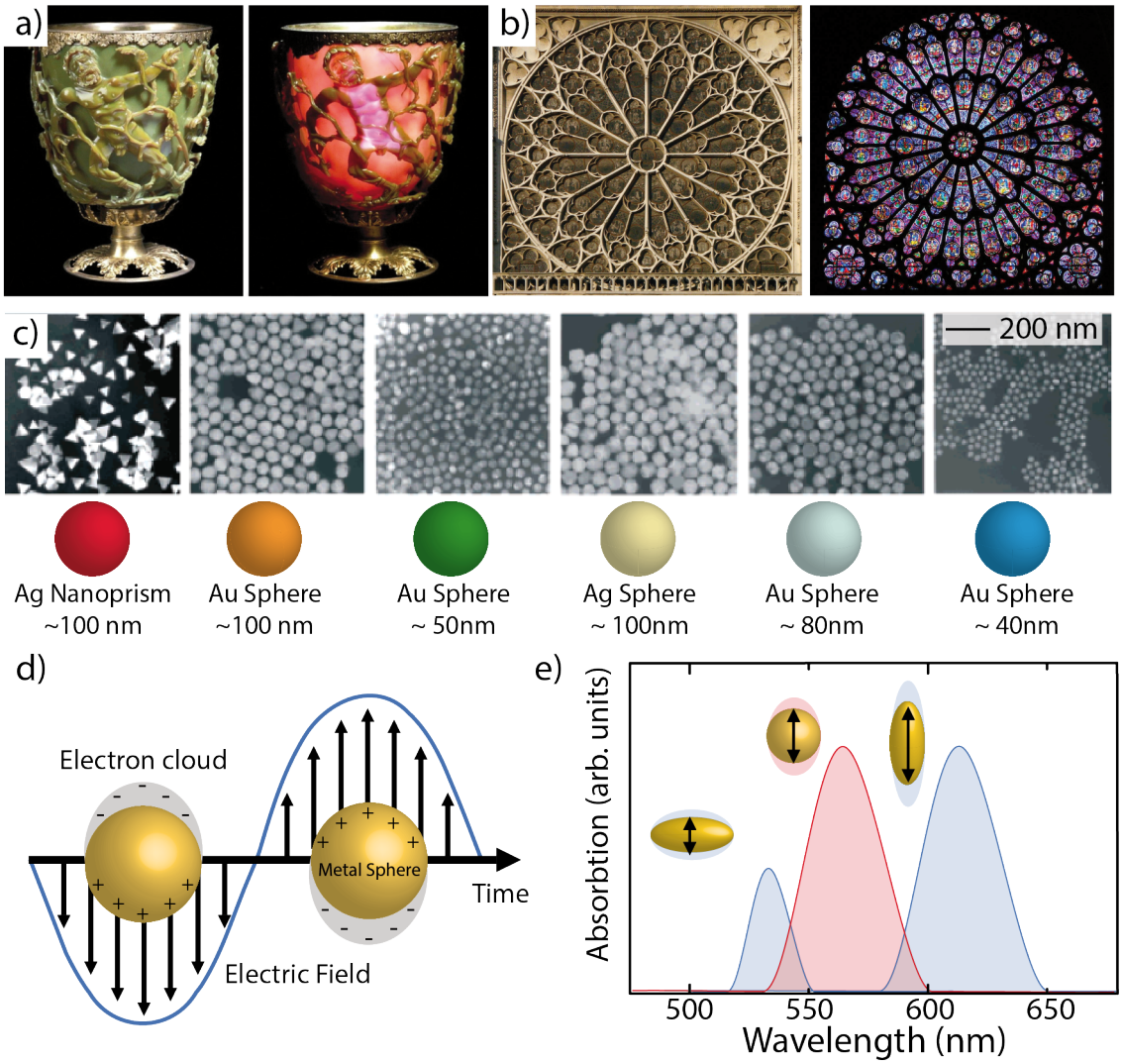

Fig. 7.1: a) Lycurgus cup without (left) and with (right) illumination [161]. One can clearly see that the incoming radiation is exciting the plasmons leading to the red staining of the cup. b) The North Rose of Notre Dame, a church window with embedded plasmonic metal particles. Without light illumination no staining of the glass can be observed (left). From the inside of the church the window reveals remarkable colour variations due to the illumination from outside (right) [162]. c) SEM image of different metallic nanoparticles with their corresponding staining as well as the used metal and morphology [163]. d) Electron cloud displacement of the metallic nanoparticle during light illumination [164]. e) Absorption spectra of the different gold nanoparticles. Different symmetries give rise to more absorption bands.

One important parameter governing the phenomenology of their interaction is the emitter-metal separation [159], [165]. Indeed, two different regions are formed around a nanometallic particle subjected to optical irradiation: the near- and the far-field region (highlighted as NF and FF in the sketch of Fig. 7.2 a). In the near-field region (typically extending few tens nanometers around the metallic surface) the evanescent wave strongly confined in space along

with an enhancement of its intensity. In the far-field region we find the propagating component of the electromagnetic radiation scattered from the metallic particle. An emitter placed in the position labelled as (NF) in Figure 7.2 will prominently sense the plasmonic near-field, whereas an emitter placed in position (FF) will mostly sense the propagating component of the electromagnetic radiation, which can destructively or constructively interfere with the radiation generated by the emitter, yielding a net quenching or enhancement of the emitter's yield. These interference effects, though, occur for separations of the order of the metal particle radius or even bigger [165]. While they give rise to the enhancement of the SWNTs observed emission [166], they are negligible for the AuNR-SWNTs separations of our π-hybrids in which MNPs and SWNTs are within the same micellar core and thus in very close proximity.

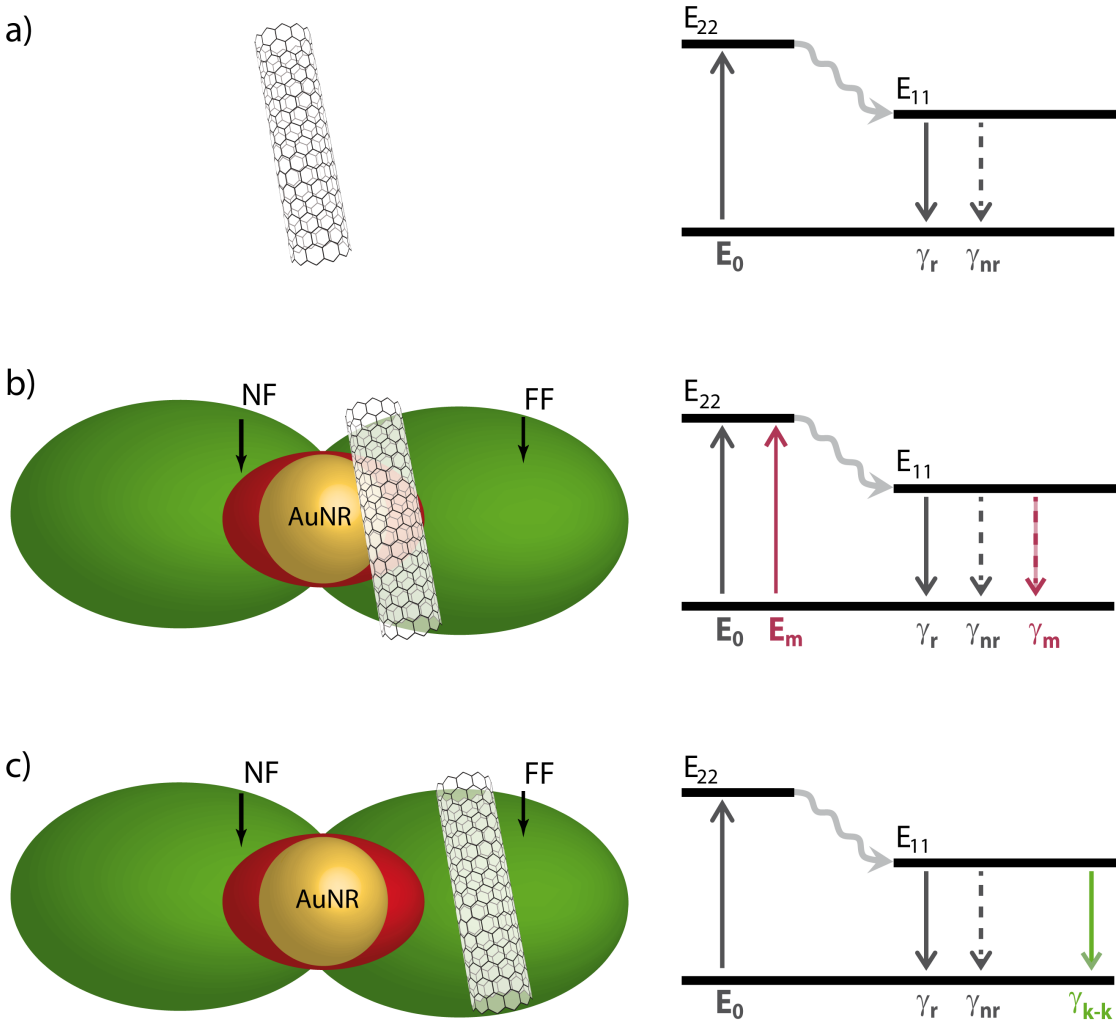

Fig. 7.2: a) Schematic depiction of the distribution of the electromagnetic field around a small metallic nanoparticle (AuNP). The localized near-field is highlighted in red while the scattered, propagating component is green. b) Beyond the intrinsic excitation (E_0) and de-excitation (γ_r and γ_{nr}) pathways, the AuNP introduces additional excitation (E_m) and de-excitation pathways (γ_m) due to the near-field interaction. c) Additional inferential terms (γ_{k-k}) are due to the interaction with the far-field.

Generally, it is possible to depict the properties of the optical process through a simple 3-level system (see Fig. 7.2 a). The system at equilibrium is in its ground state. Upon excitation, it will populate the level labelled as E_{22} for consistency with the standard nanotubes notation. From there, the system will undergo a fast non-radiative thermalization to the state labelled as E_{11}, from which it can de-excite both radiatively and non-radiatively. Please note that there could be additional states located between E_{11} and the ground state, causing additional de-excitation channels. They are taken in account by estimating the total lifetime of E_{11}. The balance between these processes can result in different phenomenologies, ranging from enhanced optical response to total quenching. For emitters with low quantum yield and under weak illumination, it has been shown that the emission is maximally enhanced by placing the emitter in the close proximity of the metallic surface [167], while competing quenching effects plays no significant role [168]. In such a lossy regime the enhancement factor Φ ascribed to proximity effects is determined by the balance between two contributions: the stronger pumping F_{exc} and the faster de-excitation F_{rad} [159], [165], [166] formalized by:

$$\Phi = F_{exc} \cdot F_{rad}. \tag{7.1}$$

Figure 7.2 b) provides a simplified sketch of the metal-induced changes in the optical process. The first term F_{exc} of Equation 7.1 takes into account the stronger pumping due to the locally enhanced plasmonic field in the proximity of the metallic surface for the transition from the ground state to E_{22} of Figure 7.2 b):

$$F_{exc} = |\frac{E_m(\pi)}{E_0}|^2, \tag{7.2}$$

whereas the second term F_{rad} takes into account the metal-induced change in the de-excitation lifetimes in the transition from E_{11} to the ground state depicted in Figure 7.2 b) [166]:

$$F_{exc} = |\frac{\tau_m}{\tau_0}|^2, \tag{7.3}$$

where $\tau_0 = 1/(\gamma_r + \gamma_{nr})$is the total lifetime of the emitter in the free space and $\tau_m = 1/(\gamma_r + \gamma_{nr} + \gamma_m)$ is the emitter lifetime in the presence of the metal. The black arrows in Figure 7.2 b) indicate the intrinsic processes of the free emitter: E_0 is the excitation rate while γ_r and γ_{nr} are, respectively, the radiative (continuous line) and non-radiative (dashed line) de-excitation rates. Once the emitter interacts with the metal, additional excitation (E_m) and de-excitation (γ_m) pathways arise. Note that we neglect the term labelled as γ_{k-k} in Figure 7.2 c), which accounts for the interference effects in the far-field region. Here we want to exploit the plasmonic near-field to enhance the optical properties of SWNTs and enhance their photoluminescence.

7.2 SWNT- Gold Nanoparticle Hybrids

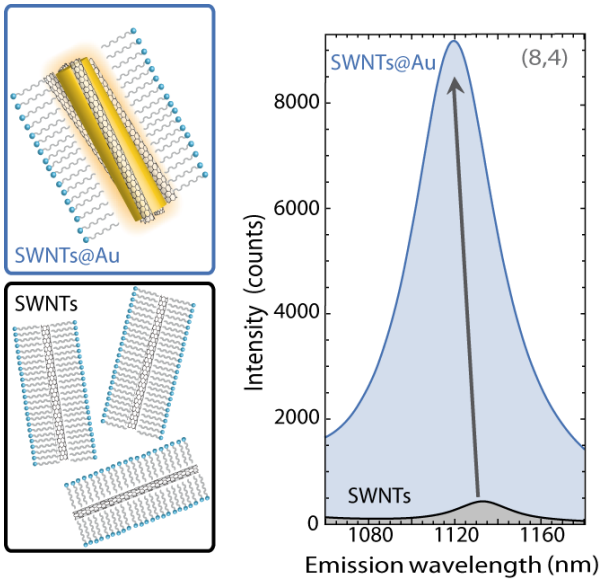

Fig. 7.3: Sketch of the SWNTs encapsulated inside the gold nanoparticle micelle (top). Sketch of the micelle solely encapsulating the SWNTs(bottom). Excitation line of the (8,4) tube indicating the strong enhancement of the luminescence (right).

The coating of SWNTs with colloidal nanoparticles showed a PL enhancement of a factor of 20 [11]. This was pursued by exploiting the micelle swelling procedure. The main difference with respect to the approach described before is that this time the SWNTs are transported into the micelle suspending the metallic nanoparticle, as seen in Figure 7.3. This strategy is beneficial as the wet chemical synthesis of the gold particles uses the surfactant CTAB - Cetyltrimethylammoniumbromid as a growing agent. At the end of the growth the surfactant forms a micelle around the gold particles [169], [170]. Thus it is much easier to insert the hydrophobic SWNTs into the gold solution: While stirring, the SWNTs enter the micelles and are immobilized close to the gold surface. The SWNT-AuNR hybrids exhibit increased luminescence. A strong enhancement of the tubes was observed with respect to reference sample of pure CTAB debundled SWNTs. The enhancement showed to be selective towards certain chiralities. The highest enhancement factor is observed for the (8,4) tube, see Fig. 7.3. This was the first experimental evidence of plasmonic nanoparticle-SWNT hybrids exhibiting enhanced photoluminescence achieved by the micelle swellling approach. For the full description of the findings and the synthesis please refer to Ref. [11]. Recently, other groups started to work on the enhancement of SWNTs through colloidal metallic nanoparticles. Yang *et al.* for example covered SWNTs with specially synthesized gold DNA strands, a mechanism similar to the previously described polymer wrapping. They achieved an enhancement of roughly 10 times and also observed a selectivity toward certain chiralities [171].

In the following sections I will outline the evolution of this project paying special attention to: i) The influence of the stirring time on the overall enhancement will be investigated. ii) The matching of the plasmon resonance with the excitation and emission wavelength of the tubes to analyse its effect on the enhancement. iii) Influence of the gold particle hybridization on the lifetimes of the SWNTs . iv) Attachment of the gold particles on the SWNTs via the [2+1] cycloadditon.

7.3 Improving the Hybrids

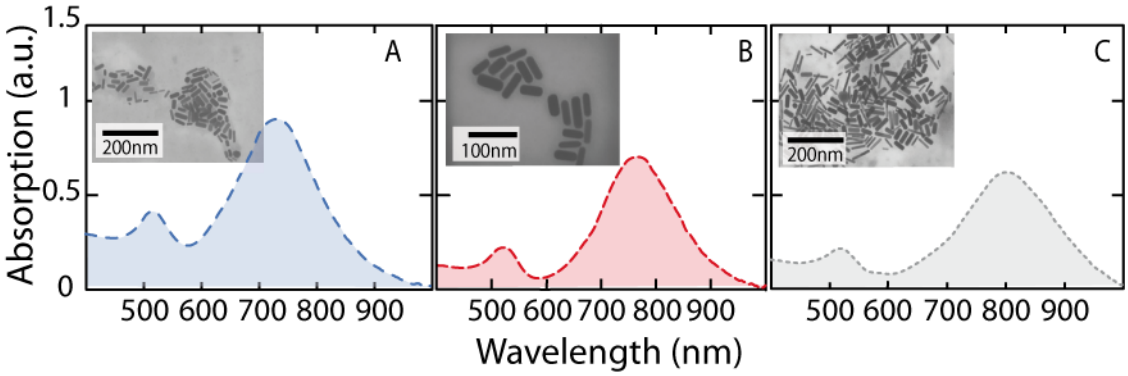

Fig. 7.4: Absorption spectra of for different AuNP (A–C). The transversal and longitudinal plasmon resonance can be recognized in the spectra. The inset in the left upper corner shows the SEM image of the synthesized AuNP.

The π-hybrid luminescence intensity proved to be sensitive towards the gold nanoparticle-SWNTs ratio we could identify an optimum ratio between the gold particles and the SWNTS. Below this concentration no significant enhancement was observed. Above the critical concentration, the micelles reach their loading capacity and burst due to the excess of SWNTs. This results in precipitation of the tubes and a decrease of the overall observed intensity [11]. In this Section I want to analyse the influence of another synthesis parameter, the stirring time. In order to distinguish whether the enhancement scales with the amount of hybrids or with the stirring time, the hybrids were stirred over a time span of several days. If the hybrids are improved by extending the gentle isolation procedure, their enhancement should increase during the longer stirring period. In order to estimate the changes in luminescence intensity, I took single excitation lines and PLE maps of the hybrids after 24h, 47h, 119h, 179h, 269h, 319h, and 458h of stirring.

Three different gold particles, named as A, B, and C were exploited in this work. Experimental details on the gold particle and hybrid synthesis can be found in Ref. [12]. I chose to exploit particles with different plasmonic features in order to rule out a dependency on the plasmon resonance. Their optical and morphological properties can be discerned in Fig. 7.4. All particles are rod-like shaped. The rods in sample A have a diameter of 10 nm and a length of 80 nm. Sample B shows short thick rods with a width of 20 nm and length of 60 nm. Sample C shows some polydispersity in the morphological distribution; the average diameter is 10-20 nm and the length 100 nm. The longitudinal plasmon resonances occur at 730 nm, 775 nm and 800 nm for A, B, and C, respectively. All of the three sets of particles were used for π-hybrid production. Furthermore, a reference sample was prepared by stirring SWNTs in a water-CTAB solution following the procedure of Ref. [11]. The advantage of CTAB is that beyond already suspending the gold particles within its micelles, it is also efficient at isolating and debundling the nanotubes and allows the direct comparison of the luminescence intensity for the samples with and without gold.

7.3.1 Photoluminescence Yield

Figure 7.5 compares the PLE maps of the hybrids produced with the particles A-C with the reference sample. One can recognize the most abundant tubes chiralities present in the solutions, namely the (7,5), (7,6), and (8,4) chiral species. Since the (7,5) and (7,6) are located on the same excitation window and since the 650 nm excitation line exhibits the brightest emission, I decided to monitor the emission trend obtained by exciting the samples at 650 nm (red highlighted lines within the PLE charts) to follow the intensity of the emission of the (7,5) and (7,6) chiral species vs. stirring time.

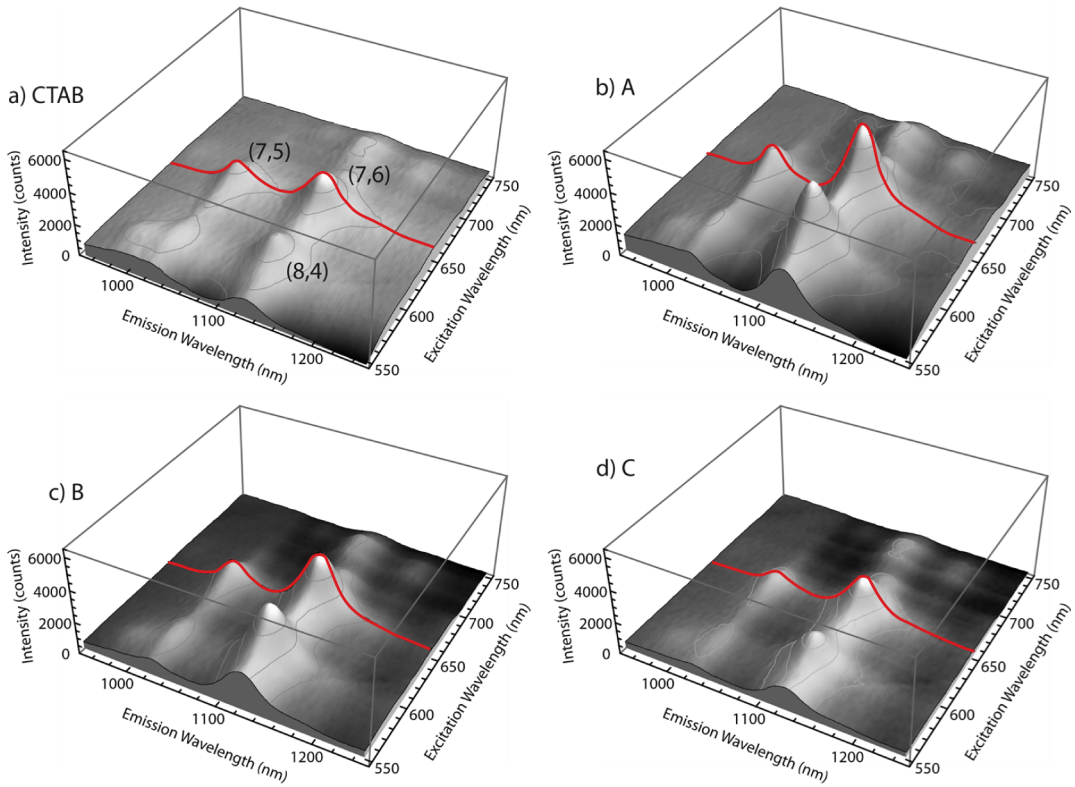

Fig. 7.5: 3D PLE maps of a) SWNTs stirred in CTAB, π-hybrid produced with b) the gold particles A, c) with particles B, and d) with particles C. In all four samples one can clearly identify the peaks due to the (7,5), (7,6), and (8,4) chiral species, which are the most abundant species in our samples. The red line is drawn in correspondence of the 650 nm excitation line, which can be used to excite the emission from both of the (7,5) and (7,6) chiral species.

The left panel of Figure 7.6 a) shows the spectra after 24h of stirring. The spectra were magnified by a factor of 10x for better visualization. Even if low, the photoluminescence (PL) emission of the (7,5) and (7,6) tubes can be identified, indicating successful debundling. This is consistent with the observations made by Wenseeler *et al.* on the ability of different surfactants (ionic, zwitter-ionic and non-ionic) to solubilize SWNTs [46]. They showed that gentle stirring lead to debundling and suspension of the tubes. Among the cationic surfactants, they showed that CTAB, the surfactant used for the synthesis and suspension of our AuNPs, was the best performing one. Accordingly, during the gentle stirring process, the SWNTs get debundled and

enclosed within the AuNP-containing micelles and thus end up close to the AuNP sidewalls. In Figure 7.6 c) and d) the evolution of the emission can be traced for the (7,6) and (7,5) tubes of the reference sample and for the composites with the different gold particles: The PL signal increases with increasing stirring time. All π-hybrids as well as the reference CTAB sample show a similar trend: The emission yield gets brighter over time until it stabilizes after two weeks of stirring. Different particles with varying plasmonic features lead to hybrids with different emission intensities.

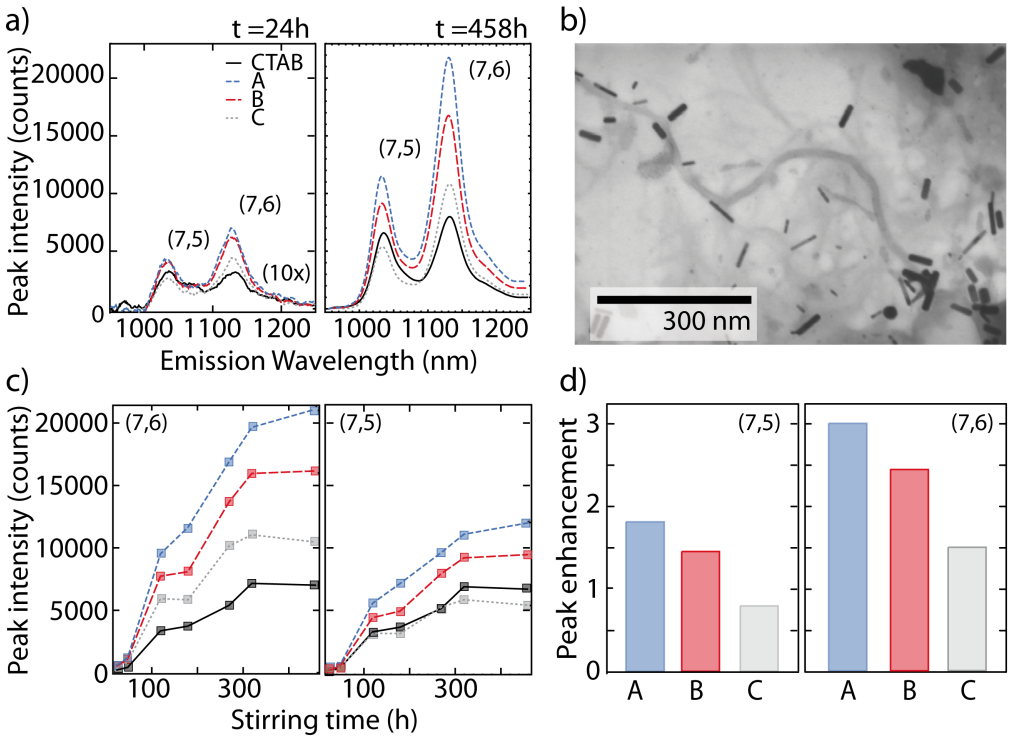

Fig. 7.6: a) 650 nm excitation line of the π-hybrids after 24 h of stirring scaled up by a factor of 10 and after 19 days of stirring. b) SEM image of the π -hybrids from sample A after 19 days of stirring, obtained after drop-casting the solution onto a substrate. c) Evolution of the emission intensity of the (7,6) and (7,5) tube over a period of 19 days. d) Final enhancement of the (7,5) and (7,6) tubes after 19 days of stirring.

The right panel of Figure 7.6 a) displays the emission spectra of the same samples after two weeks of stirring. By comparing those spectra with the left panel in Fig. 7.6 a), it can be seen that the emission signal increases, leading to roughly ten times stronger luminescence. This suggests that i) the emission intensity increases due to a more efficient debundling of the tubes, and thus more hybrids are formed or ii) the hybrids are improved during the stirring time. Fig. 7.6 d) reports the enhancement of the π-hybrids after 19 days of stirring. The A AuNPs, with the longitudinal plasmon resonance around 730 nm, provide the highest enhancement. The B and C AuNPs, with plasmon resonances at longer wavelengths, show lower enhancement. The effect of the plasmonic properties on the emission yield and enhancement, respectively, will be subject of section 7.4. Please note, the SEM micrographs of the hybrids in Fig. 7.6 b). Even if the structure of the hybrid gets disrupted once removed from the suspension and dropcasted

and dried onto the SEM grid surface, one can recognize that the average length of the SWNTs is much bigger than the length of the gold particles. This gives an useful indications of the phenomenological framework in which the enhancement process occurs, i.e. localized metal plasmon interacting with delocalized semiconductor excitons. Such a model was introduced to explain the phenomenology of an analogous system, namely CdTe nanowires coated with gold nanoparticles [172].

7.3.2 Photoluminescence Enhancement

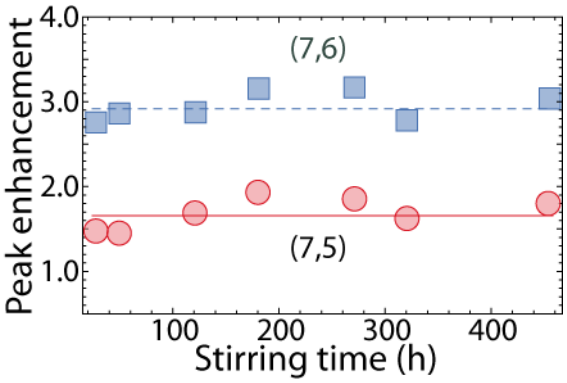

Fig. 7.7: Enhancement of the (7,5) and (7,6) tubes of the π-hybrid produced with sample A.

The better debundling or the improved hybrids can lead to a similar result regarding the enhancement. To proof whether the extended synthetic procedure improves the composites, I estimated the enhancement of the π-hybrids luminescence with respect to the reference CTAB sample. To this purpose, I compared the PLE signal of the π-hybrids with the CTAB reference sample. Even if the overall emission yield of the samples increases with stirring time, the emission enhancement factor does not. In Fig. 7.7 one can see that the enhancement for the (7,6) π-hybrids remained constant over the 19 days of stirring (Fig. 7.7, blue data points). Similarly, the (7,5) tubes' enhancement remains constant at a different value (Fig. 7.7, red data points). All other chiralities present in the hybrids produced with gold particles A-C showed a similar trend. The π-hybrids show already constant enhancement from the beginning of the stirring process on. The gentle debundling procedure makes the tubes penetrate into the CTAB micelle already containing the AuNP, where the proximity of the gold is causing the enhancement of the luminescence. In the following days, more π-hybrids are produced or more tubes penetrate the same micelle, which leads to stronger emission. The experimental evidence clearly shows that the amount of enhancement is thus dictated by the plasmonic feature of the metallic particle and does not change with the preparation condition. It should be noted that this process can proceed to a maximum loading of the micelles, after which tube-tube interaction comes into play causing quenching of the SWNTs emission [11]. To avoid this, I worked at a SWNT concentration level far below the quenching threshold level (see [11]) and thus no tube-tube quenching was encountered.

Those results have proven that the proximity of SWNTs to AuNP leads to enhancement of the luminescence, which varies for AuNPs of different morphologies but not with stirring time. The correlation between the efficiency of the enhancement process and the overlap between the SWNTs energetic and the AuNPs plasmonic features will be subject of the next section.

7.4 Resonance Study

In Figure 7.6 d) in the last section I showed that tuning the plasmon resonances lead to different enhancement factors for different tubes. The (7,6) species covered with different plasmonic particles, for example, had enhancement factors ranging from 1.5 to 3, depending upon the metallic particle SPR. Those findings lead us to the idea to investigate the influence of the SPR on the enhancement by performing a resonant plasmonic study of the effect on the optical response of SWNTs located in the vicinity of metallic nanoparticles [1].

Metallic nanoparticles with different plasmon resonance were coupled with SWNTs and the resulting enhancement factors were evaluated. Carbon nanotubes are ideal candidates for such a study as their excitation and emission energies are well separated and can be addressed separately by specific plasmon wavelengths. By fine-tuning the amount of chemicals used for the gold particle growth, particles with different aspect ratios were synthesized. The diverse particles lead to different plasmon resonances, covering the range from 530 nm up to 1100 nm. The particles were chosen to cover the excitation wavelength and emission of the chiral species typically present in the CoMoCat samples. The hybrids then were synthesized as described in Ref. [11], [12]. I investigated the enhancement factor for the individual SWNTs species yielded by the different plasmon resonances. First the excitation of the SWNTs was matched with the metallic nanoparticles and stepwise was the plasmon resonance increased to higher wavelengths covering the emission of the tubes. Figure 7.8 displays the enhancement factor as a function of the SPR wavelength for the (7,5), (7,6), and (8,3) tubes. Fig. 7.8 a) depicts the excitation and emission of the (7,5) tube (respectively the blue and red bands) and compares it with the enhancement dependence to the plasmon resonance. The shortest plasmon resonance wavelength used was the one of gold nanospheres, which is around 530 nm. Lower plasmon bands are possible but would require the use of alternative metals (e.g. silver) and could lead to other mechanism influencing the enhancement process. No significant enhancement could be observed for the gold nanosphere with a plasmon resonance of 530 nm. With increasing plasmon resonance, the enhancement scales up.

The highest enhancement was observed for particles which SPR is redshifted in respect to the excitation wavelength of the tubes. For the (7,5) tube, the maximum enhancement was achieved for a SPR which is shifted by 84 nm (220 meV) with respect to the excitation wavelength of the tubes. After a certain wavelength (in the case of the (7,5) tube 741 nm) the enhancement factor starts to decrease again until it disappears at a SPR of 840 nm. From this point on the emission gets quenched. The more the SPR penetrates the emission window of the tube the more gets the luminescence quenched. Fig. 7.8 b) shows the course of the (7,6) tube for the different SPR, following a similar trend as the (7,5). No significant enhancement can be observed for the lower plasmon wavelength. For the (7,6) tube, the maximum enhancement is observed for a plasmon resonance which is redshifted by 80 nm (210 meV) to the maximum of the excitation the highest enhancement could be observed. Past this point, the enhancement drops again and approaches the original intensity of the pristine (7,6) tube.

[1] A manuscript on the resonant plasmonic study is preparation.

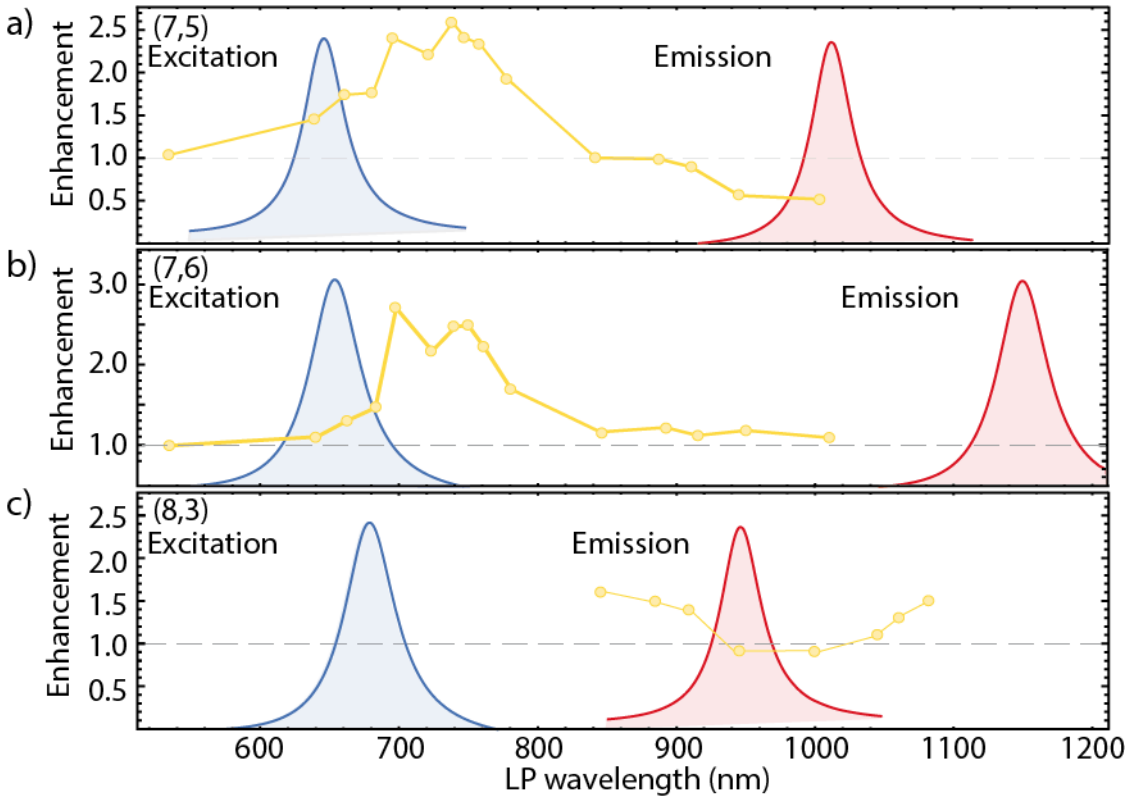

Fig. 7.8: Resonant plasmonic response of the nanotubes' emission enhancement for hybrids obtained with AuNRs with different longitudinal plasmonic wavelengths, spanning from 531 nm up to 1100 nm. The resonance profile differs for different SWNTs chiral species. The trend for the (7,5), (7,6), and (8,3) species are reported here with their corresponding excitation and emission spectra.

Other species exhibit the same trend but with different resonance profiles, where as tubes with a comparable excitation wavelength show a similar resonance pattern. Table 7.1 summarized the excitation wavelength, the plasmon wavelength at which the highest enhancement occurs and the redshift with respect to the SWNTs excitation energy as well as the FWHM of the resonance profile. Those results nicely show how the individual plasmon resonance affect the different tube species in different ways.

Chirality	λ_{ex} (nm)	λ_{SPR} (nm)	ΔE (meV)	FWHM (meV)
(8,4)	602	700	295	250
(7,6)	649	729	210	233
(9,4)	720	756	80	90
(7,5)	645	729	220	221

Tab. 7.1: Excitation energy of the different tubes with the associated surface plasmon resonance which showed the highest enhancement. Furthermore, the corresponding energy difference between the excitation wavelength and the SPR wavelength are listed together with the FWHM.

In particular, the hybridization with gold particles with a plasmon resonance at 892 nm, a wavelength that overlaps with the emission window of some of the SWNTs, revealed interesting features: Figure 7.9 displays the whole set of SWNTs hybridized with those gold nanoparticles.

It can be observed how the individual chiralities react in different ways: Some of the tubes experience quenching while other show enhancement of their emission. It can be seen that tubes whose emission energies overlap with the surface plasmon resonance (SPR) of the metallic nanoparticle experiences quenching namely the (8,3) and (6,5) tubes. The tubes with higher emission energies, on the other hand, experienced enhancement of their luminescence.

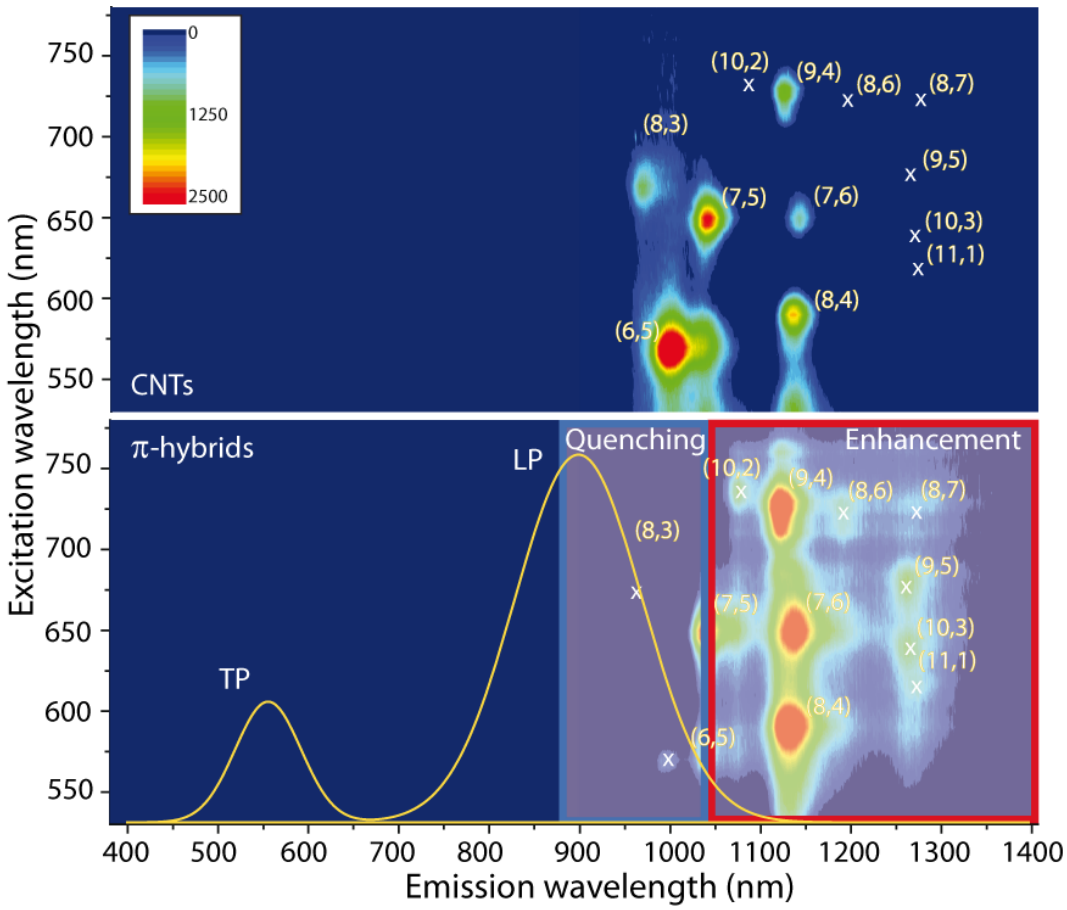

Fig. 7.9: a) 2D PLE map for the pristine SWNTs (upper map) b) 2D PLE map of SWNTs hybridized with 892 nm gold nanoparticles (lower map). Comparing the two maps one can clearly observe the enhancment and quenching of the tubes emission. The overlay of the SPR nicely demonstrates that the overlap of emission energy with the SPR leads to quenching of the tubes luminescence. There more the emission energy moves from SPR the more the emission is recovered and even enhanced.

The quenching of the (8,3) vanishes as soon as the SPR does not overlap with the emission wavelength of the tubes anymore. Figure 7.8 c) displays the evolution of the (8,3) tube for particles with a SPR between 840-1100 nm. It can be observed that the emission of the tubes first quenches and recovers for gold nanoparticles with a plasmon resonance higher than 1060 nm. When surpassing the emission wavelength of the tubes the luminescence not only got recovered it, furthermore, started to get enhanced. Please note, the fabrication of metal nanoparticles with longer SPR requires a sophisticated synthesis. We reached our limit for metallic nanoparticles exhibiting a SPR at 1100 nm, restricting our resonance study. Only for the (8,3) tube we were able to exit the emission window with particles showing a SPR at 1050-1100 nm.

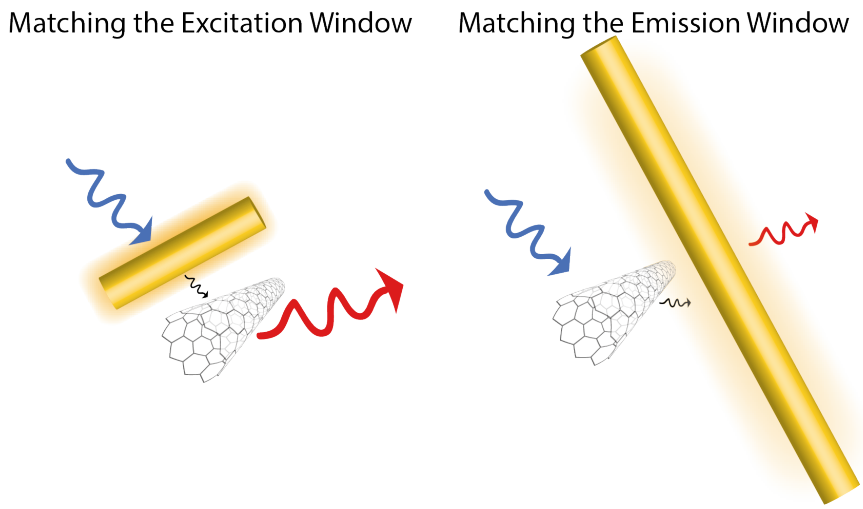

Fig. 7.10: Sketch indicating the different mechanism influencing the gold nanoparticle SWNT interaction. When matching the SPR with the excitation window of the tubes first the plasmon gets excited which non-radiatively excites the tubes leading to enhancement of the tubes emission. If the SPR overlap with the emission of the tubes the excited SWNT non-radiatively transfer the energy to the plasmonic nanoparticle leading to quenching of the tubes emission.

The different enhancement behaviours are explained as follows: When matching the excitation window of the tubes, first the plasmon resonance of the metal particle gets excited which creates an enhanced electric field. The enhanced field contributes to a higher excitation rate of the SWNTs resulting in stronger emission. Other groups also reported on the strongest enhancement in the near field for particles with a redshifted plasmon resonance with respect to the fluorophores absorbance [173]. On the other hand, if we match the emission window of a SWNT with the plasmonic frequency of a metallic particle, a different mechanism comes into play. The role of the SWNT and plasmonic particles switch their roles. The absorption of the incoming radiation first excites the SWNTs: after a fast internal relaxation the SWNTS emits a photon. The close proximity to the gold nanoparticle offers an additional de-excitation pathway to the system, namely the excitation transfer from the tube to the metal. The emission of the tubes quenches due to heat conversation or excitation of the plasmon. A similar behaviour was theoretically predicted in Ref. [174] and experimentally shown in [175]. They showed that the strongest enhancement in the near field was observed for a SPR redshifted in respect to the emission, and quenching occurs if the wavelengths coincide.

7.5 Lifetimes

So far, the key to efficient enhancement was related the tube-gold proximity. To gain a deeper insight and identify which mechanism contributes to the enhancement, we employed time resolved spectroscopy to monitor the de-excitation of our π-hybrids. The optical and morphological properties of the plasmonic nanoparticles used in this work are depicted in Fig. 7.11 a, b). Our gold nanoparticles exhibit transverse and longitudinal plasmon resonances, respectively, at 550 nm and 920 nm. SEM analysis reveals a small polydispersion in the gold

nanoparticles' morphology. The majority (approx.85%) of the particles are rods, 15 nm wide and 70 nm long. Figures 7.11 c,d) display the SWNTs absorption spectra in the pristine (black, continuous) and π-hybrids (blue, dashed) samples. After hybridization a decrease of the band associated with small-diameter tubes and an increase of the one associated with bigger diameter tubes can be observed. The full-width at half maximum of all the bands increased as well.

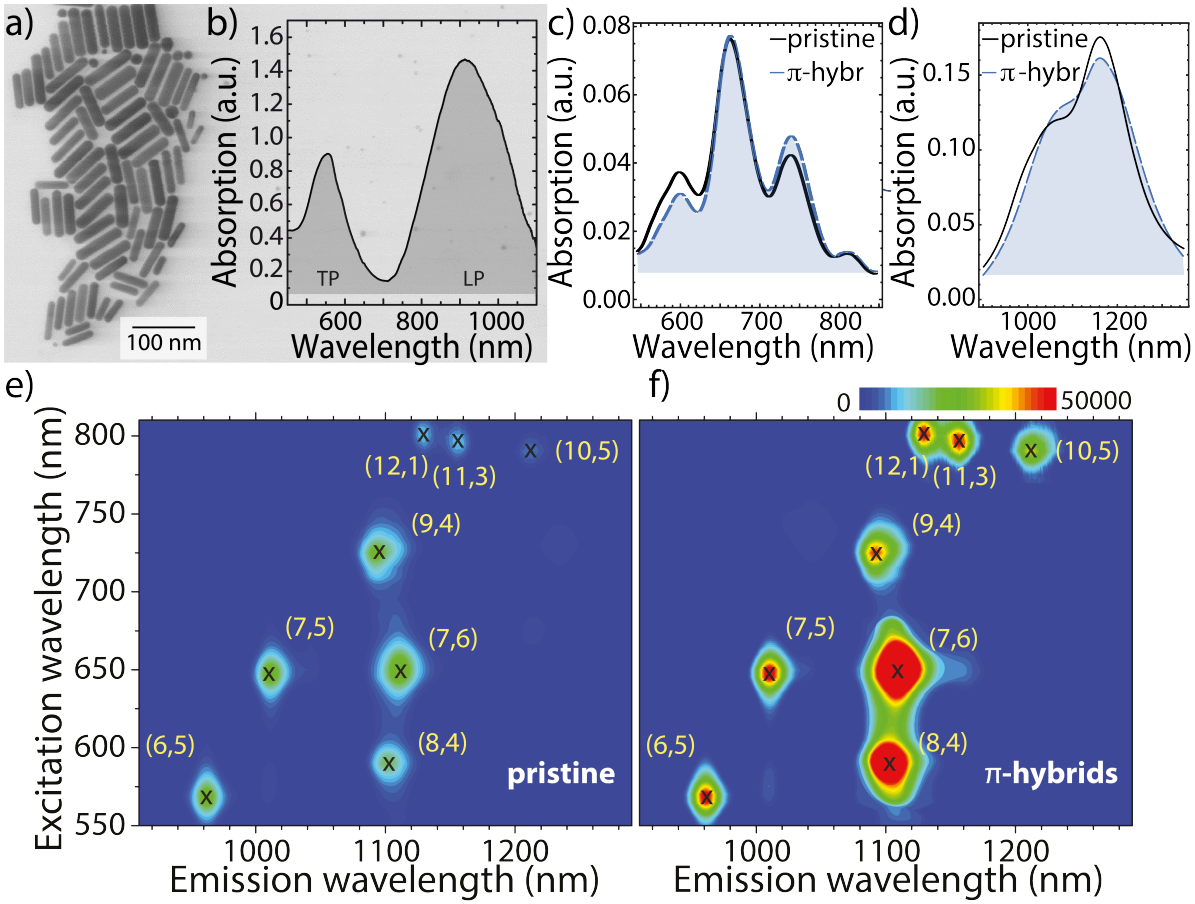

Fig. 7.11: a) SEM image of the used AuNRs. The sample is mostly composed of rods with an average width of 15 nm and length of 70 nm. b) Absorption spectra of the AuNRs. The transversal plasmon resonance is located around 550 nm and the longitudinal plasmon resonance around 920 nm. Note, that the absorption features of the SWNTs are strongly cloaked by the plasmonic bands of the gold nanoparticles. c) Comparison between the absorption spectra of pristine SWNTs and π-hybrids in the E_{22} region. d) Comparison between the absorption spectra of pristine SWNTs and π-hybrids in the E_{11} region. The π-hybrid spectra in c) and d) have been acquired using an AuNRs blank solution. 2D excitation-emission map of e) pristine and f)π-hybrids samples. The enhancement factors are summarized in Table 7.2

I conducted 2D excitation-emission measurements to identify the tubes present in the samples and their hybridization-induced enhancement factors [176]. Figure 7.11 e) and f) show the PLE maps. The luminescence enhancement factors (reported in Table 7.2) range between 1.3 and 4.8. The strongest enhancement occurs for the nanotubes species whose excitation window matches the TP resonance of the AuNRs, in particular the (7,6) and the (8,4) species. Interestingly, the highest enhancement has been observed for nanotube species redshifted with

respect to the absorption maximum matching the findings of Section 7.4. This is consistent with similar observations in simple molecular systems and in covalently functionalized carbon nanotubes [173], [8]. Please note, that while the TP resonance of the AuNRs occur in the excitation window of some of the SWNT species, the LP modes, with their longer wavelengths, are out of the excitation window of the SWNTs and do not contribute to the enhancement process. As mentioned before, we need to monitor the behaviour of nanotubes outside the plasmon resonance window to ensure the detuning condition. The most suitable candidates for this purpose are the tubes belonging to the *laola* family with index q = 25 (i.e. the (12,1), (11,3), and (10,5), cfr. Fig. 7.11 e), which satisfy the plasmon detuning condition and match resonantly with the wavelength of the used pump laser. In particular, we monitored the response of the single (12,1) species, whose emission lies within the spectral region of our probe beam. Figures 7.11 compare the emission intensities before and after hybridization. The resonance window of the nanotubes does not spectrally shift after hybridization: Changes in intensity thus directly relate to changes of the emission yield of the π-hybrids. The enhancement factors are summarized in Table 7.2.

nanotube species	(6,5)	(8,4)	(7,5)	(7,6)	(9,4)	(12,1)	(11,3)	(10,5)
enhancement	1.3	4.4	2.3	4.8	2.3	2.2	1.9	2.4

Tab. 7.2: Enhancement factors of the different nanotube species present within our samples.

7.5.1 Time-Resolved Spectroscopy

Upon optical excitation, SWNTs undergo a de-excitation process with a fast and a slow component [177], [178]. The fast part takes place on a timescale of hundreds of femtoseconds up to one picosecond whereas the slow part develops over a scale of few tens of picoseconds. Such a double-exponential trend is observed in amorphous carbon nanoparticles as well, where the involved time constants are greater by one order of magnitude [179]. In SWNTs, the fast component is ascribed to the relaxation processes that thermalize the system at the bottom of the first excited state. This process is non-radiative. Its equivalent in the simplified Jablonski diagram of Fig. 7.2 is the transition from E_{22} to the bottom of E_{11}. The slow component, on the other hand, corresponds to the transition from the bottom of E_{11} to the ground state. This part can include radiative and non-radiative de-excitation pathways.
To monitor the temporal response of an excited system, we resorted to pump-probe transient-absorption spectroscopy. The Pump-probe analysis follows de-excitation of a system through all pathways its, radiative and non-radiative, determining the total lifetime of a certain level. In our case, transient absorption monitors the whole process, revealing the characteristic double exponential trend which starts from the E_{22}-to-E_{11} thermalization (the fast, non-radiative process) up to the de-excitation from the E_{11} to the ground state (the slow process, through radiative and non-radiative channels).

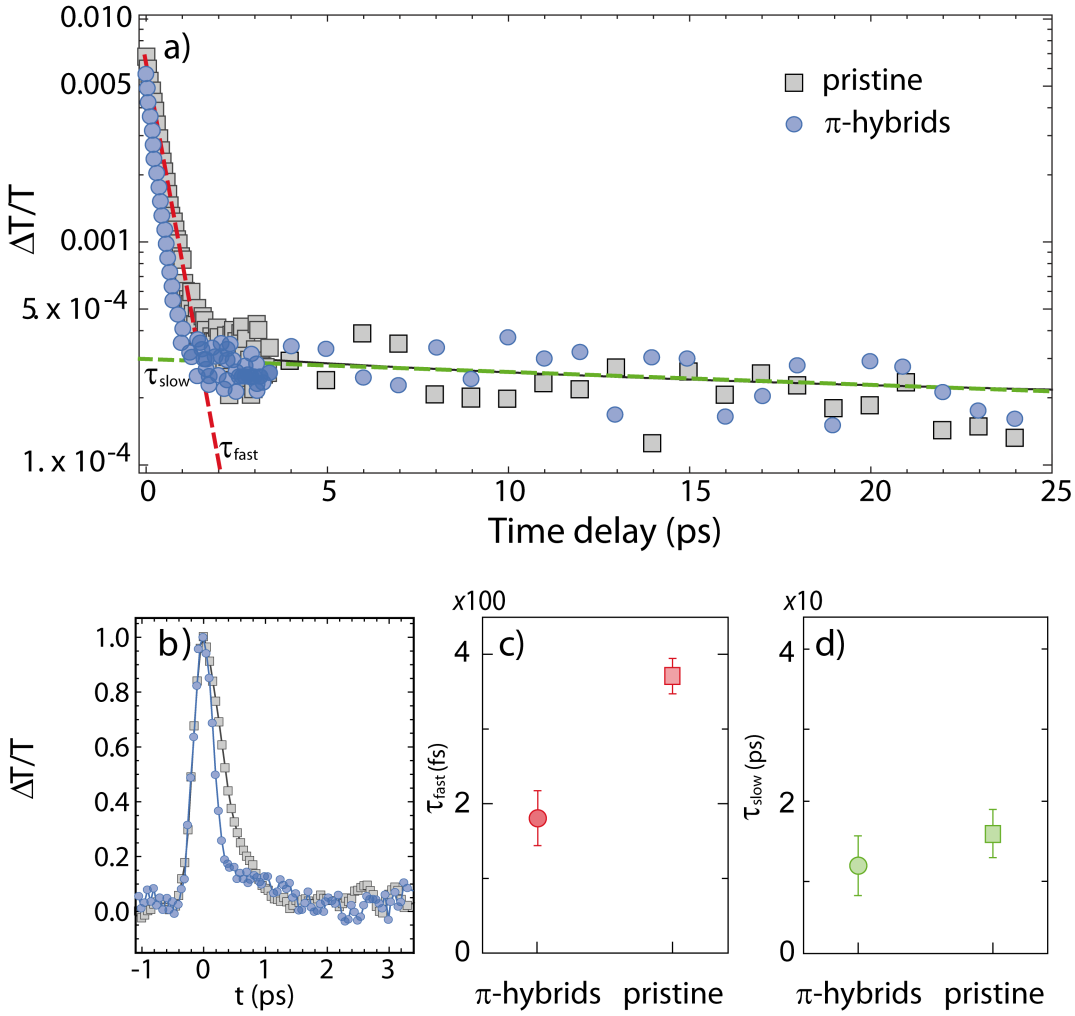

Fig. 7.12: 2d excitation-emission map of pristine a) and π-hybrids b) samples. The enhancement factors are summarized in Table 7.2

We monitored the total lifetime of E_{11} and its changes arising from the additional de-excitation pathways (radiative or non-radiative) due to the metal presence. For consistency sake with the most recent investigations by two-colour pump and probe of the carbon nanotubes response [178], [180] we adopt the notation by Dyatlova *et al.* when referring to fast (intra-band) and slow (inter-band) components of the decay. We emphasize that those are not the fast and slow components observed in time-resolved photoluminescence experiments, which are instead due to the balance between bright and dark excitonic states and occur on longer time scales than the ones monitored here. The slow component of our transient absorption spectra τ_{slow} carries the information about the total lifetime through all, radiative and non-radiative, de-excitation channels and corresponds to τ_0 in Eq. 7.3. This slow component changes when interacting with gold, giving τ_m in Eq. 7.3. The investigation needs to be performed in the detuned configuration, avoiding overlap between the tubes and gold energy bands to get rid of spurious effects [181]. The detuning configuration is warranted because, at resonance with the plasmon frequencies, the strong local enhancement of the electromagnetic field could alter the energetic structure of tubes, for example resulting in hybridized plasmon-exciton states or even

more complex phenomena. To this purpose, among the different possible nanotube species is important to select a species lying outside the plasmonic window of the metallic particles. We monitored the response of the (12,1) nanotube that satisfies the de-tuning requirement and can be resonantly excited with the fundamental beam of our pump laser (Ti:Sa laser, 800 nm). Please note, that altering the size of the metallic nanoparticles would cause a shift of the spectral position of the plasmonic bands and break the detuning condition as well. We monitored the dynamics of our system with a two-colour pump-probe system, according to the configuration established by Dyatlova *et al.* [178][2].

The de-excitation dynamics of the samples follow a double-exponential behaviour, exhibiting a fast, sub-picosecond component ($\tau_{fast} < 1$ ps) and a slow component of several picoseconds ($\tau_{slow} > 10$ ps), see Fig. 7.12a. The obtained lifetimes are consistent with the values reported previously [182], [178]. The lifetimes of the π-hybrids are shorter than the ones of pristine nanotubes, see Fig. 7.12 b-d). This is consistent with experimental observations in analogous but simpler nanometal-emitter hybrid systems, e.g. dyes attached to gold nanoparticles, where the dye lifetime shortens after interacting with the metal [183]. However, nanotubes are more complex than simple fluorophores. They exhibit a fast component, during which the system undergoes a non-radiative thermalization, and a slow component, during which radiative and non-radiative interband recombination occurs. Both regimes can easily be identified in Fig. 7.12a. The trend of the fast and slow time constants for pristine samples and π-hybrids are reported in Fig. 7.12 c, d). τ_{fast} goes from (370$\pm$20) fs for pristine SWNTs to (180$\pm$40) fs for the π-hybrids. Similarly, τ_{slow} goes from (16$\pm$3) ps for the pure sample to (12$\pm$5) ps for the π-hybrids. After hybridization, the fast decay component changes ($\frac{\Delta\tau_{fast}}{\tau_{fast}} = 106\%$) much more acutely than the slow component ($\frac{\Delta\tau_{slow}}{\tau_{slow}} = 33\%$). Fig. 7.12 b) compares the first few picoseconds of the de-excitation process to highlight the speeding up of the hybrid fast-process.

The experimental results clearly show that the presence of gold nanoparticles shortens the slow and, even more acutely, the fast relaxation times of the SWNTs. Note that no signal can be detected from the transient response of a pure AuNRs suspension within the pump window. The response is either too weak or too fast to be disentangled from the instrumental response function. These observations are consistent with the overall trend observed previously where the relaxation times were found to be slower in isolated SWNTs *vs.* SWNT bundles or SWNT-polymer mixtures, indicating that tube-tube or tube-environment interactions provide additional decay channels [184], [185]. While the presence of gold nanoparticles is expected to locally alter the dielectric environment around the SWNTs, thus altering both their electronic [186] and phonon band structure [187], [188], the exact mechanisms behind the influence of the gold nanoparticles on the SWNTs await elucidation via further experimental and theoretical work.

[2]The pump-probe transient-absorption measurements were performed by Manoj Kumar and Annalisa Bruno from the Nanyang Technological University Singapur.

Obtaining an estimation of the decay times helps to evaluate the contribution of the two terms of the quantum yield of the system, allowing, for the first time in such systems, to disentangle whether the enhancement is mainly due to stronger pumping or faster de-excitation (Eq. 7.1- 7.3). By inserting the experimental time constants into Eq. 7.3, one obtains that the lifetime-change term contributes to the enhancement with a value F_{rad}= (0.7±0.3). This implies that the local-field contribution is F_{exc} = (3±1). Note that the estimate of F_{rad} might be biased by the neglect of Joule losses that are candidate non-radiative decay channels in plasmonic systems [189]. The stronger emission from the π-hybrids is not governed by the faster de-excitation, as previously observed for SWNTs dropcasted onto rough Au surfaces [159]. We instead find that the stronger pumping due to the localized plasmonic near-field actually drives the enhancement, compensating the non-radiative losses from the metal. This is due to the homogeneous exposure of the SWNTs to the plasmonic near-field ensured by the micelle encapsulation, rather than the less-controllable match with the plasmonic hot-spots of the rough metallic surfaces. This finding is highly relevant for the improvement of the enhancement process, indicating that the parameter to tailor for improving the efficiency of the π-hybrids' enhancement process is the intensity of the near-field localized around the surface of the metallic particles.

7.6 Covalent Functionalization

Section 7.3.1 displays a SEM image of the yielded hybrids from the micelle swelling approach. After drop casting the solution on the SEM grid one observes a disarray of tubes and gold particles due to the sensitivity of the micelles towards changes in the environment. The placement onto the copper grids lead to disruption of the micelles causing a disordered scattering of the components. This observation underlines the fragility of the micelle swelling process. In solution the hybrids remain stable and one can investigate their characteristics. Inserting them into a different environment, however, leads to demolition of the hybrids. The [2+1] cycloaddtion could be a solution for this problem. A first question arising would be how to immobilize the gold particles onto the SWNTs. A common approach to attach molecules on gold surfaces is with the help of thiol groups, see Fig. 7.13 a). Thiols are known to strongly bind to metal surfaces in particular to gold surfaces e.g. it is used to decorate gold surfaces with monolayers of molecular moieties [190]. By replacing the chlorine atom of the triazine with a thiol bearing group, we could decorate SWNTs with gold nanoparticles. Thus, we are adding a new component to the toolbox of the covalent functionalization. The main advantage is the strong binding of the thiol to the gold with that the possibility to transfer the hybrid into different media or place them on to substrates. The experimental details and characterization of the thiol compound can be found in Ref. [8]. Here I want to report on the influence of the optical properties of the SWNTs.

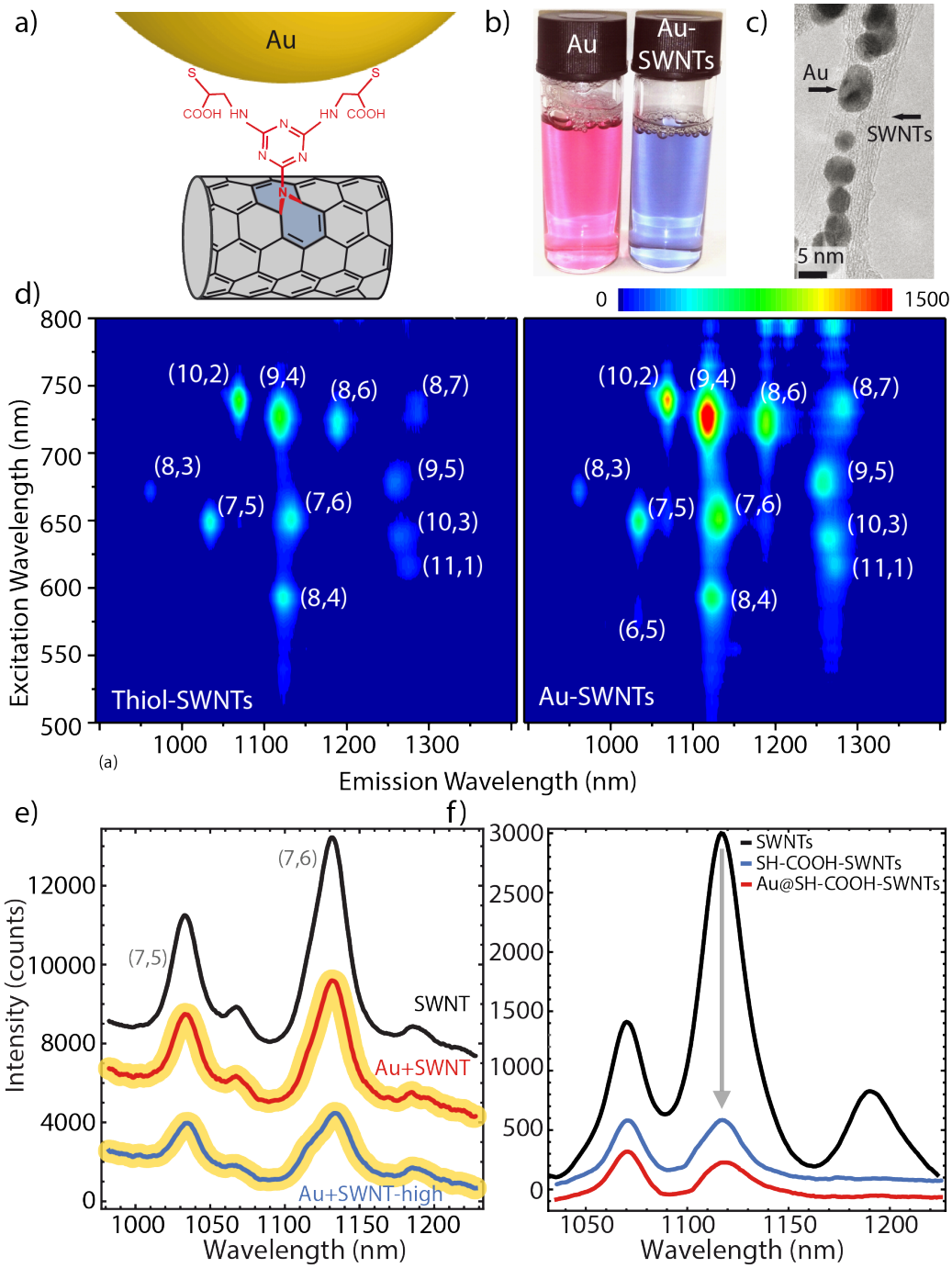

Fig. 7.13: a) Schematic illustration of the attachment of the gold particle onto the SWNTs b) Before the addition of the thiol functionalized SWNTs the plasmonic gold nanoparticle solution showed a pink staining. The addition of the SWNT induced a sudden change of the colour to blue. c) TEM image of the nanoparticles attached to the SWNTs. A chainlike arrangement of the gold spheres onto the tubes can be observed. d) 2D PLE map of the tubes before (left) and after (right) hybridization with the gold sphere. A clear enhancement of the tubes luminescence could be observed. e) 650 nm excitation line of the pristine tubes, tubes mixed with gold particles and triazine functionalized tubes with gold nanoparticles. f) Emission of thiol-carboxylated nanotubes (SH-COOH-SWNTs) and thiol-carboxylated nanotubes with gold nanoparticle attachment (Au@SH-COOH-SWNTs).

After adding the gold particles to the SWNTs a direct interaction could be seen. The pinkish gold solution turned immediately blue after addition of the SWNTs indicating an interaction between the Thiol-SWNTs and the gold particles (Fig. 7.13 b). This observation leads to the assumption that we change the morphological characteristics of the SWNTs as the blue colour indicates the coupling of the plasmon resonances. TEM imaging gave the explanation for the changes in colour. Figure. 7.13 c) depicts a small bundle of SWNTs. A chain like agglomeration of the gold particles along the SWNTs can be observed. The close packing of the particles result in coupling of the individual plasmon resonance and thus changes in the overall plasmon resonance. The TEM helped i) to identify the origin of the changes in the plasmon resonance, ii) proofed the successful functionalization through the gold particles and iii) showed their robustness towards deposition onto substrates. The main goal of this approach was to observe enhancement of the SWNTs luminescence. In Fig. 7.13 d) displays the 2D PLE maps of the Thiol-SWNT without gold and with gold functionalized SWNTs. Most of the tubes showed an enhancement factor of up to 2. This is a first proof of concept, that the [2+1] cycloaddition addition yields SWNTs-gold hybrids with enhanced luminescence.

To single out the importance of the thiol-triazine based immobilization in the enhancement process we performed two control experiments. In a first experiment, gold nanoparticles were mixed with pure SWNTs and respectively with triazine functionalized SWNTs. None of those samples showed enhanced emission as for the Thiol-SWNTs. This experiment showed that the attachment of thiol is crucial in order to anchor the gold to the tubes surface and thus observe the plasmonic enhanced emission of the tubes (see Fig. 7.13 f). In a second control experiment, we observed whether SWNTs functionalized with thiol via the covalent acid treatment leads to enhancement of the luminescence. The tubes were treated as described in Ref. [70] and subsequently functionalized with thiol via the COOH groups resulting from the acid treatment. The prepared samples were than mixed with gold nanoparticles to promote gold attachment onto the covalently functionalized tubes. Figure 7.13 f) displays the single emission line of pure SWNTs, SWNT functionalized via the acid treatment with thiol, and mixed with gold nanoparticles. It can be observed that the acid treatment significantly quenches the tubes emission and the attachment of gold particles had no influence on the tubes' emission. Those control experiments highlight the superiority of the [2+1] cycloaddtion addition routine and the relevance of the thiol linker to obtain robust SWNT- Au hybrids with enhanced emission. These hybrids are promising candidates to further explore the interaction of SWNTs and gold particles more experiments need to performed to improve the hybrids and further characterize them.

7.7 Combining two Functional Moieties

An aspect which was not covered in this thesis, so far, is the combination and relative interaction between two or more functional moieties. The different entities could influence them self and strengthen their effect onto the tubes even more. Especially the combination with gold can lead to superior properties due to the enhanced electric field. During my thesis I started to combine switches and dyes, respectively with gold nanoparticles. Here I want to give a rough insight into the first results.

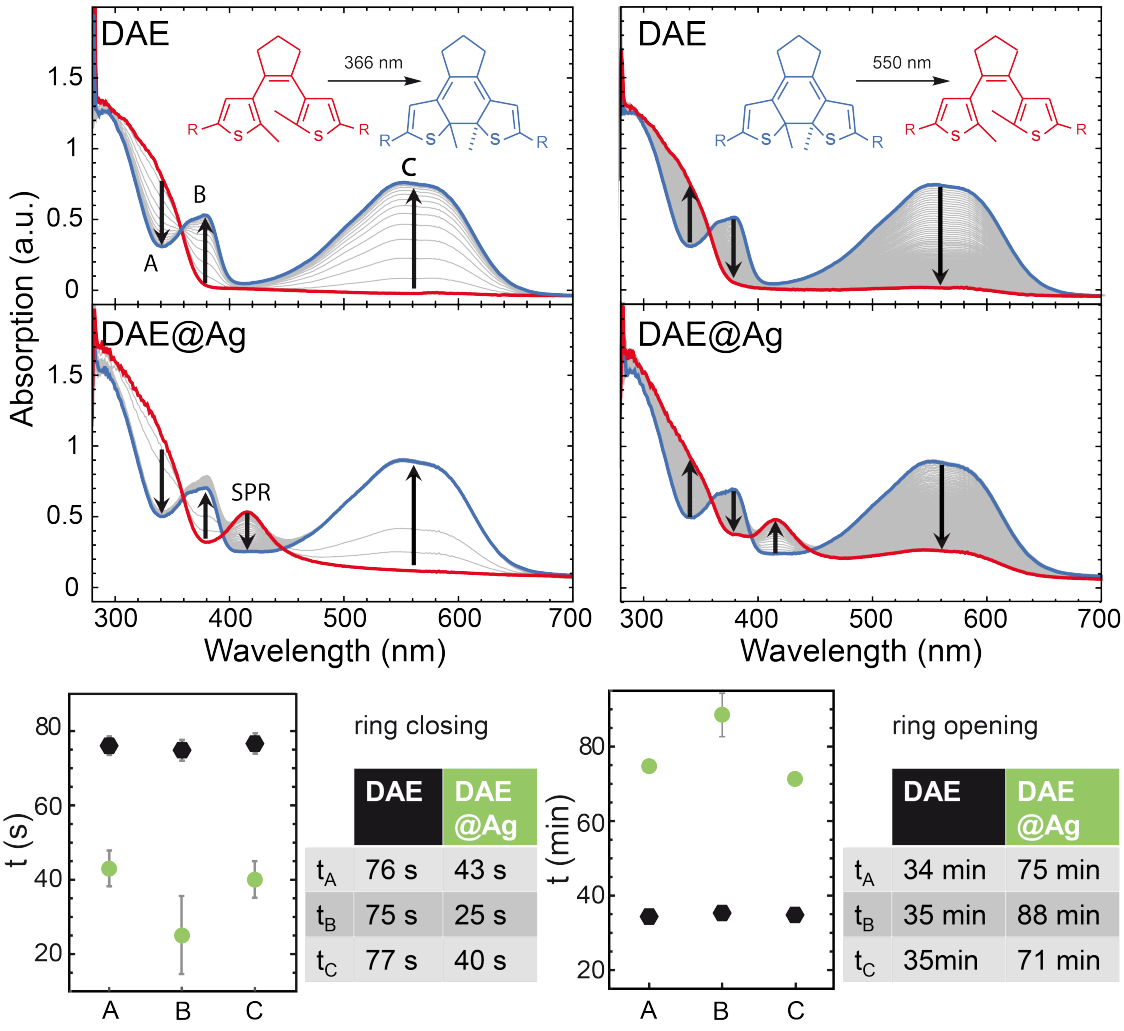

Fig. 7.14: The immobilization of the switch onto the silver nanoparticles does not inhibit the isomerization process. On the left in the upper panel the forth isomerization process of the pure DAE is displayed. The lower panel shows the isomerization of the switch attached to the metal surface. The left side displays the opening isomerization.

I showed that the presence of plasmonic nanoparticles lead to a change of the isomerization times of the molecular switch Diarylethylene (DAE). By attaching the photochromic switch DAE onto silver nanoparticles, I observed a faster forward isomerization and respectively a

slower back isomerization (see Fig. 7.14). Meanwhile absorption and scattering plasmonic bands of the silver nanoparticles disappear after ring-closing of the molecule and re-appear after ring-opening. Those first experiments already showed that the combination of switch and gold influenced their physical properties. INext tp investigating the system more detailed and optimizing it. It would be interesting to see how the combination of both would influence the optical properties of the tubes. By expanding this approach to spiropyran it could also help to overcome the obstacles Bluemmel *et al.* faced in their experiments with specially engineered SP-pyrene molecules which were non-covalently anchored onto the tubes via π-π-stacking. They only could observe the shift in transition energy in absorption bands via UV-Vis measurement. During the PLE measurements triggered back isomerization of the merocyanine which was induced by the photons needed to optically excite the SWNTs. The decrease of the back isomerization time could allow to fully investigate the sample and realize reversible alteration of the transition energies.

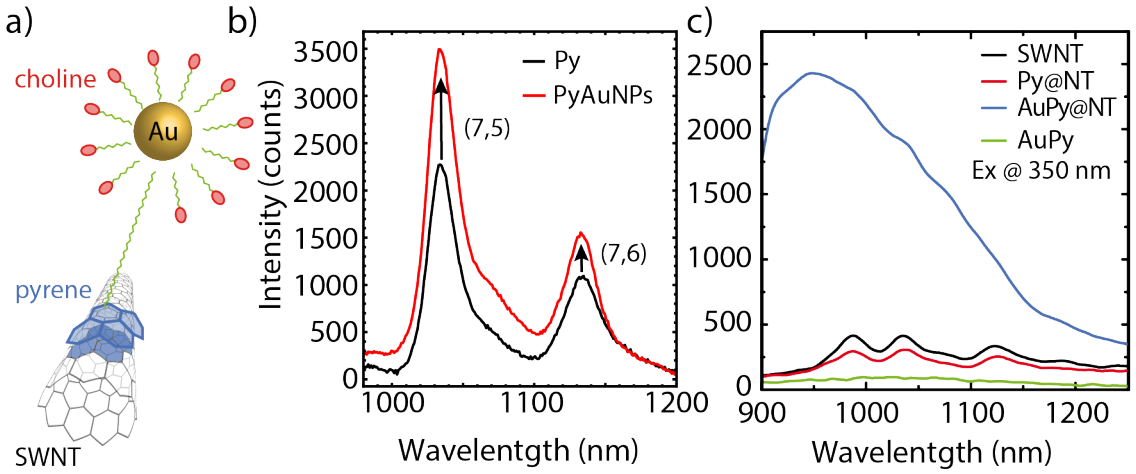

Fig. 7.15: a) Sketch of the gold nanoparticle immobilized on the CNTs through a pyrene anchor. b)Enhanced Emission of the tubes after the attachment of the 2 nm sized gold particles [191]. c) 350 nm excitation line comparing the pure SWNTs, SWNTs with pyrene, SWNTs with pyrene and gold, and pyrene and gold. The pyrene-SWNT-Au sample clearly indicates enhanced energy transfer between the SWNT and Pyrene.

Also the combination of dyes and gold particles in the presence of SWNTs can lead to superior physical properties. The combination of dyes and gold is an ongoing and well known field. The presence of the plasmonic particles can lead to an enhanced fluorescence of the dye.
In a first experiment we attached of gold nanoparticle onto SWNT sidewalls via a pyrene anchor as seen in Fig. 7.15 a). The idea was to establish another Au-SWNT system with enhanced luminescence. Fig. 7.15 b) shows the successful enhancement of the hybrids through this approach. The attachment of the gold particles lead to a roughly 50% enhancement of the PL yield as discussed in Ref. [191]. Those samples, however, revealed a more exciting feature in the UV range. A prominent peak could be observed in the excitation range of the pyrene hinting towards plasmonically enhanced energy transfer. Those samples showed enhanced indirect pyrene mediated energy transfer[3]. Those first proofs of principle showed that the

[3]A manuscript describing the plasmonically enhanced energy transfer is currently in preparation.

combination of dyes, gold nanoparticles and SWNTs lead to even stronger manipulation of the tubes properties. Hinting towards the endless functionalization possibilities of SWNTs and respectively the effect on their optical properties.

7.8 Comparison

In that chapter I showed how to achieve plasmon enhanced fluorescence of SWNTs with colloidal metal nanoparticles through two different approaches. The first one, the micelle swelling approach, yielded hybrids with an enhancement factor up to 20 times. I improved the hybrids by investigating the influence of the synthesis parameters such as gold-SWNT ratio and the stirring time. An increased stirring time improved the overall emission signal of the samples. The enhancement originated from the hybridization process but does not increase with stirring time. While the total emission yield increases with the amount of tubes isolated during the stirring process, the enhancement of the luminescence of the single tube depends on the plasmonic features of the metallic particles and remains constant during the stirring process.

Another important finding was the influence of the plasmon resonance on the enhancement factor, which I showed in a plasmon resonance study. I analysed the interplay between the fine tuned plasmon resonances and the plasmon assisted enhancement of carbon nanotubes. The discrete transition energies of SWNTs enabled to separately address the excitation and emission of the tubes. We tailored the plasmonic particles to scan the wavelength range between approx. 500-1000 nm. We achieved the strongest enhancement for SPRs redshifted with respect to the absorbance of the SWNTs. For SPR coinciding with the emission of the tubes, we observed strong quenching of the tubes emission. This provides the guidelines for rationally engineering hybrid metal-semiconductor nano-systems with targeted enhanced optical response.
Two-colour pump-probe measurements monitored the decay dynamics of carbon nanotubes in the close vicinity of gold nanoparticles. Those measurements showed an overall increase in the de-excitation dynamics due to the metal proximity. The emission-enhancement of the π-hybrids is mainly driven by the stronger pumping through the localized plasmonic near-field rather than by the additional de-excitation pathways due to the metal presence. These findings provide a guide for efficient fabrication of enhanced π-hybrids and stimulate further studies of the microscopic mechanisms behind the near-field interactions. To fully exploit the enhancement potential of the SWNTs, one needs to resort to a rational design of tailored metallic nanoparticles with increased intensity of the near fields localized around them. Structures with more singular morphologies - such as pyramids or nanostars - are promising candidates in this regard.

At last we were able to successfully alter the triazine covalently functionalized SWNTs and realize the attachment of metallic nanoparticles via the new implementation of the [2+1]

cycloaddition. We eliminated the problem of the micelle swelling approach, the fragility of the hybrids when transferring onto substrates. Furthermore, we could show an enhanced emission of the gold functionalized tubes. The reached enhancement factor does not meet the highest achieved enhancement of the micelle swelling samples. However, it gives a promising trend towards the potential of this approach. There are still many parameter which can be tuned in order to increase the enhancement factor and will be object to future investigations

The micelle swelling method gave us the opportunity to investigate several physical aspects of the interaction between plasmonic nanoparticles and SWNTs, their instability, however, could be an obstacle for future applications. The covalent attachment, on the other hand, affirms a stable immobilization of the gold on the SWNTs sidewall through the covalent attachment of the thiol on the SWNTs and the strong binding affinity of thiol on metal and in particular gold surfaces. Both aspects are promising approaches to enhance the optical properties of SWNTs, making them promising candidates, e.g. for biological imaging.

In the last section I showed that plasmonic particles not only can enhance the optical properties of tubes. Furthermore, they can be used to strengthen the interaction between SWNTs and other functional moieties such as dyes or molecular switches.

8 Conclusion and Outlook

The main target of this thesis was the functionalization of SWNTs with molecular moieties to influence their optical properties. In the first part, I introduced and revised well known functionalization routines to attach moieties, highlighting the advantages and challenges of the different methods. The endohedral functionalization method ensures a stable encapsulation of the functional moiety inside of the carbon nanotube. The finite size of the tubes' inner cavity, however, limits the application of such technique to small molecules. A more versatile method is the non-covalent functionalization routine. The non-covalent techniques are successful in immobilizing the functional moieties on to the sidewalls. The moieties can attach onto the tubes through π-π-stacking, surfactants-driven processes, polymer wrapping, or the micelle swelling method. However, the forces driving this form of attachments are relatively weak, making the non-covalent functionalization rather unstable. Small environmental changes can lead to detachment of the functionalities and disruption of the systems. The covalent functionalization routine, on the contrary, ensures a strong attachment onto the tubes. On the downside, though, this approach converts a fraction of the SWNTs sp^2 carbon atoms into their sp^3 form. This irreversibly quenches the luminescence of SWNTs and is the main reason why covalent functionalization is mainly used for non-optical purposes.

One of the main achievement of this work has been the development of a new technique upholding the best from both the covalent and the non-covalent approaches. Our newly introduced nitrine-based [2+1] cycloaddition routine disproved the assumption that covalent functionalization is bound to always disrupt the optical properties of SWNTs. In our work we first proved the covalent nature of the functionalization through several, independent techniques [8]. Crossed analysis of TGA, EELS, HRTEM, and XPS spectroscopy provided proof of the efficient covalent attachment of triazine onto the tubes sidewalls. Next, we verified through Raman and PLE spectroscopy that the covalent treatment safeguarded the optical response of the tubes. In this way, we showed that the [2+1] cycloaddition functionalization of carbon nanotubes with dichloro-triazine preserves the electronic and optoelectronic properties of SWNTs. The triazine functionalized nanotubes can be used as a building block to anchor additional functionalities onto the tubes.

After the introductory part, I focused on attaching three functional components to the nanotubes while comparing the strengths and weaknesses between the non-covalent and our new covalent approach. I investigated the influence of a) the molecular dipole switch **spiropy-**

ran/merocyanine, b) the attachment of the aromatic dye **perylene**, and c) the immobilization of **gold nanoparticles** on the tubes properties.

Spiropyran. The interaction of spiropyran with nanotubes was already subject of previous theoretical and experimental investigations in the works of Malic *et al.* and Bluemmel *et al.* The theoretical calculations predicted a shift of the emission and excitation energies of the tubes due to the conformational change of the switch. No appreciable shifts have been observed in the past investigations, mainly due to the large separation between switch and anchor (0.6-1 nm). In chapter 7 I showed that the non-covalent immobilization can be realized by the micelle swelling approach, which does not require any anchors and ensures close proximity between the switch and nanotubes. I verified the validity of the theoretical predictions and observed shifts in the tubes' transition energies induced by the dipole switch. Comparing the effect of molecules with similar morphologies but different dipole moments (spiropyran vs. spiro-oxazine), I experimentally proved that the change in the excitonic energies is proportional to the magnitude of the dipole moment [9]. A comparative study of the effects of the temperature on the sample synthesis allowed the identification of the best working condition for ensuring the best coating conditions of the tubes for the highest dipole moment.
An alternative approach to the micelle swelling was the covalent attachment of spiropyran via the [2+1] cycloaddition method. Following this strategy, we could observe a suppression of the visible absorption band of merocyanine due to conjugation of the merocyanine's π-electron onto the extended conjugated network of the nanotubes. Additionally, we showed that the exposure to UV photons reversible changes in the Fermi level of the SWNTs and quenches their emission. The reversible manipulation of the optical and electronic properties of SWNTs pave the way for sophisticated optical applications [8].

In perspective for future experiments within the non-covalent framework, it would be beneficial to establish a routine that preserves the switching ability of the spiropyran and shows reversible changes in the transition energies. Other surfactant systems with bigger micelles could possibly grant less steric hindrance and more flexibility for the switch to isomerize. An alternative non-covalent possibility could be the endohedral functionalization. In tubes with big diameters (probably >1.6 nm) the switch might have the chance to undergo the isomerization process without any hindrance. Further experiments on the spiropyran attached via the [2+1] cycloaddition could give a deeper insight in the underlying mechanism and could lead to the actual implementation of the samples as light switchable ballistic transport channels.

Perylene. In the next chapter, I reported the results of our investigation of the influence of perylene on the optoelectronic properties of SWNTs. Perylene is a small aromatic dye which has been shown to form excitation-transfer complexes with SWNTs. The attachment occurred through π-π-stacking. In the investigations carried out within this thesis, perylene was incorporated into a polymer, whose wrapping around the SWNTs ensures strong and stable attachment. The hybrids we created in this way are very useful for biomedical applications. We demonstrated their cellular uptake and a significant increase of their biocompatibility.

Furthermore, we successfully proved the intracellular detection of the complexes in the 1st and 2nd optical transparency window of biological tissues. These results encourage further investigations of our polymer-perylene-complexes for multipurpose biomedical applications. For example, targeted drug release in cancerous cells could be achieved by inserting drugs into the hollow structure of the tubes and attaching receptors to the polymer to make them bind to specific cells [10].
We also covalently attached perylene onto the SWNTs sidewalls. 2D excitation-emission spectroscopy revealed Förster energy transfer between the perylene and the tubes. The perylene-mediated energy transfer efficiency was around 50% in agreement with the theoretical expectation of the calculated efficiency. The energy transfer efficiency is ruled by structural factors as the perylene coverage or the alignment between the dipole moments of perylene and tubes. While higher degrees of coverage can be achieved by fine-tuning the synthetic conditions of the hybrids, a major increase of the overall efficiency of the excitation transfer will require a careful redesign of the linking geometrical configuration to be pursued in future experiments.

Plasmonic gold particles. In the last section, I observed the influence of plasmonic gold nanoparticles on the luminescence intensity of the tubes. Via the micelle swelling approach I could show that the close proximity to gold lead to an enhanced signal of the SWNTs [11]. I showed that increasing the preparation time does not improve the value of the enhancement per tube but it rather ensures the creation of bigger and bigger amount of hybrids [12]. Changes of the spectral position of the plasmonic resonance affects the value of the enhancement factor. Metallic nanoparticles with plasmon resonance redshifted with respect to the absorption of the tubes showed the highest enhancement factor, whereas overlap with the plasmon resonances with the emission energies of the tubes lead to photoluminescence quenching. By pump-probe transient-absorption spectroscopy we monitored the lifetimes of the plasmonic hybrids and showed that the stronger pumping due to the localized plasmonic near-field actually drives the enhancement of the tubes emission [13].
The attachment of gold particles through an amine-based variation of the [2+1] cycloaddition yielded SWNTs with enhanced emission as well. The covalently bound SWNT-Au hybrids are very stable and outlast the transfer from one environment to another. While these experiments are a valid proof-of-principle of the validity of our hybrids, further experiments need to be performed to fully characterize and comprehend these complexes. Moreover, attaching varying particles with different plasmonic features would offer an insight into the physical mechanisms setting on within the samples [8].

At the end I gave a outlook how the combination of two functional moieties such as gold and molecular switches or gold nanoparticles and dyes lead to an even superior tailoring of the tubes optoelectronic properties [191].

In summary, in my thesis I developed several advanced functionalization strategies of SWNTs. I compared non-covalent routines to the new covalent cycloaddition we developed and investi-

gated their effect on the fundamental properties of the complexes. I demonstrated that the attachment of varying functional moieties affects the optical properties of SWNTs in different ways. Not only the functionality attached but also the attachment procedure itself have a crucial impact on the optoelectronic properties of the final products. Furthermore, are the attachment procedures numerous and lead to different results. Especially the [2+1] cycloaddition allows a wide variety for rigid attachment of all kinds of entities to the tubes sidewalls. The potentials of the different functionalization routines are not even close to be fully utilized. The toolbox of molecular moieties ranges from dyes to switches, plasmonic to magnetic nanoparticles, and beyond. They can be immobilized by oneself or in the presence of another functionality leading to different influences on the optical properties of the SWNTs.

Appendix

Determination of the Parameters needed to Calculate the Förster Radius

SWNT Concentration

The calculation is based on Ref. [148] and gives an approximation of the SWNT concentration in the SWNT sample used for calculating the Förster radius. The specific surface of a SWNT can be observed as one side of a graphene sheet (1315m^2/g). The weight of a SWNT now can be calculated by considering the length (l) and diameter (d) of the specific tube.

$$W = \frac{1}{1315} d \cdot l \cdot \pi,$$

In our case we used (6,5) enriched CoMoCats tubes. The average length is specified as 1μm and the diameter of the (6,5) is 0.747nm.

$$W = \frac{1}{1315 m^2/g} \cdot 0.74 \cdot 10^{-9} m \cdot 10^{-6} m \cdot \pi = 1.78 \cdot 10^{-18} g$$

The volume of the sample was 1ml of 0.1g/L SWNTs, resulting in 0.1mg SWNTs. 41% of the 0.1 mg were (6,5) tubes reducing the observed SWNTs content to 0.041mg. Dividing the weight of the SWNT content by the weight of one SWNT results in the total number of SWNTs in the sample.

$$N = \frac{4.1 \cdot 10^{-3} g}{1.78 \cdot 10^{-18} g} = 2.30 \cdot 10^{15}$$

By dividing through the Avogadro constant the amount of substance can be calculated.

$$n = \frac{N}{N_A} = 3.82 \cdot 10^{-9} mol$$

In order to get the final concentration n needs to be divided by the volume of the sample.

$$c = \frac{n}{V} = 3.82 \cdot 10^{-6} mol/L$$

The concentration in order to calculate the Förster radius is c=3.82·$10^{-6} mol/L$.

Tube-Perylene Separation

The triazine can be attached to the SWNTs sidewall in three configurations leading to different orientations of the triazine and respectively also for the perylene. The possible angels are 27°, 33° and 87° and stem from the different C-C bond orientation towards the SWNT axis. In order to calculate the shortest distance for those angles from the tube centre to the perylene centre various distances need to be calculated. In a first step the distance **a** is acquired. This is the distance between the tube and the perylene centre and can be used as an approximation for the angle of 87°. In order to obtain **a** different distances were defined. **c** is the vertical distance between the perylene and the tubes and is composed of (c_1+c_2+c_3) as seen in Fig. A. c_1 is half the tubes diameter c_2 is the distance between the tubes surface and the beginning of linker connecting the triazine and the perylene.To obtain c_3 distance **z** needs to be determined. This distance could be acquired with the help of the software ChemDraw. The angle α can be won out of the symmetry of the benzol ring. Knowing those number we can calculate c_3, resulting in the value of **c**:

$$c = c_1 + c_2 + sin(30)z = 1.345nm$$

Next distance **b** is calculated:

$$b = cos(30) + z = 1.117nm.$$

Finally, **a** can be obtained:

$$a = \sqrt{b^2 + c^2} = 1.74nm.$$

As the other to orientations are not around aligned in a right angle to the tube surface further geometrical consideration need to be performed.

$$e_{27°} = \frac{b}{\cos(\alpha)} = 1.25nm$$

$$d_{27°} = \sqrt{e^2 - b2} = 0.57nm$$

$$f_{27°} = \sqrt{c^2 + d^2} = 1.47nm$$

$$e_{33°} = \frac{b}{\cos(\alpha)} = 1.32nm$$

$$d_{33°} = \sqrt{e^2 - b2} = 0.72nm$$

$$f_{33°} = \sqrt{c^2 + d^2} = 1.53nm$$

The mean value for donor-acceptor distance r is thus 1.58nm and can be used to calculate the the expected energy transfer efficiency.

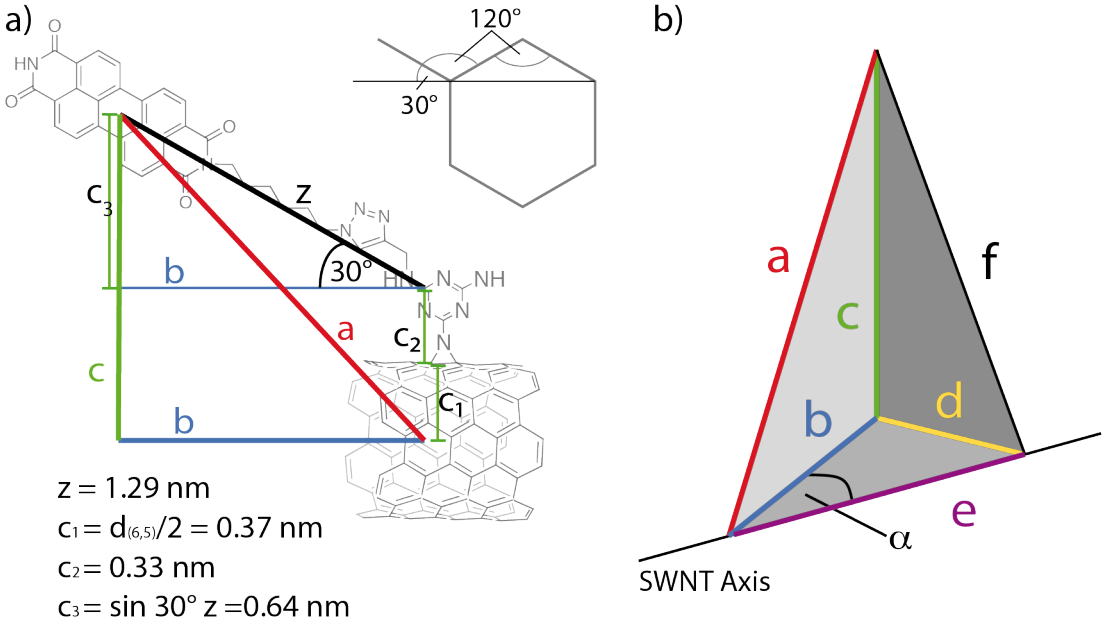

Fig. A a) Sketch of the covalent functionalized perylene-SWNTs in order to calculate the distance between the tube and the perylene. b) Spatial consideration to calculate the shortest tube dye distance.

Zusammenfassung

Die Funktionalisierung von Kohlenstoffnanoröhren (CNTs) ist ein aktuelles und aktiv erforschtes Teilgebiet der Nanotechnologie. Die Anbringung von funktionellen Einheiten beeinflusst die physikalischen Eigenschaften der Röhren und ermöglicht die Entwicklung von neuen Technologien. Die Funktionalisierung von CNTs wird in drei verschiedene Ansätze unterteilt: Endohedrale, kovalente und nicht kovalente Funktionalisierung. Alle drei Methoden weisen spezifische Vor- und Nachteile auf und werden zu Beginn der Arbeit eingeführt und analysiert.

Im ersten Teil der Arbeit wird ein neuer kovalenter Funktionalisierungsansatz vorgestellt - die nitrinbasierte [2+1] - Cycloaddition. Dieser Ansatz ermöglicht eine feste, kovalente Verankerung von molekularen Funktionalitäten, ohne das π-Netzwerk zu zerstören oder die optoelektronischen Eigenschaften von CNTs zu schwächen. Diese neue Methode kann als variable Plattform für die Funktionalisierung und gezielte Manipulation der physikalischen Eigenschaften von CNTs genutzt werden.

Im zweiten Teil der Arbeit werden bekannte Funktionalisierungsmethoden mit der neu eingeführten [2+1] - Cycloaddition verglichen. Hierfür wurden drei verschiedene funktionelle Gruppen ausgewählt und deren Einfluss auf die optischen Eigenschaften der Röhren untersucht: Der Dipolschalter **Spiropyran**, der molekulare Farbstoff **Perylen** und **Gold Nanopartikel**.

Die vergleichende Studie zwischen kovalenten und nicht-kovalenten Funktionalisierungsmethoden zeigt, dass nicht nur die ausgewählte funktionale Gruppen einen starken Einfluss auf die optischen Eigenschaften der Röhren hat. Auch die Verankerungsmethode hat einen direkten Effekt auf die resultierenden physikalischen Eigenschaften der CNTs.

Publications

1. Nanoplasmonic Colloidal Suspensions for the Enhancement of the Luminescent Emission from Single-Walled Carbon Nanotubes
   M. Glaeske and A. Setaro
   Nano Research, Springer, 2013, 6, 593-601

2. Optimization of the Nanoplasmonic Hybridization Process for the Enhancement of the Optical Response of Single-Walled Carbon Nanotubes
   S. Vaitiekenas, M. Glaeske and A. Setaro
   Photonics Technologies, 2014 Fotonica AEIT Italian Conference on, 2014, 1-3

3. Effect of Hybrid Isolation on the Luminescence Enhancement of Carbon Nanotube - Gold Nanorod Composites
   M. Glaeske and A. Setaro
   physica status solidi (b), Wiley Online Library, 2014, 251, 2480-2484

4. Chiral selectivity of polyglycerol-based amphiphiles incorporating different aromatic cores
   A. Setaro, C. S. Popeney, M. Witt, P. Bluemmel, M. Glaeske, R. Haag and S. Reich
   physica status solidi (b), Wiley Online Library, 2015, 252, 2536-2540

5. Doping in Covalently Functionalized Carbon Nanotubes: A Raman Scattering Study
   G. Gordeev, A. Setaro, M. Glaeske, S. Juergensen and S. Reich
   physica status solidi (b), Wiley Online Library, 2016, 253, 2461-2467

6. Preserving π-Conjugation in Covalently Functionalized Carbon Nanotubes for Optoelectronic Applications
   A. Setaro, M. Adeli, M. Glaeske, D. Przyrembel, T. Bisswanger, G. Gordeev, F. Maschietto, A. Faghani, B. Paulus, M. Weinelt, R. Arenal, R. Haag and S. Reich
   Nature Communications, Nature Publishing Group, 2017, 8

7. Relaxation Lifetimes of Plasmonically Enhanced Hybrid Gold-Carbon Nanotubes Systems.
   M. Glaeske, M. Kumar, T. Bisswanger, S. Vaitiekenas, C. Soci, R. Narula, A. Bruno and A. Setaro
   Nanotechnology, 2017, 28, 255202

8. Dipole-Switch Induced Modification of the Emissive Response of Carbon Nanotubes
   M. Glaeske, P. Bluemmel, S. Juergensen, A. Setaro and S. Reich
   Journal of Physics: Condensed Matter, IOP Publishing, 2017

9. Controlling the Decoration of the Reduced Graphene Oxide Surface with Pyrene-Functionalized Gold Nanoparticles
   L. Gabrielli, G. Altoè, M. Glaeske, S. Juergensen, S. Reich, A. Setaro, E. Menna, F. Mancin and T. Gatti
   physica status solidi (b), Wiley Online Library, 2017, 254, 1700281

10. Fluorescent Polymer-Single-Walled Carbon Nanotube Complexes with Charged and Non-charged Dendronized Perylene Bisimides for Bioimaging Studies
    K. Huth, M. Glaeske, K. Achazi, G. Gordeev, S. Kumar, R. Arenal, S. K. Sharma, M. Adeli, A. Setaro, S. Reich and R. Haag
    Small, Wiley Online Library, 2018, 1800796

Acknowledgements

The last years at the AG Reich have been a period of intense learning for me, not only in the scientific area, but also on a personal level. I went through difficult phases with slow progress and sections with astonishing and exciting results. In both, good and bad, times many people had been at my side, contributing to this work or supporting me otherwise.
I want to use this opportunity to thank...

... Stephanie Reich for the encouragement and support through this thesis. Since I joined the AG Reich I had the freedom to explore the world of carbon nanotubes. I was given the opportunity to pursue the topics and experiments of my interest. I was not only given the change to explore the scientific world but also attend conference around the world. I am happy I enrolled in your seminar back in 2009, discovered the world of carbon nanotubes, and became part of the AG Reich. I will always remember the outstanding time I had in your group and the opportunities I was given.

... Antonio who was a major help during my thesis. He was always [after 12 pm ;)] available whenever I ran into a trouble spot or had a question about my research or writing. He steered me in the right direction whenever he thought I needed it and always supported me with multiple Mathematica problems I encountered. He encouraged me to attend conferences and present my work. I am thankful for the support you provided during the last years.

... Rainer Haag for being my second supervisor and the collaboration with the AG Haag during my thesis.

... Mohsen Adeli for establishing the concept of the [2+1] cycloaddition. Without this approach the thesis would not have been possible in its current form.

... Katharina Huth for the synthesis of the perylene compounds and the collaborations on the perylene projects.

... the other collaboration partner who made this work possible: Katharina Achazi, Ivgen Donski and Abbas Faghani from the AG Haag for the collaboration on the perylene projects.

Daniel Przyrembel and Martin Weinelt for the XPS measurements of the covalent samples. Federica Maschietto and Beate Paulus for the quantum chemical calculations. Raul Arenal for the EELS and HRTEM measurements. Timo Bisswanger for synthesizing the gold nanoparticles. Manoj Kumar and Anna Lisa Bruno for the time resolved spectroscopy measurements and the hospitality during our stay in Singapur.

... the members and former members of AG Reich for all the good work and all the fun times, in particular Kati, Benni, Basti, Pascal, Patryk, Sole, Sabrina, Georgy, Sören, Gudrun, Martin, Vladka, André, Anna, Izabela, Katharina, Niclas, Valerio...

... Kika for her friendship in the past years, for becoming Luises godmother and the opportunity to work again with her and being part of this new exciting chapter.

... my friends who supported me during the last years and especially last months with encouraging words.

Finally, I must express my very profound gratitude to my family and to Flo for providing me with unfailing support and continuous encouragement throughout my years of study and through the process of researching and writing this thesis. This accomplishment would not have been possible without them.
Thank you.

Bibliography

[1] I. Firkowska, A. Boden, A.-M. Vogt, and S. Reich. „Tailoring the contact thermal resistance at metal–carbon nanotube interface“. In: *physica status solidi (b)* 248.11 (2011), pp. 2520–2523 (cit. on pp. 1, 25).

[2] N. M. Pugno. „On the strength of the carbon nanotube-based space elevator cable: from nanomechanics to megamechanics“. In: *Journal of Physics: Condensed Matter* 18.33 (2006), S1971 (cit. on p. 1).

[3] M. F. De Volder, S. H. Tawfick, R. H. Baughman, and A. J. Hart. „Carbon nanotubes: present and future commercial applications“. In: *science* 339.6119 (2013), pp. 535–539 (cit. on p. 1).

[4] Q. Cao, J. Tersoff, D. B. Farmer, Y. Zhu, and S.-J. Han. „Carbon nanotube transistors scaled to a 40-nanometer footprint“. In: *Science* 356.6345 (2017), pp. 1369–1372 (cit. on p. 1).

[5] M. M. Shulaker, G. Hills, N. Patil, et al. „Carbon nanotube computer“. In: *Nature* 501.7468 (2013), pp. 526–530 (cit. on p. 1).

[6] S. Beg, M. Rizwan, A. M. Sheikh, et al. „Advancement in carbon nanotubes: basics, biomedical applications and toxicity“. In: *Journal of pharmacy and pharmacology* 63.2 (2011), pp. 141–163 (cit. on pp. 1, 63).

[7] K. Welsher, Z. Liu, S. P. Sherlock, et al. „A route to brightly fluorescent carbon nanotubes for near-infrared imaging in mice“. In: *Nature nanotechnology* 4.11 (2009), pp. 773–780 (cit. on pp. 1, 40, 63, 77).

[8] A. Setaro, M. Adeli, M. Glaeske, et al. „Preserving π-conjugation in covalently functionalized carbon nanotubes for optoelectronic applications“. In: *Nature Communications* 8 (2017) (cit. on pp. 1, 2, 30, 31, 35, 36, 43, 53, 69, 78, 92, 95, 103–105).

[9] M. Gläske, P. Bluemmel, S. Juergensen, A. Setaro, and S. Reich. „Dipole-switch induced modification of the emissive response of carbon nanotubes“. In: *Journal of Physics: Condensed Matter* (2017) (cit. on pp. 2, 23, 43, 104).

[10] K. Huth, T. Heek, K. Achazi, et al. „Noncharged and Charged Monodendronised Perylene Bisimides as Highly Fluorescent Labels and their Bioconjugates“. In: *Chemistry-A European Journal* 23.20 (2017), pp. 4849–4862 (cit. on pp. 2, 63, 64, 69, 105).

[11] M. Glaeske and A. Setaro. „Nanoplasmonic colloidal suspensions for the enhancement of the luminescent emission from single-walled carbon nanotubes“. In: *Nano Research* 6.8 (2013), pp. 593–601 (cit. on pp. 2, 63, 77, 78, 82, 83, 86, 87, 105).

[12] M. Glaeske and A. Setaro. „Effect of hybrid isolation on the luminescence enhancement of carbon nanotube–gold nanorod composites“. In: *physica status solidi (b)* 251.12 (2014), pp. 2480–2484 (cit. on pp. 2, 78, 83, 87, 105).

[13] M. Glaeske, M. Kumar, T. Bisswanger, et al. „Relaxation Lifetimes of Plasmonically Enhanced Hybrid Gold-Carbon Nanotubes Systems.“ In: *Nanotechnology* 28.255202 (2017), p. 255202 (cit. on pp. 3, 78, 105).

[14] S. Iijima. „Helical microtubules of graphitic carbon“. In: *nature* 354.6348 (1991), p. 56 (cit. on p. 5).

[15] S. Iijima and T. Ichihashi. „Single-shell carbon nanotubes of 1-nm diameter“. In: *nature* 363.6430 (1993), pp. 603–605 (cit. on p. 5).

[16] R. Saito, G. Dresselhaus, and M. S. Dresselhaus. *Physical properties of carbon nanotubes*. World scientific, 1998 (cit. on p. 6).

[17] P. Blümmel. „Functionalization of Carbon Nanotubes with Molecular Switches“. PhD thesis. Freie Universität Berlin, 2013 (cit. on pp. 7, 10, 13, 43, 44).

[18] S. Reich, C. Thomsen, and J. Maultzsch. *Carbon nanotubes: basic concepts and physical properties*. John Wiley & Sons, 2008 (cit. on pp. 9, 36).

[19] A. H. C. Neto, F. Guinea, N. M. Peres, K. S. Novoselov, and A. K. Geim. „The electronic properties of graphene“. In: *Reviews of modern physics* 81.1 (2009), p. 109 (cit. on p. 9).

[20] R. R. Nair, P. Blake, A. N. Grigorenko, et al. „Fine structure constant defines visual transparency of graphene“. In: *Science* 320.5881 (2008), pp. 1308–1308 (cit. on p. 9).

[21] A. Setaro. „Advanced carbon nanotubes functionalization“. In: *Journal of Physics: Condensed Matter* 29.42 (2017), p. 423003 (cit. on pp. 11, 12).

[22] H. Kataura, Y Kumazawa, Y Maniwa, et al. „Optical properties of single-wall carbon nanotubes“. In: *Synthetic metals* 103.1-3 (1999), pp. 2555–2558 (cit. on p. 11).

[23] M. J. O'connell, S. M. Bachilo, C. B. Huffman, et al. „Band gap fluorescence from individual single-walled carbon nanotubes“. In: *Science* 297.5581 (2002), pp. 593–596 (cit. on p. 11).

[24] J. Mintmire and C. White. „Universal density of states for carbon nanotubes“. In: *Physical Review Letters* 81.12 (1998), p. 2506 (cit. on p. 11).

[25] J Maultzsch, R Pomraenke, S Reich, et al. „Exciton binding energies in carbon nanotubes from two-photon photoluminescence“. In: *Physical Review B* 72.24 (2005), p. 241402 (cit. on p. 12).

[26] Y. Ohno, S. Maruyama, and T. Mizutani. „Environmental effects on photoluminescence of single-walled carbon nanotubes“. In: *Carbon Nanotubes*. InTech, 2010 (cit. on p. 12).

[27] C. D. Spataru, S. Ismail-Beigi, L. X. Benedict, and S. G. Louie. „Excitonic effects and optical spectra of single-walled carbon nanotubes“. In: *Physical Review Letters* 92.7 (2004), p. 077402 (cit. on p. 13).

[28] F. Wang, G. Dukovic, L. E. Brus, and T. F. Heinz. „The optical resonances in carbon nanotubes arise from excitons“. In: *Science* 308.5723 (2005), pp. 838–841 (cit. on p. 13).

[29] J. H. Choi and M. S. Strano. „Solvatochromism in single-walled carbon nanotubes“. In: *Applied Physics Letters* 90.22 (2007), p. 223114 (cit. on pp. 14, 51).

[30] S. Berger, F. Iglésias, P. Bonnet, et al. „Optical properties of carbon nanotubes in a composite material: The role of dielectric screening and thermal expansion“. In: *Journal of Applied Physics* 105.9 (2009), p. 094323 (cit. on p. 15).

[31] A. Hirsch and O. Vostrowsky. „Functionalization of carbon nanotubes“. In: *Functional molecular nanostructures*. Springer, 2005, pp. 193–237 (cit. on pp. 15, 16).

[32] F. Hauke and A. Hirsch. „Covalent functionalization of carbon nanotubes“. In: *Carbon Nanotubes and Related Structures: Synthesis, Characterization, Functionalization, and Applications* (2010), pp. 135–198 (cit. on pp. 16, 24).

[33] R. Haddon, L. Brus, and K. Raghavachari. „Rehybridization and π-orbital alignment: the key to the existence of spheroidal carbon clusters“. In: *Chemical physics letters* 131.3 (1986), pp. 165–169 (cit. on p. 16).

[34] S. Park, D. Srivastava, and K. Cho. „Generalized chemical reactivity of curved surfaces: carbon nanotubes“. In: *Nano letters* 3.9 (2003), pp. 1273–1277 (cit. on p. 16).

[35] T. Dinadayalane and J. Leszczynski. „Remarkable diversity of carbon–carbon bonds: structures and properties of fullerenes, carbon nanotubes, and graphene“. In: *Structural Chemistry* 21.6 (2010), pp. 1155–1169 (cit. on p. 16).

[36] L. Girifalco, M. Hodak, and R. S. Lee. „Carbon nanotubes, buckyballs, ropes, and a universal graphitic potential“. In: *Physical Review B* 62.19 (2000), p. 13104 (cit. on p. 17).

[37] L. Vaisman, H. D. Wagner, and G. Marom. „The role of surfactants in dispersion of carbon nanotubes“. In: *Advances in colloid and interface science* 128 (2006), pp. 37–46 (cit. on p. 17).

[38] A. Thess, R. Lee, P. Nikolaev, et al. „Crystalline ropes of metallic carbon nanotubes“. In: *Science* (1996), pp. 483–487 (cit. on p. 17).

[39] D. M. Guldi and N. Martín. *Carbon nanotubes and related structures: synthesis, characterization, functionalization, and applications*. John Wiley & Sons, 2010 (cit. on pp. 20, 22).

[40] S. Cambré, J. Campo, C. Beirnaert, et al. „Asymmetric dyes align inside carbon nanotubes to yield a large nonlinear optical response“. In: *Nature nanotechnology* 10.3 (2015), pp. 248–252 (cit. on p. 20).

[41] D. E. Luzzi and B. W. Smith. „Carbon cage structures in single wall carbon nanotubes: a new class of materials“. In: *Carbon* 38.11 (2000), pp. 1751–1756 (cit. on p. 20).

[42] S. Y. Hong, G. Tobias, K. T. Al-Jamal, et al. „Filled and glycosylated carbon nanotubes for in vivo radioemitter localization and imaging“. In: *Nature materials* 9.6 (2010), p. 485 (cit. on p. 20).

[43] L. Shao, G. Tobias, Y. Huh, and M. L. Green. „Reversible filling of single walled carbon nanotubes opened by alkali hydroxides“. In: *Carbon* 44.13 (2006), pp. 2855–2858 (cit. on p. 20).

[44] K. Holmberg, B. Jönsson, B. Kronberg, and B. Lindman. *Surfactants and polymers in aqueous solution*. Wiley Online Library, 2002 (cit. on p. 21).

[45] B. Trappmann, K. Ludwig, M. R. Radowski, et al. „A new family of nonionic dendritic amphiphiles displaying unexpected packing parameters in micellar assemblies“. In: *Journal of the American Chemical Society* 132.32 (2010), pp. 11119–11124 (cit. on p. 21).

[46] W. Wenseleers, I. I. Vlasov, E. Goovaerts, et al. „Efficient Isolation and Solubilization of Pristine Single-Walled Nanotubes in Bile Salt Micelles“. In: *Advanced Functional Materials* 14.11 (2004), pp. 1105–1112 (cit. on pp. 21, 84).

[47] S.-Y. Ju, J. Doll, I. Sharma, and F. Papadimitrakopoulos. „Selection of carbon nanotubes with specific chiralities using helical assemblies of flavin mononucleotide“. In: *Nature nanotechnology* 3.6 (2008), pp. 356–362 (cit. on p. 21).

[48] R. Marquis, C. Greco, I. Sadokierska, et al. „Supramolecular discrimination of carbon nanotubes according to their helicity“. In: *Nano letters* 8.7 (2008), pp. 1830–1835 (cit. on p. 21).

[49] A. Setaro, C. S. Popeney, M. Witt, et al. „Chiral selectivity of polyglycerol-based amphiphiles incorporating different aromatic cores“. In: *physica status solidi (b)* 252.11 (2015), pp. 2536–2540 (cit. on pp. 21, 51).

[50] S. Ghosh, S. M. Bachilo, and R. B. Weisman. „Advanced sorting of single-walled carbon nanotubes by nonlinear density-gradient ultracentrifugation“. In: *Nature nanotechnology* 5.6 (2010), pp. 443–450 (cit. on pp. 21, 57).

[51] F. Ernst, T. Heek, A. Setaro, R. Haag, and S. Reich. „Energy Transfer in Nanotube-Perylene Complexes“. In: *Advanced functional materials* 22.18 (2012), pp. 3921–3926 (cit. on pp. 21, 58, 62, 77).

[52] R. J. Chen, Y. Zhang, D. Wang, and H. Dai. „Noncovalent sidewall functionalization of single-walled carbon nanotubes for protein immobilization“. In: *Journal of the American Chemical Society* 123.16 (2001), pp. 3838–3839 (cit. on p. 22).

[53] N. Nakashima, Y. Tomonari, and H. Murakami. „Water-soluble single-walled carbon nanotubes via noncovalent sidewall-functionalization with a pyrene-carrying ammonium ion“. In: *Chemistry Letters* 31.6 (2002), pp. 638–639 (cit. on p. 22).

[54] P. Bluemmel, A. Setaro, C. Maity, S. Hecht, and S. Reich. „Designing a spiropyran-based molecular switch for carbon nanotube functionalization: Influence of anchor groups and tube–switch separation“. In: *physica status solidi (b)* 249.12 (2012), pp. 2479–2482 (cit. on pp. 22, 45, 46).

[55] R. K. Wang, W.-C. Chen, D. K. Campos, and K. J. Ziegler. „Swelling the micelle core surrounding single-walled carbon nanotubes with water-immiscible organic solvents“. In: *Journal of the American Chemical Society* 130.48 (2008), pp. 16330–16337 (cit. on pp. 22, 45).

[56] C. Roquelet, J.-S. Lauret, V. Alain-Rizzo, et al. „Π-Stacking Functionalization of Carbon Nanotubes through Micelle Swelling“. In: *ChemPhysChem* 11.8 (2010), pp. 1667–1672 (cit. on pp. 22, 58).

[57] S. K. Kreft, M. Å. Petersen, M. B. Nielsen, S. Reich, and A. Setaro. „Isomerization of orthogonal molecular switches encapsulated within micelles solubilizing carbon nanotubes“. In: *The Journal of Physical Chemistry C* 119.27 (2015), pp. 15731–15734 (cit. on pp. 22, 48).

[58] G. Clave, G. Delport, C. Roquelet, et al. „Functionalization of carbon nanotubes through polymerization in micelles: A bridge between the covalent and noncovalent methods“. In: *Chemistry of Materials* 25.13 (2013), pp. 2700–2707 (cit. on p. 22).

[59] U. Gedde. *Polymer physics*. Springer Science & Business Media, 2013 (cit. on p. 23).

[60] A. Nish, J.-Y. Hwang, J. Doig, and R. J. Nicholas. „Highly selective dispersion of single-walled carbon nanotubes using aromatic polymers“. In: *Nature nanotechnology* 2.10 (2007), pp. 640–646 (cit. on pp. 23, 64).

[61] M. J. O'Connell, P. Boul, L. M. Ericson, et al. „Reversible water-solubilization of single-walled carbon nanotubes by polymer wrapping“. In: *Chemical physics letters* 342.3 (2001), pp. 265–271 (cit. on pp. 23, 61).

[62] J. N. Coleman, U. Khan, W. J. Blau, and Y. K. Gun'ko. „Small but strong: a review of the mechanical properties of carbon nanotube–polymer composites". In: *Carbon* 44.9 (2006), pp. 1624–1652 (cit. on p. 24).

[63] T. Fujigaya and N. Nakashima. „Non-covalent polymer wrapping of carbon nanotubes and the role of wrapped polymers as functional dispersants". In: *Science and technology of advanced materials* 16.2 (2015), p. 024802 (cit. on p. 24).

[64] L. Cognet, D. A. Tsyboulski, J.-D. R. Rocha, et al. „Stepwise quenching of exciton fluorescence in carbon nanotubes by single-molecule reactions". In: *Science* 316.5830 (2007), pp. 1465–1468 (cit. on pp. 24, 28).

[65] A. Hirsch. „Functionalization of single-walled carbon nanotubes". In: *Angewandte Chemie International Edition* 41.11 (2002), pp. 1853–1859 (cit. on p. 24).

[66] G. Gordeev, A. Setaro, M. Glaeske, S. Jürgensen, and S. Reich. „Doping in covalently functionalized carbon nanotubes: A Raman scattering study". In: *physica status solidi (b)* 253.12 (2016), pp. 2461–2467 (cit. on pp. 25, 27, 28).

[67] C. A. Dyke and J. M. Tour. „Covalent functionalization of single-walled carbon nanotubes for materials applications". In: *The Journal of Physical Chemistry A* 108.51 (2004), pp. 11151–11159 (cit. on p. 25).

[68] W. Yang, P. Thordarson, J. J. Gooding, S. P. Ringer, and F. Braet. „Carbon nanotubes for biological and biomedical applications". In: *Nanotechnology* 18.41 (2007), p. 412001 (cit. on p. 25).

[69] N. W. Shi Kam, T. C. Jessop, P. A. Wender, and H. Dai. „Nanotube molecular transporters: internalization of carbon nanotube- protein conjugates into mammalian cells". In: *Journal of the American Chemical Society* 126.22 (2004), pp. 6850–6851 (cit. on p. 25).

[70] R. Yu, L. Chen, Q. Liu, et al. „Platinum deposition on carbon nanotubes via chemical modification". In: *Chemistry of Materials* 10.3 (1998), pp. 718–722 (cit. on pp. 27, 97).

[71] Y. Piao, B. Meany, L. R. Powell, et al. „Brightening of carbon nanotube photoluminescence through the incorporation of sp3 defects". In: *Nature chemistry* 5.10 (2013), pp. 840–845 (cit. on p. 29).

[72] Y. Miyauchi, M. Iwamura, S. Mouri, et al. „Brightening of excitons in carbon nanotubes on dimensionality modification". In: *Nature Photonics* 7.9 (2013), pp. 715–719 (cit. on p. 29).

[73] W. Reusch. *Alkene Reactivity*. 2009 (cit. on p. 29).

[74] Y.-S. Lee and N. Marzari. „Cycloaddition functionalizations to preserve or control the conductance of carbon nanotubes". In: *Physical review letters* 97.11 (2006), p. 116801 (cit. on pp. 29, 30).

[75] I. Kumar, S. Rana, and J. W. Cho. „Cycloaddition reactions: a controlled approach for carbon nanotube functionalization". In: *Chemistry-A European Journal* 17.40 (2011), pp. 11092–11101 (cit. on p. 29).

[76] C. Liu, Q. Zhang, F. Stellacci, et al. „Carbene-Functionalized Single-Walled Carbon Nanotubes and Their Electrical Properties". In: *Small* 7.9 (2011), pp. 1257–1263 (cit. on p. 30).

[77] R. F. Egerton. *Electron energy-loss spectroscopy in the electron microscope*. Springer Science & Business Media, 2011 (cit. on p. 32).

[78] J. Cervenka, A. Budi, N. Dontschuk, et al. „Graphene field effect transistor as a probe of electronic structure and charge transfer at organic molecule–graphene interfaces". In: *Nanoscale* 7.4 (2015), pp. 1471–1478 (cit. on p. 39).

[79] B. Hatting, S. Heeg, K. Ataka, et al. „Fermi energy shift in deposited metallic nanotubes: A Raman scattering study“. In: *Physical Review B* 87.16 (2013), p. 165442 (cit. on p. 40).

[80] M. Natali and S. Giordani. „Molecular switches as photocontrollable “smart” receptors“. In: *Chemical Society Reviews* 41.10 (2012), pp. 4010–4029 (cit. on p. 43).

[81] E Fischer and Y Hirshberg. „Formation of coloured forms of spirans by low-temperature irradiation“. In: *Journal of the Chemical Society* NOV (1952), pp. 4522–4524 (cit. on p. 43).

[82] F. M. Raymo, R. J. Alvarado, S. Giordani, and M. A. Cejas. „Memory effects based on intermolecular photoinduced proton transfer“. In: *Journal of the American Chemical Society* 125.8 (2003), pp. 2361–2364 (cit. on p. 43).

[83] C. Kördel, A. Setaro, P. Bluemmel, et al. „Controlled reversible debundling of single-walled carbon nanotubes by photo-switchable dendritic surfactants“. In: *Nanoscale* 4.10 (2012), pp. 3029–3031 (cit. on pp. 43, 45).

[84] P. Bluemmel, A. Setaro, C. S. Popeney, R. Haag, and S. Reich. „Dispersion of carbon nanotubes using an azobenzene derivative“. In: *physica status solidi (b)* 247.11-12 (2010), pp. 2891–2894 (cit. on p. 43).

[85] M. Del Valle, R. Gutiérrez, C. Tejedor, and G. Cuniberti. „Tuning the conductance of a molecular switch“. In: *Nature nanotechnology* 2.3 (2007), pp. 176–179 (cit. on p. 44).

[86] I. A. Banerjee, L. Yu, and H. Matsui. „Application of host- guest chemistry in nanotube-based device fabrication: Photochemically controlled immobilization of azobenzene nanotubes on patterned α-CD monolayer/Au substrates via molecular recognition“. In: *Journal of the American Chemical Society* 125.32 (2003), pp. 9542–9543 (cit. on p. 44).

[87] A. M. Kolpak and J. C. Grossman. „Azobenzene-functionalized carbon nanotubes as high-energy density solar thermal fuels“. In: *Nano letters* 11.8 (2011), pp. 3156–3162 (cit. on p. 44).

[88] R. Klajn. „Spiropyran-based dynamic materials“. In: *Chemical Society Reviews* 43.1 (2014), pp. 148–184 (cit. on p. 44).

[89] E. Malic, A. Setaro, P. Bluemmel, et al. „Carbon nanotubes as substrates for molecular spiropyran-based switches“. In: *Journal of Physics: Condensed Matter* 24.39 (2012), p. 394006 (cit. on pp. 44, 46).

[90] E Malic, C Weber, M Richter, et al. „Microscopic model of the optical absorption of carbon nanotubes functionalized with molecular spiropyran photoswitches“. In: *Physical review letters* 106.9 (2011), p. 097401 (cit. on p. 44).

[91] A. Setaro, P. Bluemmel, C. Maity, S. Hecht, and S. Reich. „Non-Covalent Functionalization of Individual Nanotubes with Spiropyran-Based Molecular Switches“. In: *Advanced Functional Materials* 22.11 (2012), pp. 2425–2431 (cit. on pp. 45, 46).

[92] P. Blümmel, A. Setaro, C Maity, S Hecht, and S. Reich. „Tuning the interaction between carbon nanotubes and dipole switches: the influence of the change of the nanotube–spiropyran distance“. In: *Journal of Physics: Condensed Matter* 24.39 (2012), p. 394005 (cit. on pp. 45, 46, 55).

[93] P. Bluemmel, A. Setaro, C. S. Popeney, et al. „Amphiphile replacement on carbon nanotube surfaces: Effect of aromatic groups on the interaction strength“. In: *physica status solidi (b)* 248.11 (2011), pp. 2532–2535 (cit. on p. 45).

[94] Y. Matsuzawa, H. Kato, H. Ohyama, et al. „Photoinduced Dispersibility Tuning of Carbon Nanotubes by a Water-Soluble Stilbene as a Dispersant“. In: *Advanced Materials* 23.34 (2011), pp. 3922–3925 (cit. on p. 45).

[95] C. S. Popeney, A. Setaro, R.-C. Mutihac, et al. „Polyglycerol-Derived Amphiphiles for the Solubilization of Single-Walled Carbon Nanotubes in Water: A Structure–Property Study“. In: *ChemPhysChem* 13.1 (2012), pp. 203–211 (cit. on p. 45).

[96] A Setaro, C. Popeney, B Trappmann, et al. „Polyglycerol-derived amphiphiles for single walled carbon nanotube suspension“. In: *Chemical Physics Letters* 493.1 (2010), pp. 147–150 (cit. on p. 45).

[97] M. Piantek, G. Schulze, M. Koch, et al. „Reversing the thermal stability of a molecular switch on a gold surface: ring-opening reaction of nitrospiropyran“. In: *Journal of the American Chemical Society* 131.35 (2009), pp. 12729–12735 (cit. on p. 46).

[98] R. F. Khairutdinov, M. E. Itkis, and R. C. Haddon. „Light modulation of electronic transitions in semiconducting single wall carbon nanotubes“. In: *Nano Letters* 4.8 (2004), pp. 1529–1533 (cit. on p. 47).

[99] H. Zhang, X. Guo, J. Hui, et al. „Interface engineering of semiconductor/dielectric heterojunctions toward functional organic thin-film transistors“. In: *Nano letters* 11.11 (2011), pp. 4939–4946 (cit. on p. 49).

[100] R. Liu. *Water-insoluble drug formulation*. CRC press, 2008 (cit. on pp. 49, 51).

[101] A. Metelitsa, C Coudret, J. Micheau, and N. Voloshin. „Quantitative investigations of thermal and photoinduced J-and H-aggregation of hydrophobic spirooxazines in binary solvent through UV/vis spectroscopy“. In: *RSC Advances* 4.40 (2014), pp. 20974–20983 (cit. on p. 51).

[102] D Gaude, M Le Baccon, R Guglielmetti, and R Gautron. „Photochromisme de spiropyrannes. Étude de la photodégradation de dérové indoliniques substitués et polymériques“. In: *Bull. Soc. Chim. Fr* 9.10 (1979), pp. 489–498 (cit. on p. 53).

[103] M. J. O'Connell, E. E. Eibergen, and S. K. Doorn. „Chiral selectivity in the charge-transfer bleaching of single-walled carbon-nanotube spectra.“ In: *Nature materials* 4.5 (2005) (cit. on p. 55).

[104] B. Satishkumar, L. O. Brown, Y. Gao, et al. „Reversible fluorescence quenching in carbon nanotubes for biomolecular sensing“. In: *Nature Nanotechnology* 2.9 (2007), pp. 560–564 (cit. on p. 55).

[105] M. Zheng, A. Jagota, M. S. Strano, et al. „Structure-based carbon nanotube sorting by sequence-dependent DNA assembly“. In: *Science* 302.5650 (2003), pp. 1545–1548 (cit. on p. 57).

[106] M. Zheng, A. Jagota, E. D. Semke, et al. „DNA-assisted dispersion and separation of carbon nanotubes“. In: *Nature materials* 2.5 (2003), p. 338 (cit. on p. 57).

[107] R. Krupke, F. Hennrich, H. v. Löhneysen, and M. M. Kappes. „Separation of metallic from semiconducting single-walled carbon nanotubes“. In: *Science* 301.5631 (2003), pp. 344–347 (cit. on p. 57).

[108] A. A. Green and M. C. Hersam. „Nearly Single-Chirality Single-Walled Carbon Nanotubes Produced via Orthogonal Iterative Density Gradient Ultracentrifugation“. In: *Advanced Materials* 23.19 (2011), pp. 2185–2190 (cit. on p. 57).

[109] H. Liu, D. Nishide, T. Tanaka, and H. Kataura. „Large-scale single-chirality separation of single-wall carbon nanotubes by simple gel chromatography“. In: *Nature communications* 2 (2011), p. 309 (cit. on p. 57).

[110] L. Qu, R. B. Martin, W. Huang, et al. „Interactions of functionalized carbon nanotubes with tethered pyrenes in solution“. In: *The Journal of Chemical Physics* 117.17 (2002), pp. 8089–8094 (cit. on p. 58).

[111] W Feng, A Fujii, M Ozaki, and K Yoshino. „Perylene derivative sensitized multi-walled carbon nanotube thin film“. In: *Carbon* 43.12 (2005), pp. 2501–2507 (cit. on p. 58).

[112] C. Ehli, C. Oelsner, D. M. Guldi, et al. „Manipulating single-wall carbon nanotubes by chemical doping and charge transfer with perylene dyes“. In: *Nature Chemistry* 1.3 (2009), pp. 243–249 (cit. on p. 58).

[113] C. Roquelet, D. Garrot, J.-S. Lauret, et al. „Quantum efficiency of energy transfer in noncovalent carbon nanotube/porphyrin compounds“. In: *Applied Physics Letters* 97.14 (2010), p. 141918 (cit. on p. 58).

[114] F. Ernst. „Energy transfer in nanotube-chromophore complexes“. PhD thesis. Freie Universität Berlin, 2013 (cit. on p. 58).

[115] J. A. Broussard, B. Rappaz, D. J. Webb, and C. M. Brown. „Fluorescence resonance energy transfer microscopy as demonstrated by measuring the activation of the serine/threonine kinase Akt“. In: *Nature protocols* 8.2 (2013), p. 265 (cit. on p. 59).

[116] L. M. Loura, A. P. Carvalho, and J. P. Ramalho. „Direct calculation of Förster orientation factor of membrane probes by molecular simulation“. In: *Journal of Molecular Structure: THEOCHEM* 946.1-3 (2010), pp. 107–112 (cit. on p. 59).

[117] F. Ernst, T. Heek, A. Setaro, R. Haag, and S. Reich. „Excitation characteristics of different energy transfer in nanotube-perylene complexes“. In: *Applied Physics Letters* 102.23 (2013), p. 233105 (cit. on p. 60).

[118] K. Huth, M. Glaeske, K. Achazi, et al. „Fluorescent Polymer—Single-Walled Carbon Nanotube Complexes with Charged and Noncharged Dendronized Perylene Bisimides for Bioimaging Studies“. In: *Small* (2018), p. 1800796 (cit. on pp. 60, 61).

[119] R. Lehner, X. Wang, S. Marsch, and P. Hunziker. „Intelligent nanomaterials for medicine: carrier platforms and targeting strategies in the context of clinical application“. In: *Nanomedicine: Nanotechnology, Biology and Medicine* 9.6 (2013), pp. 742–757 (cit. on p. 63).

[120] P. P. Adiseshaiah, J. B. Hall, and S. E. McNeil. „Nanomaterial standards for efficacy and toxicity assessment“. In: *Wiley Interdisciplinary Reviews: Nanomedicine and Nanobiotechnology* 2.1 (2010), pp. 99–112 (cit. on p. 63).

[121] E. Heister, V. Neves, C. Tîlmaciu, et al. „Triple functionalisation of single-walled carbon nanotubes with doxorubicin, a monoclonal antibody, and a fluorescent marker for targeted cancer therapy“. In: *Carbon* 47.9 (2009), pp. 2152–2160 (cit. on p. 63).

[122] A. M. Smith, M. C. Mancini, and S. Nie. „Bioimaging: second window for in vivo imaging“. In: *Nature nanotechnology* 4.11 (2009), p. 710 (cit. on pp. 63, 77).

[123] H. Gong, R. Peng, and Z. Liu. „Carbon nanotubes for biomedical imaging: the recent advances“. In: *Advanced drug delivery reviews* 65.15 (2013), pp. 1951–1963 (cit. on p. 63).

[124] M. Cooper, A. Ebner, M. Briggs, et al. „Cy3B™: improving the performance of cyanine dyes“. In: *Journal of fluorescence* 14.2 (2004), pp. 145–150 (cit. on p. 63).

[125] Y. Li, Y. Bai, N. Zheng, et al. „Crosslinked dendronized polyols as a general approach to brighter and more stable fluorophores“. In: *Chemical Communications* 52.19 (2016), pp. 3781–3784 (cit. on p. 63).

[126] S. Zhu, J. Zhang, G. Vegesna, et al. „Highly water-soluble neutral BODIPY dyes with controllable fluorescence quantum yields“. In: *Organic letters* 13.3 (2010), pp. 438–441 (cit. on p. 63).

[127] K. Peneva, G. Mihov, F. Nolde, et al. „Water-Soluble Monofunctional Perylene and Terrylene Dyes: Powerful Labels for Single-Enzyme Tracking“. In: *Angewandte Chemie* 120.18 (2008), pp. 3420–3423 (cit. on p. 63).

[128] J. Qu, C. Kohl, M. Pottek, and K. Müllen. „Ionic Perylenetetracarboxdiimides: Highly Fluorescent and Water-Soluble Dyes for Biolabeling“. In: *Angewandte Chemie* 116.12 (2004), pp. 1554–1557 (cit. on p. 63).

[129] K. Peneva, G. Mihov, A. Herrmann, et al. „Exploiting the nitrilotriacetic acid moiety for biolabeling with ultrastable perylene dyes“. In: *Journal of the American Chemical Society* 130.16 (2008), pp. 5398–5399 (cit. on p. 63).

[130] S. K. Yang, X. Shi, S. Park, et al. „Monovalent, clickable, uncharged, water-soluble perylenediimide-cored dendrimers for target-specific fluorescent biolabeling“. In: *Journal of the American Chemical Society* 133.26 (2011), pp. 9964–9967 (cit. on p. 63).

[131] T. Heek, J. Nikolaus, R. Schwarzer, et al. „An amphiphilic perylene imido diester for selective cellular imaging“. In: *Bioconjugate chemistry* 24.2 (2013), pp. 153–158 (cit. on p. 64).

[132] C. Jung, B. K. Müller, D. C. Lamb, et al. „A new photostable terrylene diimide dye for applications in single molecule studies and membrane labeling“. In: *Journal of the American Chemical Society* 128.15 (2006), pp. 5283–5291 (cit. on p. 64).

[133] T Heek, C Kuhne, H Depner, et al. „Synthesis, Photophysical, and Biological Evaluation of Sulfated Polyglycerol Dendronized Perylenebisimides (PBIs) A Promising Platform for Anti-Inflammatory Theranostic Agents?“ In: *Bioconjugate chemistry* 27.3 (2016), pp. 727–736 (cit. on p. 64).

[134] C. Kohl, T. Weil, J. Qu, and K. Müllen. „Towards Highly Fluorescent and Water-Soluble Perylene Dyes“. In: *Chemistry-A European Journal* 10.21 (2004), pp. 5297–5310 (cit. on p. 64).

[135] P. Deria, C. D. Von Bargen, J.-H. Olivier, et al. „Single-handed helical wrapping of single-walled carbon nanotubes by chiral, ionic, semiconducting polymers“. In: *Journal of the American Chemical Society* 135.43 (2013), pp. 16220–16234 (cit. on p. 64).

[136] J. Budhathoki-Uprety, R. E. Langenbacher, P. V. Jena, D. Roxbury, and D. A. Heller. „A Carbon Nanotube Optical Sensor Reports Nuclear Entry via a Noncanonical Pathway“. In: *ACS nano* 11.4 (2017), pp. 3875–3882 (cit. on p. 64).

[137] R. Soleyman, S. Hirbod, and M. Adeli. „Advances in the biomedical application of polymer-functionalized carbon nanotubes“. In: *Biomaterials science* 3.5 (2015), pp. 695–711 (cit. on p. 64).

[138] M. Adeli, S. Beyranvand, and R. Kabiri. „Preparation of hybrid nanomaterials by supramolecular interactions between dendritic polymers and carbon nanotubes“. In: *Polymer Chemistry* 4.3 (2013), pp. 669–674 (cit. on p. 64).

[139] J. T. Robinson, G. Hong, Y. Liang, et al. „In vivo fluorescence imaging in the second near-infrared window with long circulating carbon nanotubes capable of ultrahigh tumor uptake“. In: *Journal of the American Chemical Society* 134.25 (2012), pp. 10664–10669 (cit. on p. 64).

[140] P. Petrov, G. Georgiev, D. Momekova, G. Momekov, and C. B. Tsvetanov. „UV-assisted grafting of polymers: a method towards biocompatible carbon nanotubes“. In: *Polymer* 51.12 (2010), pp. 2465–2471 (cit. on p. 64).

[141] R. M. Sankar, K. M. S. Meera, D. Samanta, et al. „The reinforced hydrogel for drug loading: immobilization of single-walled carbon nanotubes in cross-linked polymers via multiple interactions“. In: *RSC Advances* 2.32 (2012), pp. 12424–12430 (cit. on p. 64).

[142] I Armentano, M Dottori, E Fortunati, S Mattioli, and J. Kenny. „Biodegradable polymer matrix nanocomposites for tissue engineering: a review“. In: *Polymer degradation and stability* 95.11 (2010), pp. 2126–2146 (cit. on p. 64).

[143] J. J. Landry, P. T. Pyl, T. Rausch, et al. „The genomic and transcriptomic landscape of a HeLa cell line“. In: *G3: Genes, Genomes, Genetics* 3.8 (2013), pp. 1213–1224 (cit. on p. 65).

[144] Z. Tu, K. Achazi, A. Schulz, et al. „Combination of Surface Charge and Size Controls the Cellular Uptake of Functionalized Graphene Sheets“. In: *Advanced Functional Materials* 27.33 (2017) (cit. on p. 66).

[145] A. Faghani, I. S. Donskyi, M. Fardin Gholami, et al. „Controlled covalent functionalization of thermally reduced graphene oxide to generate defined bifunctional 2D nanomaterials“. In: *Angewandte Chemie International Edition* 56.10 (2017), pp. 2675–2679 (cit. on p. 69).

[146] V. Hong, S. I. Presolski, C. Ma, and M. Finn. „Analysis and Optimization of Copper-Catalyzed Azide–Alkyne Cycloaddition for Bioconjugation“. In: *Angewandte Chemie International Edition* 48.52 (2009), pp. 9879–9883 (cit. on p. 69).

[147] K. Petkau-Milroy and L. Brunsveld. „Self-Assembling Multivalency–Supramolecular Polymers Assembled from Monovalent Mannose-Labelled Discotic Molecules“. In: *European Journal of Organic Chemistry* 2013.17 (2013), pp. 3470–3476 (cit. on p. 69).

[148] C. Laurent, E. Flahaut, and A. Peigney. „The weight and density of carbon nanotubes versus the number of walls and diameter“. In: *Carbon* 48.10 (2010), pp. 2994–2996 (cit. on pp. 72, 107).

[149] K. Welsher, Z. Liu, D. Daranciang, and H. Dai. „Selective probing and imaging of cells with single walled carbon nanotubes as near-infrared fluorescent molecules“. In: *Nano letters* 8.2 (2008), pp. 586–590 (cit. on p. 77).

[150] K. Welsher, S. P. Sherlock, and H. Dai. „Deep-tissue anatomical imaging of mice using carbon nanotube fluorophores in the second near-infrared window“. In: *Proceedings of the National Academy of Sciences* 108.22 (2011), pp. 8943–8948 (cit. on p. 77).

[151] A. Hagen, M. Steiner, M. B. Raschke, et al. „Exponential decay lifetimes of excitons in individual single-walled carbon nanotubes“. In: *Physical review letters* 95.19 (2005), p. 197401 (cit. on p. 77).

[152] D. A. Tsyboulski, J.-D. R. Rocha, S. M. Bachilo, L. Cognet, and R. B. Weisman. „Structure-dependent fluorescence efficiencies of individual single-walled carbon nanotubes“. In: *Nano letters* 7.10 (2007), pp. 3080–3085 (cit. on p. 77).

[153] M. Jones, C. Engtrakul, W. K. Metzger, et al. „Analysis of photoluminescence from solubilized single-walled carbon nanotubes“. In: *Physical Review B* 71.11 (2005), p. 115426 (cit. on p. 77).

[154] E. Gaufrès, N. Izard, X. Le Roux, et al. „Optical microcavity with semiconducting single-wall carbon nanotubes“. In: *Optics express* 18.6 (2010), pp. 5740–5745 (cit. on p. 77).

[155] R. Watahiki, T. Shimada, P. Zhao, et al. „Enhancement of carbon nanotube photoluminescence by photonic crystal nanocavities“. In: *Applied Physics Letters* 101.14 (2012), p. 141124 (cit. on p. 77).

[156] A. Kumar, S. Kim, and J.-M. Nam. „Plasmonically engineered nanoprobes for biomedical applications“. In: *J. Am. Chem. Soc* 138.44 (2016), pp. 14509–14525 (cit. on p. 77).

[157] R. Bardhan, N. K. Grady, J. R. Cole, A. Joshi, and N. J. Halas. „Fluorescence enhancement by Au nanostructures: nanoshells and nanorods“. In: *Acs Nano* 3.3 (2009), pp. 744–752 (cit. on p. 77).

[158] J. R. Lakowicz. „Radiative decay engineering 5: metal-enhanced fluorescence and plasmon emission“. In: *Analytical biochemistry* 337.2 (2005), pp. 171–194 (cit. on p. 77).

[159] G. Hong, S. M. Tabakman, K. Welsher, et al. „Metal-enhanced fluorescence of carbon nanotubes“. In: *Journal of the American Chemical Society* 132.45 (2010), pp. 15920–15923 (cit. on pp. 77, 79, 81, 95).

[160] T. Ming, H. Chen, R. Jiang, Q. Li, and J. Wang. „Plasmon-controlled fluorescence: beyond the intensity enhancement“. In: *The Journal of Physical Chemistry Letters* 3.2 (2012), pp. 191–202 (cit. on p. 78).

[161] I. Freestone, N. Meeks, M. Sax, and C. Higgitt. „The Lycurgus cup—a roman nanotechnology“. In: *Gold bulletin* 40.4 (2007), pp. 270–277 (cit. on p. 79).

[162] *Notre-Dame de Paris*. 2018 (cit. on p. 79).

[163] N. R. Council. *Controlling the Quantum World: The Science of Atoms, Molecules, and Photons*. Washington, DC: The National Academies Press, 2007 (cit. on p. 79).

[164] S. Tokonami, Y. Yamamoto, H. Shiigi, and T. Nagaoka. „Synthesis and bioanalytical applications of specific-shaped metallic nanostructures: A review“. In: *Analytica chimica acta* 716 (2012), pp. 76–91 (cit. on p. 79).

[165] J. R. Lakowicz. *Principles of Fluorescence Spectroscopy*. 3rd ed. Springer, 2006 (cit. on pp. 79–81).

[166] T. Sakashita, Y. Miyauchi, K. Matsuda, and Y. Kanemitsu. „Plasmon-assisted photoluminescence enhancement of single-walled carbon nanotubes on metal surfaces“. In: *Applied Physics Letters* 97.6 (2010), p. 063110 (cit. on pp. 80, 81).

[167] G. Sun, J. B. Khurgin, and R. Soref. „Practical enhancement of photoluminescence by metal nanoparticles“. In: *Applied Physics Letters* 94.10 (2009), p. 101103 (cit. on p. 81).

[168] A. M. Kern, D. Zhang, M. Brecht, et al. „Enhanced single-molecule spectroscopy in highly confined optical fields: from $\lambda/2$-Fabry–Pérot resonators to plasmonic nano-antennas“. In: *Chemical Society Reviews* 43.4 (2014), pp. 1263–1286 (cit. on p. 81).

[169] B. Nikoobakht and M. A. El-Sayed. „Preparation and growth mechanism of gold nanorods (NRs) using seed-mediated growth method“. In: *Chem. Mater* 15.10 (2003), pp. 1957–1962 (cit. on p. 82).

[170] N. R. Jana, L. Gearheart, and C. J. Murphy. „Wet chemical synthesis of high aspect ratio cylindrical gold nanorods“. In: *The Journal of Physical Chemistry B* 105.19 (2001), pp. 4065–4067 (cit. on p. 82).

[171] J. Yang, Q. Zhao, M. Lyu, et al. „Chirality-Selective Photoluminescence Enhancement of ssDNA-Wrapped Single-Walled Carbon Nanotubes Modified with Gold Nanoparticles“. In: *small* 12.23 (2016), pp. 3164–3171 (cit. on p. 82).

[172] J. Lee, P. Hernandez, J. Lee, A. O. Govorov, and N. A. Kotov. „Exciton-plasmon interactions in molecular spring assemblies of nanowires and wavelength-based protein detection“. In: *Nature materials* 6.4 (2007), p. 291 (cit. on p. 86).

[173] P. Anger, P. Bharadwaj, and L. Novotny. „Enhancement and quenching of single-molecule fluorescence“. In: *Physical review letters* 96.11 (2006), p. 113002 (cit. on pp. 90, 92).

[174] M. Thomas, J.-J. Greffet, R Carminati, and J. Arias-Gonzalez. „Single-molecule spontaneous emission close to absorbing nanostructures“. In: *Applied physics letters* 85.17 (2004), pp. 3863–3865 (cit. on p. 90).

[175] P. Bharadwaj and L. Novotny. „Spectral dependence of single molecule fluorescence enhancement“. In: *Optics Express* 15.21 (2007), pp. 14266–14274 (cit. on p. 90).

[176] S. M. Bachilo, M. S. Strano, C. Kittrell, et al. „Structure-assigned optical spectra of single-walled carbon nanotubes“. In: *Science* 298.5602 (2002), pp. 2361–2366 (cit. on p. 91).

[177] G. Ostojic, S Zaric, J Kono, et al. „Interband recombination dynamics in resonantly excited single-walled carbon nanotubes“. In: *Physical Review Letters* 92.11 (2004), p. 117402 (cit. on p. 92).

[178] O. A. Dyatlova, C. Koehler, P. Vogel, et al. „Relaxation dynamics of carbon nanotubes of enriched chiralities“. In: *Physical Review B* 90.15 (2014), p. 155402 (cit. on pp. 92–94).

[179] A. Bruno, F. Ossler, C. de Lisio, et al. „Detection of fluorescent nanoparticles in flame with femtosecond laser-induced fluorescence anisotropy“. In: *Optics express* 16.8 (2008), pp. 5623–5632 (cit. on p. 92).

[180] O. A. Dyatlova, C. Khler, E. Malic, et al. „Ultrafast relaxation dynamics via acoustic phonons in carbon nanotubes“. In: *Nano letters* 12.5 (2012), pp. 2249–2253 (cit. on p. 93).

[181] B. L. Darby, B. Auguié, M. Meyer, A. E. Pantoja, and E. C. Le Ru. „Modified optical absorption of molecules on metallic nanoparticles at sub-monolayer coverage“. In: *Nature Photonics* 10.1 (2016), p. 40 (cit. on p. 93).

[182] T. Gokus, A. Hartschuh, H. Harutyunyan, et al. „Exciton decay dynamics in individual carbon nanotubes at room temperature“. In: *Applied Physics Letters* 92.15 (2008), p. 153116 (cit. on p. 94).

[183] Y. Fu, J. Zhang, and J. R. Lakowicz. „Plasmon-enhanced fluorescence from single fluorophores end-linked to gold nanorods“. In: *Journal of the American Chemical Society* 132.16 (2010), pp. 5540–5541 (cit. on p. 94).

[184] T. Hertel and G. Moos. „Electron-phonon interaction in single-wall carbon nanotubes: A time-domain study“. In: *Physical review letters* 84.21 (2000), p. 5002 (cit. on p. 94).

[185] M Zamkov, N Woody, B Shan, Z Chang, and P Richard. „Lifetime of charge carriers in multiwalled nanotubes“. In: *Physical review letters* 94.5 (2005), p. 056803 (cit. on p. 94).

[186] D. A. Siegel, C.-H. Park, C. Hwang, et al. „Many-body interactions in quasi-freestanding graphene“. In: *Proceedings of the National Academy of Sciences* 108.28 (2011), pp. 11365–11369 (cit. on p. 94).

[187] S Piscanec, M Lazzeri, F. Mauri, A. Ferrari, and J Robertson. „Kohn anomalies and electron-phonon interactions in graphite“. In: *Physical review letters* 93.18 (2004), p. 185503 (cit. on p. 94).

[188] R. Narula and S. Reich. „Graphene band structure and its 2 D Raman mode“. In: *Physical Review B* 90.8 (2014), p. 085407 (cit. on p. 94).

[189] P. Tassin, T. Koschny, M. Kafesaki, and C. M. Soukoulis. „A comparison of graphene, superconductors and metals as conductors for metamaterials and plasmonics“. In: *Nature Photonics* 6.4 (2012), pp. 259–264 (cit. on p. 95).

[190] C. D. Bain and G. M. Whitesides. „Molecular-level control over surface order in self-assembled monolayer films of thiols on gold“. In: *Science* 240.4848 (1988), pp. 62–64 (cit. on p. 95).

[191] L. Gabrielli, G. Altoè, M. Glaeske, et al. „Controlling the Decoration of the Reduced Graphene Oxide Surface with Pyrene-Functionalized Gold Nanoparticles“. In: *physica status solidi (b)* 254.11 (2017), p. 1700281 (cit. on pp. 99, 105).

Selbstständigkeitserklärung

Hiermit versichere ich, dass ich alle verwendeten Hilfsmittel und Hilfen angegeben und die vorliegende Arbeit auf dieser Grundlage selbstständig verfasst habe. Diese Arbeit ist nicht schon einmal in einem früheren Promotionsverfahren eingereicht worden.

Mareen Gläske